

Spatiotemporal Controlled Delivery of Nanoparticles to Injured Vasculature

By

Juliana Maria Chan

B.A. (Hons), M.A. Natural Sciences Tripos, 2005
University of Cambridge, England

Submitted to the Department of Biology in Partial
Fulfillment of the Requirements for the Degree of

Doctor of Philosophy in Biology

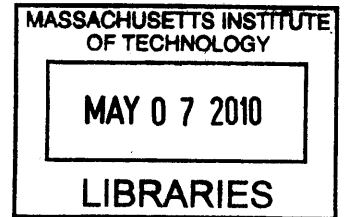
At the

Massachusetts Institute of Technology

June 2010

© 2010 Massachusetts Institute of Technology.
All rights reserved.

ARCHIVES



Signature of Author:

A handwritten signature in black ink, appearing to read "Juliana Chan".

Juliana Chan
Department of Biology
April 30, 2010

Certified by:

Robert S. Langer, Sc.D.
Institute Professor
Thesis Supervisor

Accepted by:

A handwritten signature in black ink, appearing to read "Steven P. Bell".

Steven P. Bell, Ph.D.
Professor of Biology
Chairman, Graduate Committee

This doctoral thesis was successfully defended in public on Thursday, March 4th 2010 at 1:00PM in the McGovern Auditorium, Whitehead Institute in partial fulfillment of the degree of Doctor of Philosophy in Biology at the Massachusetts Institute of Technology.

This thesis has been examined by the following Thesis Committee:

Thesis Advisor

Robert S. Langer, Sc.D.

Institute Professor

Massachusetts Institute of Technology

Omid C. Farokhzad, M.D.

Associate Professor of Anesthesiology

Harvard Medical School

Thesis Committee

Phillip Sharp, Ph.D.

Institute Professor

Massachusetts Institute of Technology

Michael Hemann, Ph.D.

Latham Family Career Development Assistant Professor of Biology

Massachusetts Institute of Technology

David Housman, Ph.D.

Ludwig Professor of Biology

Massachusetts Institute of Technology

External Thesis Committee

Rakesh K. Jain, Ph.D.

Andrew Werk Cook Professor of Radiation Oncology

Harvard Medical School

Spatiotemporal Controlled Delivery of Nanoparticles to Injured Vasculature

By

Juliana Maria Chan

Submitted to the Department of Biology on April 30, 2010
in Partial Fulfillment of the Requirements for the
Degree of Doctor of Philosophy in Biology

ABSTRACT

Complex multimodal nanoparticles (NP) that target and deliver therapeutic agents to a site of disease are a promising direction in modern medicine. As a starting point for innovation, we designed a hybrid NP system combining the benefits of liposomes and polymeric NPs. These particles have a polymeric surface which displays targeting ligands while avoiding macrophage uptake. A liposome-like layer provides *in vivo* biocompatibility and a hydrophobic core allows for high-capacity small molecule drug delivery.

Targeting ligands that bind injured vasculature were discovered and optimized by screening an M13 bacteriophage library (10^9 independent clones) against collagen IV, the major component of the basement membrane. Relative binding affinities using ELISA identified the lead targeting candidate, which bound with 900-fold greater relative affinity to collagen IV when compared with the unselected library.

The selected peptide sequence was synthesized and tested for its ability to actively target the hybrid NP system. Paclitaxel, an anti-proliferative drug, was chosen as the delivered pharmaceutical. Drug release was modified through a slow-eluting paclitaxel conjugate using controlled ester hydrolysis (drug release ~10-12 days *in vitro*). To test these targeted NPs, injured vasculature was approximated using an aortic smooth muscle culture embedded on a collagen IV matrix. In this setting, the hybrid NPs showed clear evidence of increased potency using the selected ligands.

In experimental animal models of surgery-induced vascular injury, targeted NPs showed a four-fold improved retention at angioplastied aortas over intact aortas *ex vivo*. Targeted NPs were tested as intraarterially delivered therapy to angioplastied carotid arteries *in vivo* and showed a two-fold better localization at injury sites versus scrambled-peptide and non-targeted NPs. Targeted NPs were also tested using a systemic, intravenous infusion administered post-procedure on Day 1 and 6 and resulted in lower neointima-to-media (N/M) scores at two weeks compared to FDA-approved Taxol® and injury-only groups ($N/M_{\text{sham}}=1.249 \pm 0.046$, vs. $N/M_{\text{Taxol}}=0.837 \pm 0.087$, $N/M_{\text{NP}}=0.749 \pm 0.136$ and $N/M_{\text{Pep-NP}}=0.662 \pm 0.169$, all $P < 0.01$ vs. injury-only, mean \pm SEM, $n=5$). These findings indicate that complex, multilayered NPs can functionally target and treat injured vasculature, a clinical problem of primary importance.

Thesis Supervisor: Robert S. Langer, Sc.D.

Title: David H. Koch Institute Professor

ACKNOWLEDGEMENTS

I am extremely grateful to Professor Robert Langer for his constant support and invaluable input into my research, scientific writing and career development. I will always be indebted to you for your mentorship.

I am also extremely grateful to Professor Omid Farokhzad for co-supervising my thesis project. I thank you for your confidence in me as I pursued my research, and I cherish this opportunity given to me.

I am indebted to members of my thesis committee, Professor Phillip Sharp, Professor Michael Hemann and Professor David Housman, as well as my external thesis examiner, Professor Rakesh Jain, for supporting this thesis project.

I would like to thank my colleagues in the Langer Lab. Although I cannot mention all of you, I thank you profusely for your time and help. I am fortunate to have worked closely with Prof. Liangfang Zhang, June-Wha Rhee, Thuy Tram Dang, Dr. Weiwei Gao, Eric Pridgen, Dr. Nagesh Kolishetti, Dr. Zeyu Xiao, Grace Liao, Dr. David Nguyen, Dr. Chester Drum, Rong Tong, Prof. Jianjun Cheng and Prof. Gershon Golomb. Thank you for being my collaborators and for supporting me every step of the way.

I dedicate this work to my parents, Eric and Betty, my sister Samantha, and my aunt Penny. They have steadfastly supported me as I pursued my studies abroad for the past eight years.

Finally, I would like to thank the MIT Department of Biology for accepting me to this Ph.D. program, the NIH and David H. Koch Prostate Cancer Foundation for project funding, and the Agency for Science, Technology and Research (A*STAR), Singapore for awarding me the B.S.-Ph.D. National Science Fellowship.

Thank you.

TABLE OF CONTENTS

ABSTRACT.....	3
ACKNOWLEDGEMENTS.....	4
TABLE OF CONTENTS.....	5
ABBREVIATIONS	12
INTRODUCTION	15
Chapter 1. Background.	17
Nanoparticles in Medicine – Therapeutic Applications and Developments	17
Table 1: FDA-approved NP-based therapeutics for clinical use.	18
Polymeric Nanoparticles for Drug Delivery	19
Figure 1. Schematic of therapeutic NP platforms in clinical and preclinical development.	19
Barriers to Efficient Nanoparticle Delivery	20
Next Generation Nanoparticles: Targeted Nanoparticle Delivery	23
Figure 2. A theoretical model of NP targeting.....	23
Modeling approach to the interaction of particles in specific contact with receptor substrates under linear laminar flow.	23
Table 2: Various classes of targeting ligands for NP surface-functionalization.....	25
Moving Beyond the Targeting Paradigm	27
Figure 3. Targeting paradigm.	27
Figure 4. New targeting paradigm.	28
Outlook.....	29
References	30
Chapter 2. Design and Engineering of Hybrid Lipid-Polymeric Core-Shell Nanoparticles.....	35
Abstract	35
Introduction	36
Methods.....	38
Materials.	38
Synthesis of PLGA–lipid–PEG NPs.....	38
NP Size and Surface Charge Characterization.	39
Transmission Electron Microscopy (TEM) Characterization.	39
Drug Loading and Release Kinetics.	39

NP In Vitro Stability.....	40
NP Cytotoxicity Assays.....	40
PLGA–Lipid–PEG Microparticle Synthesis and Self-Assembly.....	41
Scanning Electron Microscopy (SEM) Characterization.....	41
Results	42
Self-assembly of PLGA–lipid–PEG NPs.....	42
Characterization of PLGA–lipid–PEG NP Properties.....	42
PLGA–lipid–PEG NP Lipid Formulation Parameters.....	43
PLGA–lipid–PEG NP Polymer Formulation Parameters.....	44
In Vitro Controlled Drug Release Kinetics of PLGA–lipid–PEG NPs.....	45
In Vitro Stability of PLGA–lipid–PEG NPs.....	47
Post-formulation Purification and Storage of PLGA–lipid–PEG NPs.....	48
Scalability of PLGA–lipid–PEG NPs.....	49
In Vitro Cytotoxicity of PLGA–lipid–PEG NPs.....	49
PLGA–Lipid–PEG Microparticle Synthesis by the Homogenization Emulsion Technique.....	50
Figure 1. Synthesis of PLGA–lipid–PEG core–shell NPs.....	51
Figure 2. Lipid/lipid–PEG to polymer ratios.....	51
Figure 3. Requirements for an optimal PLGA–lipid–PEG system.....	52
Figure 4. The effect of formulation parameters on the size and zeta potential of PLGA–lipid–PEG NPs.....	53
Figure 5. Controlled and sustained drug release profiles of PLGA–lipid–PEG NPs.....	54
Figure 6. Drug loading capacity and release profile of PLGA–lipid–PEG hybrid NPs versus PLGA–PEG and PLGA polymeric NPs.....	55
Figure 7. NP temporal stability in vitro.....	56
Figure 8. Post-formulation stability of PLGA–lipid–PEG NPs.....	57
Figure 9. Cytotoxicity of PLGA–lipid–PEG NPs on HeLa and HepG2 cell lines.....	57
Figure 10. SEM images of PLGA–lipid–PEG MPs.....	58
Figure 11. Representative diameters of PLGA–lipid–PEG MPs.....	59
Discussion.....	59
References.....	62
Chapter 3. Pharmacokinetic-Pharmacodynamic Studies of Hybrid Lipid-Polymeric Nanoparticles.	64
Abstract.....	64
Introduction.....	65
Methods.....	66

Materials.....	66
Animals.....	67
In vivo Circulation Half-Life Studies.....	67
Lipid-PEG-Aptamer Triblock Synthesis.....	67
Cellular Uptake Studies by Fluorescence Microscopy.....	68
LnCaP Xenograft Mouse Model.....	68
In vivo Biodistribution Studies.....	69
Results.....	70
In Vivo Circulation Half-Life of PLGA–lipid–PEG NPs.....	70
Aptamer Targeted–NP Synthesis.....	70
Cellular Uptake Studies.....	71
In Vivo Biodistribution of PLGA–lipid–PEG NPs.....	72
Figure 1. Circulation half-life of PLGA–lipid–PEG and PLGA– <i>b</i> –PEG NPs.....	73
Figure 2. Hybrid NPs with varying aptamer surface densities.....	74
Figure 3. Calibration of A10 aptamer surface coverage on hybrid NPs.....	75
Figure 4. Cellular uptake of hybrid NPs surface-modified with the A10 RNA aptamer..	76
Figure 5. Average ³ H readings taken as a percentage of injected dose per organ.....	77
Figure 6. Average ³ H readings in tumors taken as a percentage of injected dose per gram of tumor tissue.....	77
Discussion.....	78
References.....	81
Chapter 4. Fibrin Targeted Nanoparticles for Delivery to Diverse Atherosclerotic Lesion Types in Coronary Artery Disease.....	82
Abstract.....	82
Introduction.....	83
Methods.....	84
Materials.....	84
Animals.....	84
Synthesis of Lipid–PEG–Peptide Copolymers.....	85
Synthesis of Fluorescent Dye-PLGA Copolymers.....	85
Preparation of Peptide-NP Conjugates.....	85
Induction of Early Stage Atherogenesis in ApoE ^{-/-} Mice.....	86
Ex Vivo ApoE ^{-/-} Mouse Aorta Targeting Studies.....	86
Ex Vivo Balloon-Injured Rat Aorta Targeting Studies.....	86
Results.....	87

Synthesis of Fibrin-Targeted Hybrid NPs.	87
Characterization of Physicochemical Properties of Targeted-NPs.....	87
Targeting of Thin-Cap Fibroatheroma in ApoE ^{-/-} Mice Fed an Atherogenic Diet.	87
Targeting of Revascularized Stenotic Lesions in Balloon-Injury Rat Models.	88
Figure 1. Fibrin-targeting for a diversity of lesions in human coronary atherosclerosis. .	90
Figure 2. NP synthesis for fibrin-targeted drug delivery.	91
Figure 3. Targeting of thin-cap fibroatheroma in ApoE ^{-/-} mouse aortas.	92
Figure 4. Uninjured and balloon-angioplastied aortas.	93
Figure 5. Targeting of revascularized lesions in balloon-injured rat aortas.	93
Discussion	94
References	96
Chapter 5. Screening of a Phage Display Library for the Discovery of Novel Targeting Peptides.	98
Abstract	98
Introduction	99
Methods.....	101
Materials.	101
Screening of Library.....	101
Phage Amplification and Precipitation.....	102
Titering and Measurement of Phage Plaque Forming Units.	102
DNA Sequencing and Peptide Sequence Analysis.....	103
Phage ELISA Matrigel Binding Studies.....	103
IC ₅₀ Value Determination of Phage Clones.....	103
Titer Count Analyses.	104
Statistical Analysis.	104
Results	104
Selection and Characterization of Basement Membrane Targeting Peptides for Vascular Wall Targeting.....	104
Matrigel ELISA Binding Assays of Phage Clones.....	105
Sequence Specific Competition Assays of Phage Clones.	106
Titer Count Analyses of Phage Clones.....	107
Epitope Mapping by Phage Display.	107
Selection and Characterization of Basement Membrane Targeting Peptides against Matrigel.	108
Figure 1. Panning with a pentavalent peptide library displayed on pIII.	109

Figure 2. Sequence of the peptide cloning site where the library is inserted into the M13KE phage genome.	110
Figure 3. Illustration of targeting to the basement membrane.	111
Figure 4. Schematic of phage display selection strategy.	111
Figure 5. Identification and characterization of peptides for targeting to the basement membrane.	112
Figure 6. Alignment and consensus sequence.	113
Figure 7. Sequence-specific competition binding assays.	113
Figure 8. Titer count analyses of C-11 compared to the R0 phage library on Matrigel and collagen IV.	114
Figure 9. Epitope mapping using phage display.	115
Figure 10. Phage display strategy against Matrigel matrices.	116
Discussion	117
References	120
Chapter 6. Spatiotemporal Targeting of Nanoparticles to Injured Vasculature.	123
Abstract	123
Introduction	124
Methods	126
Materials.	126
Paclitaxel-Poly lactide Conjugation.	126
Synthesis and Characterization of Nanoburrs.	126
Release Kinetics Studies.	127
HaSMC Cytotoxicity Studies.	127
Animals.	128
Balloon-Angioplasty Ex Vivo Studies.	128
Balloon-Angioplasty In Vivo Studies.	128
Optical Imaging and Fluorescence Microscopy Studies.	129
Statistical Analysis.	129
Results	130
Synthesis and Characterization of the Nanoburr Drug Delivery System.	130
Targeted Drug Release from Nanoburrs.	131
Binding Studies in Angioplasty Models of Injured Vasculature.	131
Ex Vivo Binding Studies in Angioplastied Aortas.	132
In Vivo Intraarterial Delivery Studies in Angioplastied Carotid Arteries.	133
In Vivo Intravenous Delivery Studies in Angioplastied Carotid Arteries.	133

Figure 1. Schematic of Ptx1–PLA biomaterial synthesis.	134
Figure 2. Schematic of nanoburr synthesis by nanoprecipitation and self-assembly.	134
Figure 3. Nanoburr characterization.	135
Figure 4. Targeted drug release from nanoburrs.....	136
Figure 5. Representative H&E stained cross-sections of balloon-injured and uninjured aortas.	136
Figure 6. Ex vivo delivery in an abdominal aorta injury model.	137
Figure 7. Quantification of nanoburr binding ex vivo to angioplastied aortas.	137
Figure 8. Representative images of nanoburr binding to angioplastied and normal aortas ex vivo.....	138
Figure 9. In vivo IA delivery in a carotid injury model.....	138
Figure 10. Quantification of nanoburr binding in vivo to angioplastied left common carotids by IA delivery.....	139
Figure 11. Representative images of nanoburr binding in vivo by IA delivery to angioplastied left common carotids.	139
Figure 12. In vivo systemic delivery in a carotid angioplasty model.	140
Figure 13. Quantification of nanoburr binding in vivo to angioplastied left common carotids by i.v. delivery.....	140
Figure 14. Representative images of nanoburr binding in vivo by i.v. delivery to angioplastied left common carotids.	141
Discussion	141
References	144
Chapter 7. Targeted Nanoparticles for Anti-Restenotic Drug Delivery to Injured Vasculature.	146
Abstract	146
Introduction	147
Methods.....	149
Materials.	149
Synthesis and Characterization of Targeted NPs.	149
Preparation of Taxol Formulations.....	150
Animals.....	150
Rat Carotid Model and In Vivo Proliferation Studies.	150
Morphometric Analysis.	151
Immunohistochemistry.	151
Statistics.....	152
Results	153

Rat Carotid Injury Model.	153
Characterization of NP Treatment Groups.	154
Morphometric Analyses of Treatment Groups.	154
Figure 1. Schematic of events after angioplasty and stenting.	156
Figure 2. A rat carotid model of vascular injury.	157
Figure 3. Representative carotid arteries with and without injury.	158
Figure 4. Determination of N/M ratios of carotid samples.	159
Figure 5. N/M ratio measurements of intimal proliferation.	160
Figure 6. Representative H&E carotid cross-sections from different treatment groups.	161
Figure 7. Representative α -SMA immunostained carotid cross-sections from different treatment groups.	161
Discussion	162
References	165
Chapter 8. Closing Remarks.	167
References	169
CURRICULUM VITAE.	170

ABBREVIATIONS

^1H NMR	proton nuclear magnetic resonance
^3H	tritium
A647	Alexa Fluor 647 dye
ABTS	2,2'-azino-bis(3-ethylbenzthiazoline-6-sulphonic acid)
ANOVA	analysis of variance
ATVD	atherothrombotic vascular disease
Apt	aptamer
BMS	bare metal stent
BSA	bovine serum albumin
CABG	coronary artery bypass graft surgery
CAD	coronary artery disease
CREKA	cysteine-arginine-glutamic acid-lysine-alanine
CrEL	Cremophor polyethoxylated castor oil
CRP	C-reactive protein
DCM	dichloromethane
DES	drug eluting stent
DI H ₂ O	distilled water
DLS	dynamic light scattering
DLT	dose-limiting toxicity
DMSO	dimethyl sulfoxide
DNA	deoxynucleic acid
DSPE	1,2-distearoyl-sn-glycero-3-phosphoethanolamine
Dtxl	docetaxel
EC	endothelial cell
ECM	extracellular matrix
EDC	1-ethyl-3-(3-dimethylaminopropyl)carbodiimide hydrochloride
EHS	Engelbreth-Holm-Swarm
ELISA	enzyme-linked immunosorbant assay
EPR	enhanced permeability and retention effect
F _{ab}	antigen-binding fragment
FBS	fetal bovine serum
FDA	United States Food and Drug Administration
FTIR	Fourier transform infra-red spectroscopy
F _v	variant fragment
GRAS	generally regarded as safe
H&E	hematoxylin & eosin
HaSMC	human aortic smooth muscle cell
HeLa	human cervical carcinoma cell line
HepG2	human hepatocellular carcinoma cell line
HRP	horse-radish peroxidase
IA	intraarterial
IC ₅₀	half maximal inhibitory concentration
IPTG	isopropyl β -D-1-thiogalactopyranoside

IV	intravenous
IVIS	image visualization and infrared spectroscopy
K_D	dissociation constant
LB	lysogeny broth (informally: Luria-Bertani broth)
LDEV	lactate dehydrogenase elevating virus
LNCaP	human prostate carcinoma cell line
MACE	major adverse cardiac event
MDR	multiple-drug resistance
MP	microparticle
MTS	3-(4,5-dimethylthiazol-2-yl)-5-(3-carboxymethoxyphenyl)-2-(4-sulfophenyl)-2H-tetrazolium, inner salt
MWCO	molecular weight cut-off
NBD-cholesterol	22-(<i>N</i> -(7-nitrobenz-2-oxa-1,3-diazol-4-yl)amino)-23,24-bisnor-5-cholen-3 β -ol
NCBI	National Center for Biotechnology Information
NHS	N-hydroxysuccinimide
N/M ratio	neointima/media ratio
NP	nanoparticle
P_a	probability of adhesion
PAMP	pathogen-associated molecular pattern
pBLAST	protein basic local alignment search tool
PC3	human prostate carcinoma cell line
PCI	percutaneous coronary intervention
PCL	poly(ϵ -caprolactone)
PCTA	percutaneous transluminal angioplasty
PD	pharmacodynamic
PDB	protein data bank
PEG	poly(ethylene glycol)
PFU	plaque-forming unit
PLA	poly(D,L -lactic acid)
PLGA	poly(D,L -lactic- <i>co</i> -glycolic acid)
PK	pharmacokinetic
PMS	phenazine methosulfate
PSMA	prostate-specific membrane antigen
Ptxl	paclitaxel
PVA	poly(vinyl alcohol)
R0	unselected 'round zero' phage library
RES	reticulo-endothelial system
RFU	relative fluorescence unit
RGD	arginine-glycine-aspartate tripeptide
RNA	ribonucleic acid
ROI	region of interest
RP-HPLC	reverse-phase high performance liquid chromatography
RT	room temperature
SAP	serum amyloid P component
scF _v	single-chain variant fragment
SD	standard deviation of the mean

SELEX	systematic evolution of ligands by exponential enrichment
SEM	standard error of the mean
SEM	scanning electron microscopy
sPC	soy phosphatidylcholine
Sulfo-NHS	sulfo-N-hydroxysuccinimide
TBST	tris-buffered saline with Tween-20
T/C	treatment over control
TC₅₀	half maximal toxic concentration
TC₁₀₀	maximal toxic concentration
TCEP	tris(2-carboxyethyl)phosphine
TEM	transmission electron microscopy
THF	tetrahydrofuran
VEGF	vascular endothelial growth factor
VLST	very late stent thrombosis
VvG	Verhoeff van Gieson

INTRODUCTION

The field of nanotechnology has crossed significant milestones from the systemic delivery of medicines, and over the last two decades there has been a convergence in knowledge on the biological and physicochemical properties of nanomaterials. In 2010, several liposomal drugs and polymer-drug conjugates have already been approved by the U.S. Food and Drug Administration (FDA) for use in many indications, but polymeric nanoparticle (NP) technology is only now nearing clinical approval.

The commentary in **Chapter 1** discusses the foundations of polymeric NP delivery using biocompatible, biodegradable, FDA-approved controlled-release polymers. Systemically-delivered polymeric NPs have generated immense academic and clinical interest as they are designed to avoid immune responses and improve on drug release profiles. First generation NPs, however, are limited by the lack of targeting to solid tumors and other sites of interest. Since then, second generation NPs have used targeting ligands to alter the biodistribution and improve on the efficacy of NP-delivered therapeutic agents.

Chapter 2 describes the design of hybrid lipid-polymeric NPs that combine features of liposomes and polymeric NPs. This hybrid version has a polymeric core and a liposomal shell to derive improved drug loading, controlled drug release, biocompatibility and efficacy. Chapter 2 also describes the development of microparticle equivalents for applications that require larger biocompatible particles with polymeric cores.

An in depth study on the *in vivo* pharmacokinetic and pharmacodistribution profile of lipid-polymeric NPs is outlined in **Chapter 3**. The addition of RNA aptameric ligands specific for the prostate specific membrane antigen (PSMA) on prostate epithelial cells was found to alter the localization of radiolabeled NPs in mouse xenograft models of prostate cancer.

Subsequently, an interest in peptide targeting ligands led to the development of peptide-functionalized NPs against fibrin in **Chapter 4**. The peptide-targeted NPs were delivered to atherosclerotic plaques in Apolipoprotein E-deficient mice and to angioplastied aortas in balloon-injured rats. The NPs targeted thrombotic elements found in non-stenotic and stenotic lesions and may potentially be applied towards the management of coronary artery disease.

The focus of **Chapter 5** is the discovery of novel peptide ligands for targeting to injured vasculature. Peptide ligands were characterized from a M13 bacteriophage display screen against collagen IV and Matrigel basement membrane extracts. By comparing the candidates against an unbiased library, a lead candidate peptide was selected for further characterization. Additionally, a number of promising candidates were identified in sequence alignment studies for their biological relevance to resident basement membrane structures.

Building on the foundations of peptide-targeting in Chapter 4 and given the favorable results of the screen in Chapter 5, a spatiotemporal NP delivery system was developed to target exposed basement membrane. In **Chapter 6**, targeted NPs were delivered to injured vasculature *ex vivo* and *in vivo*. Taken together, results from these studies led to the conclusion that targeted NPs preferentially localized to sites of injury over intact arterial vessels.

Chapter 7 puts the collective previous results and techniques into a medical context with the targeting and treatment of injured vasculature. The lead targeted NP system was delivered infusionally as an anti-proliferative therapy for arterial stenosis and compared against FDA-approved Taxol® (Cremophor-EL micelles of paclitaxel), non-targeted NPs and injury-only sham controls. The targeted NP group reduced neointimal hyperplasia and luminal occlusion more effectively versus Taxol and non-targeted NP groups.

As a step forward, the commentary in **Chapter 8** describes the role of nanotechnology in cardiovascular medicine and describes the potential of this NP technology as an infusional treatment for restenosis.

Chapter 1. Background.

Nanoparticles in Medicine – Therapeutic Applications and Developments

Nanotechnology is the understanding and control of matter generally in the 1-100 nm dimension range. The application of nanotechnology to medicine, referred to as nanomedicine, concerns the use of precisely engineered materials at this length scale to develop novel therapeutic and diagnostic modalities^{1,2}. Nanomaterials have unique physicochemical properties which are different from bulk material of the same composition, such as ultra small size, large surface area to mass ratio and high reactivity. The use of materials in nanoscale may overcome certain limitations found in traditional therapeutic and diagnostic agents, as it provides unparalleled freedom to modify fundamental properties of solubility, diffusivity, blood circulation half-life, drug release profile and immunogenicity. These nanoscale agents may be more effectively and/or conveniently administered, reduce off-target toxicity and extend product life cycle, all of which may ultimately reduce health-care costs.

The topic of this dissertation lies principally on the therapeutic applications of systemically administered nanoparticle (NPs). Until now, the main utility of parenterally delivered first generation NPs has been to improve on the solubility of hydrophobic drugs and prolong drug circulation half-life *in vivo*. This thesis details the development of second generation NPs with controlled release and targeting functions. Other novel functions of these second generation nanocarriers include releasing drugs in an environmentally responsive manner to lower the frequency of administration^{3,4}, and to synergistically deliver two or more drugs for combination therapy and suppression of drug resistance⁵.

Nanomedical research has shown immense clinical relevance, with great strides being made towards therapeutic approval of NP drug formulations. In the past two decades, there has been a steady increase in the number of commercially available NP-based therapeutic products, with numerous ensuing products currently under clinical testing or entering the commercial pipeline. More than 24 nanotechnology-based therapeutic products have been approved for clinical use, with total sales exceeding \$5.4 billion by 2006⁶. Among these products, liposomal⁷

and polymer–drug conjugates^{8,9} represent the two dominant classes that account for more than 80% of the market (Table 1).

Table 1 Clinically approved nanoparticle-based therapeutics

Composition	Trade name	Company	Indication	Administration
<i>Liposomal platforms</i>				
Liposomal amphotericin B	Abelcet	Enzon	Fungal infections	i.v.
Liposomal amphotericin B	AmBisome	Gilead Sciences	Fungal and protozoal infections	i.v.
Liposomal cytarabine	DepoCyt	SkyePharma	Malignant lymphomatous meningitis	i.t.
Liposomal daunorubicin	DaunoXome	Gilead Sciences	HIV-related Kaposi's sarcoma	i.v.
Liposomal doxorubicin	Myocet	Zeneus	Combination therapy with cyclophosphamide in metastatic breast cancer	i.v.
Liposomal IRIV vaccine	Epaxal	Berna Biotech	Hepatitis A	i.m.
Liposomal IRIV vaccine	Inflexal V	Berna Biotech	Influenza	i.m.
Liposomal morphine	DepoDur	SkyePharma, Endo	Postsurgical analgesia	Epidural
Liposomal verteporfin	Visudyne	QLT, Novartis	Age-related macular degeneration, pathologic myopia, ocular histoplasmosis	i.v.
Liposome-PEG doxorubicin	Doxil/Caelyx	Ortho Biotech, Schering-Plough	HIV-related Kaposi's sarcoma, metastatic breast cancer, metastatic ovarian cancer	i.m.
Micellular estradiol	Estrasorb	Novavax	Menopausal therapy	Topical
<i>Polymeric platforms</i>				
L-Glutamic acid, L-alanine, L-lysine, and L-tyrosine copolymer	Copaxone	TEVA Pharmaceuticals	Multiple sclerosis	s.c.
Methoxy-PEG-poly(D,L-lactide) taxol	Genexol-PM	Samyang	Metastatic breast cancer	i.v.
PEG-adenosine deaminase	Adagen	Enzon	Severe combined immunodeficiency disease associated with ADA deficiency	i.m.
PEG-anti-VEGF aptamer	Macugen	OSI Pharmaceuticals	Age-related macular degeneration	i.r.
PEG- α -interferon 2a	Pegasys	Nektar, Hoffmann-La Roche	Hepatitis B, hepatitis C	s.c.
PEG-GCSF	Neulasta	Amgen	Neutropenia associated with cancer chemotherapy	s.c.
PEG-HGF	Somavert	Nektar, Pfizer	Acromegaly	s.c.
PEG-L-asparaginase	Oncaspar	Enzon	Acute lymphoblastic leukemia	i.v., i.m.
Poly(allylamine hydrochloride)	Renagel	Genzyme	End-stage renal disease	Oral
<i>Other platforms</i>				
Albumin-bound paclitaxel	Abraxane	Abraxis BioScience, AstraZeneca	Metastatic breast cancer	i.v.
Nanocrystalline aprepitant	Emend	Elan, Merck	Antiemetic	Oral
Nanocrystalline fenofibrate	Tricor	Elan, Abbott	Anti-hyperlipidemic	Oral
Nanocrystalline sirolimus	Rapamune	Elan, Wyeth Pharmaceuticals	Immunosuppressant	Oral

ADA, adenosine deaminase; GCSF, granulocyte colony-stimulating factor; HGF, hepatocyte growth factor; HIV, human immunodeficiency virus; i.m., intramuscular; i.r., intravitreal; IRIV, immunopotentiating reconstituted influenza virosome; i.t., intrathecal; i.v., intravenous; PEG, polyethyleneglycol; s.c., subcutaneous; VEGF, vascular endothelial growth factor.

Table 1: FDA-approved NP-based therapeutics for clinical use. This figure was originally published in *Clinical Pharmacology and Therapeutics*. Zhang, L., Gu, F.X., Chan, J.M. *et al.* Nanoparticles in Medicine: Therapeutic Applications and Developments. *Clin Pharmacol Ther* 2008; 83: 761-9. © Nature Publishing Group.

Polymeric Nanoparticles for Drug Delivery

Besides liposomes and polymeric conjugates, the most common NP platforms today include polymeric NPs, micelles, dendrimers, viral, albumin, polysaccharide, metallic and ceramic-based NPs (**Figure 1**). These NPs have shown therapeutic potential for almost every branch of medicine including oncology, cardiology and immunology^{1,10}.

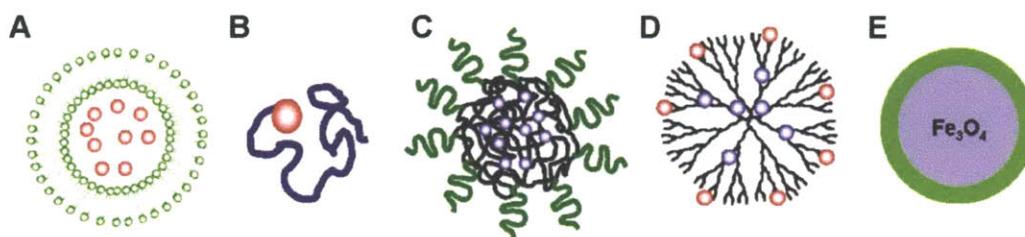


Figure 1. Schematic of therapeutic NP platforms in clinical and preclinical development.

(A) Liposome, (B) polymer-drug conjugate, (C) polymeric NP, (D) dendrimer, and (E) iron oxide NP. Red dots represent hydrophilic drugs and blue dots represent hydrophobic drugs. This figure was originally published in *Clinical Pharmacology and Therapeutics*. Zhang, L., Gu, F.X., Chan, J.M. *et al.* Nanoparticles in Medicine: Therapeutic Applications and Developments. *Clin Pharmacol Ther* 2008; 83: 761-9. © Nature Publishing Group.

In particular, biodegradable polymeric micelles with sizes of 10-200 nm (**Figure 1C**) have shown therapeutic potential as controlled-release drug delivery carriers¹¹. One example of a polymeric NP is Genexol-PM®, a PLGA-*b*-methoxyPEG micellar formulation of paclitaxel that has received regulatory approval in South Korea for clinical use, and which is currently undergoing phase II clinical trials for a number of cancer indications in the United States¹²⁻¹⁴. Polymeric micelles are formed by the spontaneous self-assembly of block copolymers consisting of two or more polymer chains with different hydrophobicity into core-shell micellar structures to minimize the system's free energy¹¹. In aqueous environments, the hydrophobic blocks form the core to minimize exposure to aqueous surroundings, whereas the hydrophilic blocks form the corona-like shell to stabilize the core through direct contact with water. This self-assembly process generates a functional micellar structure that is capable of carrying pharmaceuticals, especially poorly soluble drugs, in the hydrophobic core. The hydrophilic shell provides not only steric protection for the micelle, thereby increasing its stability in blood, but also functional end-groups suitable for further modification. In contrast with polymer-drug conjugates, each

polymeric micelle can carry more drugs per structure due to its relatively larger size and release these drugs in a more regulated manner via surface or bulk erosion of the biodegradable polymers, diffusion of the drug through the polymer matrix, or polymer swelling followed by drug diffusion. FDA-approved poly(D,L-lactic acid) (PLA)^{15,16}, poly(D,L-lactic-co-glycolic acid) (PLGA)¹⁷⁻²⁰ and poly(ϵ -caprolactone) (PCL)^{21,22} polymers diblocked or multiblocked with poly(ethylene glycol) (PEG) are the most extensively studied biodegradable polymers for micellar-based drug delivery and controlled release.

Barriers to Efficient Nanoparticle Delivery

In the design of NPs for systemic delivery, regardless which NP platform is chosen, there are a number of challenges to overcome in the blood circulation before therapeutic payloads can be delivered to their target site. Major barriers to NP-based therapeutic delivery can be characterized as follows (but not necessarily in chronological order):

1. Plasma stability and solubility
2. Dose-limiting toxicity (DLT) of NP formulation
3. Interaction with the reticulo-endothelial system (RES)
4. Opsonization and complement activation
5. Non-specific binding of serum proteins
6. Non-specific cellular uptake
7. Ease of internalization by target cells

A primary objective in the design of systemically delivered particles is RES avoidance, given that the RES itself is not the delivery target. Experimental evidence has shown that interaction with the RES may be modulated through key features such as NP size and surface-biocompatibility. Particles greater than 10 μm have been shown to cause embolization in the liver and lungs²³ and 3-4 μm sized particles have been shown to accumulate in the open circulation of the spleen²⁴. Hence, particles in the sub-micron range are preferred. A classic strategy to increase the circulation half-life and escape RES recognition, such as by liver Kupffer cells, consists of protecting the NP core with PEG polymer chains²⁵⁻²⁷. PEG is a highly hydrated

and flexible polymer chain that reduces plasma protein adsorption due to its surface inertness. PEG was studied as a potential surfactant for protein delivery as early as the 1960s²⁷ and was first introduced into clinical use in the early 1990s. PEG was shown to dramatically increase the circulation half-life of PLGA-PEG NPs from minutes to hours¹⁷ and has since been used in many systemically delivered polymeric systems. Studies have shown that PEG surface density, PEG chain length and PEG structure (linear versus branched) all influence the effectiveness of PEG towards NP surface-biocompatibility^{28,29}. For example, the molecular weight of the PEG segment varies typically between 2-5 kDa, the minimum lengths which are necessary for suppressing protein opsonization and complement activation. With sufficient PEG surface density, a mushroom-to-brush conformational transition occurs and the maximal effect of PEG surface-grafting can be observed by a combination of steric and electrostatic repulsion of serum albumins and complement proteins^{28,29}. PEG clearance does not require catabolism in the liver as the molecular weights used to confer sufficient shielding are below the cut-off size for renally filterable molecules (< 60 kDa)³⁰. Besides PEG, other linear polymers such as polyglutamic acid, polysaccharide, and poly(allylamine hydrochloride) have also been used to improve on NP surface-biocompatibility.

The size cut-off for NP localization at sites of disease has been attributed to a phenomenon called the enhanced permeability and retention (EPR) effect^{31,32}. EPR is the effect by which certain sizes of NPs tend to accumulate in tumors much more than in healthy tissue due to characteristic leaky blood vessels and dysfunctional lymphatic drainage from tumor angiogenesis^{33,34}. Using the EPR strategy for extravasation into tumor tissues, maximum NP diameters should be approximately 200 to 400 nm, smaller than the diameters of leaky endothelial cell fenestrations that range from 200 nm to 1.2 μm ^{35,36}. The surface charge of NPs must also be considered for the EPR effect. In a study of albumin surface charge, positively charged albumin macromolecules extravasated faster in solid tumors compared to anionic or neutral albumin³⁷. However, the rapid clearance of cationic molecules from the plasma suggests that the charge modification enhanced drug delivery to normal organs as well³⁸. Therefore, caution should be exercised when designing NP surface properties to improve drug delivery to solid tumors.

Once the particles have been delivered to its target site, they should be internalized by target cells if the aim is to release therapeutic agents within the cytosol (siRNA and drugs) or in the nucleus (gene delivery). The mode and efficiency of cellular uptake of NPs is strongly size-dependent³⁹⁻⁴¹. Small particles (< 500 nm) are internalized by receptor-mediated endocytosis, a process requiring a modest rearrangement of the cell cytoskeleton; whereas larger particles (> 1 μm) are internalized through a phagocytic process that requires an extensive rearrangement of the cell cytoskeleton and the formation of protruding actin filaments⁴². Taken together with size requirements for tumor delivery, the optimal NP radii should be kept under 150 nm to derive maximal tumor and cellular uptake efficiency.

First generation polymeric NPs have been designed to overcome barriers to effective therapeutic delivery. Although passive targeting approaches currently form the basis of clinical therapy, they suffer from several limitations. For instance, most drugs are incapable of distinguishing between benign and malignant cells, and consequently cause dose-limiting toxicities (DLT) during treatment. Also, solid tumors usually contain well-perfused, rapidly growing regions, and poorly perfused, necrotic areas^{43,44}. Hence, drugs may not be able to diffuse efficiently and ubiquitously throughout the tumor due to differential permeability of vessels in a single tumor. Elevated interstitial pressures due to poor lymphatic drainage may reduce extravasation of NPs into tumors and lead to a radial convection outward that opposes inward diffusion. Finally, tumors upregulate a number of transporter proteins of the ATP-binding cassette family to expel drugs from cells, causing multiple-drug resistance (MDR) and the failure of chemotherapy treatments⁴⁵.

Next Generation Nanoparticles: Targeted Nanoparticle Delivery

To overcome these limitations, second generation NPs have been designed to actively target specific cells for drug delivery. Keeping the previously described parameters of NP surface-biocompatibility and size constant, second generation NP systems may benefit from active binding interactions to tissues and organs of interest. This binding may be achieved by attaching targeting agents such as ligands – molecules that bind to specific receptors on the cell surface – to NPs by a variety of conjugation chemistries. Through differential targeting and uptake by a subset of cells, targeted NP systems in preclinical and clinical trials have improved the therapeutic index of drugs by two ways: (i) increasing the upper dose limit from the reduction of systemic toxicity, and/or (ii) reducing the dose required by enhancing local or intracellular drug concentration^{46,47}.

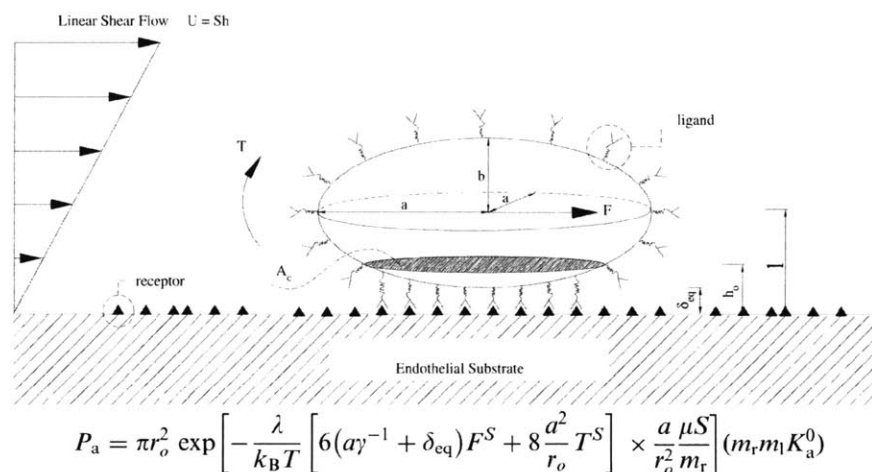


Figure 2. A theoretical model of NP targeting.

Modeling approach to the interaction of particles in specific contact with receptor substrates under linear laminar flow. P_a : adhesion strength parameter. This figure was originally published in *Biomaterials* by Decuzzi, P. and Ferrari, M. The adhesive strength of non-spherical particles mediated by specific interactions. *Biomaterials* 2006; 27: 5307-14. © Elsevier Limited Inc.

Taken conceptually to cover all classes of affinity ligands, researchers have developed a mathematical model^{48,49} in **Figure 2** predicting the adhesion probability (P_a) or the strength of NP adhesion based on three governing parameters: geometrical (radius of the particle, a ; shape aspect ratio, γ); biophysical (ligand-to-receptor surface density ratio, m_l/m_r ; equilibrium separation distance δ_{eq} between the substrate and the particle; the maximum distance h_o at which ligand–receptor bonds can be formed; shear stress at the blood vessel wall, μS) and biochemical (ligand–receptor binding affinity, K_a^o ; and characteristic length λ of the ligand–receptor bond). If conditions of dislodging forces (hydrodynamic shear stress and torque) are balanced by specific ligand-receptor interactions and non-specific adhesion forces at the cell-NP interface, firm adhesion is ensured. From there, the particles can release their payload to the extracellular matrix or be endocytosed. In short, this predictive model suggests that the targetability of NPs is defined by a myriad of parameters, namely size, shape, ligand affinity binding constant and both ligand and receptor densities. Thus, targeting cannot be simply defined by the ligand itself.

Along with theoretical models, NP targeting has been studied empirically for many years⁴⁷. The ligands studied range widely and are classified below as:

1. Small molecule ligands: vitamins (e.g. folic acid), carbohydrates (e.g. mannose, galactose).
2. Protein-based ligands: peptides, small proteins (e.g. transferrin), antibodies, antigen-binding fragments (F_{ab}), variant fragments (F_v), single-chain variant fragments (scF_v), and other types of antibody fragments.
3. Nucleic acid-based ligands: deoxynucleic acid (DNA) and ribonucleic acid (RNA) aptamers.

Given the large number of targeting ligands available, a logical route to select one ligand class over another may be desired. While there certainly may be reasons for a particular choice of ligand class, there is no straightforward process to reach that particular conclusion. A myriad of biological and physicochemical properties regarding the NP vehicle such as size, surface hydrophilicity and surface-density of the ligand have to be optimized in parallel, which together may impact the targeting efficacy of the surface-functionalized ligand.

Table 2 attempts to summarize the different classes of ligands based on their key properties and review their individual benefits and shortfalls for NP functionalization and targeting. The information presented in this table is subject to many exceptions, which is often the case with biological ligands.

	Properties	Small molecules (e.g. vitamins, carbohydrates)	Peptide	Antibody fragment	Antibody	Aptamer (DNA, RNA)
Biological properties:	Size (kDa)	< 1	~1-5	Affibody (~5-8) scFv (~20-40) etc.	~150	~20-40
	Stability	+++	+++	++	+	+
	Immune compatibility	+++	++	+	+	+
Biochemical properties:	Affinity constant, K_D (M)	$\geq 10^{-9} \sim 10^{-8}$	$\geq 10^{-8} \sim 10^{-6}$	$\geq 10^{-10} \sim 10^{-7}$	$\geq 10^{-10} \sim 10^{-7}$	$\geq 10^{-12}$ to 10^{-9}
	Binding selectivity	+	+	++	+++	+++
	Ease of discovery	+	+++	++	+	+
Manufacturing considerations:	Ease of synthesis; scale-up	+++	+++	++	+	+
	Cost	+	+	++	+++	+++

Table 2: Various classes of targeting ligands for NP surface-functionalization.

Parameters to be considered are classified as biological, biochemical and manufacturing. Information presented in this table gives a general guideline, and many exceptions are possible. Symbols: low (+), medium (++) and high (+++).

Biological parameters of size, stability and immune compatibility are important considerations when choosing a ligand class to functionalize onto NPs. Small molecules may be preferred for their low molecular weight, structural stability and integrity. For general immune compatibility, short peptides may evade getting processed onto major histocompatibility complexes (MHC) that trigger adaptive immune responses. Antibody engineering improvements have resulted in the production of smaller antibody fragments and chimeric, humanized antibodies (antibodies with both animal and human origins) to reduce the overall size and immunogenicity of non-human antibodies used in targeting⁵⁰. Larger double-stranded RNA or DNA aptamers, however, may interact with toll-like receptors on antigen-presenting cells (e.g. dendritic cells) and provoke an immune response. Hence, truncated versions of aptamers that contain only minimal flanking sequences around the active site have been designed to minimize aptamer size and reduce immune detection⁵¹. The stability of DNA and RNA aptamers may be considerably lower than small molecules and peptides as aptamers may be cleaved by

endogenous and non-specific nucleases in the blood. To reduce nuclease activity and improve aptamer stability, aptamers have been stabilized with 2'-fluoro-modified riboses on all pyrimidines and 3'-inverted deoxythymidine caps ("inverted T-cap")^{52,53}.

Biochemical parameters of binding affinity constants have a significant contribution to targeting efficacy. Binding affinity for a specific receptor, receptor isoform and even receptor on-off state can be dramatically improved with the use of ligands that not only show sequence complementarity but also three-dimensional (3D) structural conformation at the active site⁵¹. Antibody-based targeting been clinically successful with 22 different mAbs approved by the FDA by 2010, such as trastuzumab (Herceptin), an anti-HER2 mAb that binds to ErbB2 receptor for the treatment of breast cancer, and bevacizumab (Avastin), an anti-VEGF mAb that inhibits neoangiogenesis for the treatment of colorectal cancer⁵⁴. The affinity of peptides and fragments may be lower in comparison to antibodies and aptamers, and smaller ligands may less likely discriminate between minute differences in receptor on-off states or isoforms. However, affinity ligands are displayed at high densities on the surface of NPs and the collective binding from a multivalent interaction may result in improved targeting compared to a monovalent interaction. In one study, dendrimers conjugated to 3-15 folate molecules showed a 2,500- to 170,000-fold enhancement in binding affinity over free folate to immobilized receptors, which was attributed to the avidity effect from multiple folic acid groups⁵⁵. Hence, avidity can improve on, and in some cases compensate for, binding affinity when multiple ligands are functionalized onto NP surfaces. Furthermore, high binding affinities have been shown to decrease NP penetration into solid tumors due to a 'binding-site barrier', where NPs bind so strongly to their targets such that it prevents subsequent penetration into the tissue⁵⁶.

To discover new targeting ligands, it is important to be able to screen and enrich for high affinity binders in a cost-effective and efficient manner. Bacteriophage⁵⁷ and yeast⁵⁸ display libraries allow for the selection of high affinity peptides and scFv fragments *in vitro* and *in vivo*. For larger aptameric ligands, the SELEX (systematic evolution of ligands by exponential enrichment) technique can be used to screen combinatorial oligonucleotide libraries against target antigens^{59,60}. Recently, small molecule arrays have been developed to screen small molecule compounds against diverse targets including protein kinases, histone deacetylases, extracellular growth factors, and transcription factors⁶¹. One caution when screening for high

affinity ligands is that the selection for sub-nanomolar binding affinities may not necessarily improve on the selectivity for the target molecule⁶². Off-target binding to related molecules could lead to significant clinical effects.

Finally, *manufacturing considerations* are important if the targeted NP system is to be translated for clinical use. Generally, the scale-up of small-molecules and peptides is much more straightforward when compared to antibodies and aptamers. Furthermore, they are cost-effective for large-scale production, show high batch-to-batch consistency and retain ligand stability under various storage conditions. Not surprisingly, there are exceptions to the rule. Cyclic peptides contain a pair of cysteines spaced apart that are oxidized to form cyclic conformations. Concatemer formation and disulfide bond reduction may result in a loss of bioactivity, which makes the scale-up of cyclic peptides more difficult than for linear peptides.

In conclusion, there are a host of parameters to integrate before the choice of a particular ligand class – and the ligand itself – can be made. Hence, the selection of ligands for NP targeting is not a zero sum game, such that the gain or loss based on one parameter can be balanced equally by the gain or loss of another parameter. Rather, it is a delicate balance of parameters based on the therapeutic requirements for the disease to be treated.

Moving Beyond the Targeting Paradigm

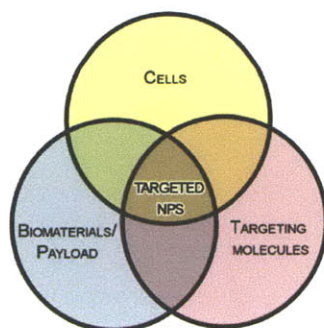


Figure 3. Targeting paradigm.

Targeted NPs have traditionally been directed against cell-based receptors to release a payload (hydrophobic drugs, proteins, plasmids and siRNA).

Traditionally, NPs have been targeted against cellular-based receptors (**Figure 3**). Antibodies have been directed against the upregulated Erb2 receptor⁶³ in breast tumors and the upregulated PSMA antigen in prostate tumors⁶⁴. The extracellular matrices (ECM) which surround and support cells have also been studied and applied as a source for targeting ligands against cell surface receptors overexpressed in tumors⁶⁵. For example, hyaluronan (HA) has been coated onto liposomes to improve circulation time and enhance targeting to HA receptor-expressing tumors *in vivo*⁶⁶. A classic example is the use of RGD (arg-gly-asp) tripeptide motifs which are found ubiquitously throughout the ECM on matrix proteins such as fibronectin. RGD peptides and their mimetics have been successfully used to target liposomes and polymeric NPs to cancer cells with upregulated integrin receptors⁶⁷.

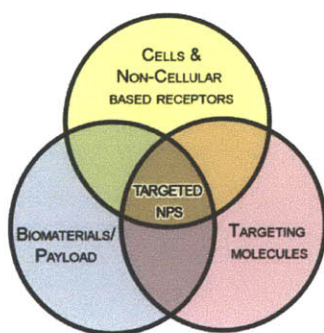


Figure 4. New targeting paradigm.

Researchers are now exploring non-cellular protein epitopes in the ECM and basement membrane to overcome the heterogeneity of cell-surface receptor expression in disease. Targeting of matrix proteins may generate an extracellular depot for the payload to be released into solid tumors and atherosclerotic plaques.

More recently, investigators have explored abundant non-cellular targets in the ECM for targeting in human disease (**Figure 4**). Many oncologic, cardiovascular and regenerative diseases are associated with compromised vasculature and increased vascular permeability³³. Hence, researchers have come up with original ways to utilize this pathology for the treatment of disease.

As a novel approach to anti-angiogenic therapy, researchers have attempted to modulate the angiogenic process and generate locally non-permissive basement membranes by disrupting crucial interactions within the matrix⁶⁸. For example, the use of blocking therapeutic ligands against MMP2-processed collagen IV inhibited angiogenesis *in vivo*⁶⁹. The breach of the endothelial layer may also be exploited as a high-capacity surface for targeting the underlying

basement membrane. Various conjugates and NPs have been targeted to fibrin⁷⁰, laminin^{71,72}, collagen I⁷³ and collagen II α 1⁷⁴ for both therapeutic drug delivery and imaging. Targeting of the ECM provides a number of benefits over cell receptor-based targeting as it may overcome intra- and inter-patient heterogeneity of cell-surface receptor expression found in tumors⁷⁵. Advances in molecular profiling of tumors have revealed substantial heterogeneity in both histological and expression phenotypes of cancerous cells⁷⁶. Targeting efforts against the HER2/neu epidermal growth factor receptor may be hampered by intratumoral heterogeneity associated with subclonal diversity of Her2 amplified tumor cells found in 5-30% of tumors^{77,78}. Besides the upregulated α v β 3 integrin receptors on cancer cells, RGD peptides have also been shown to bind to α 5 β 1 and α 4 β 1 integrins which are not specific to cancer cells⁷⁹. Hence, the heterogeneity observed in tumors may make it difficult to discriminate cancer cells from healthy cells through the targeting of cellular receptors. Potentially, targeting the underlying ECM exposed in disease may overcome these issues.

Outlook

More complex multimodal NP systems that are concurrently capable of targeting, imaging and therapy are the subject of intense research in nanotechnology. Researchers have improved on the functionality of NPs with the addition of targeting ligands and controlled release capacity to achieve the spatiotemporal control that is essential to many medical applications. A myriad of functionalities can be assembled into one system, but NPs must be precisely engineered with an optimal mix of physicochemical and biological properties to achieve an effective design.

Indeed, this has been the bottleneck for the translation of targeted NPs into clinical practice. Hence, even though the earliest targeted liposome was described in 1980⁸⁰, only a handful of systems have ever made it to clinical trials and none have been clinically approved. We expect the role of targeted nanotechnology as a diagnostic and therapeutic tool in the clinic to become more prominent as more effective multifunctional systems are designed, as formulations become more economically viable and as their long-term safety can be guaranteed.

References

1. Zhang, L., *et al.* Nanoparticles in medicine: therapeutic applications and developments. *Clin Pharmacol Ther* **83**, 761-769 (2008).
2. Farokhzad, O.C. & Langer, R. Nanomedicine: developing smarter therapeutic and diagnostic modalities. *Adv Drug Deliv Rev* **58**, 1456-1459 (2006).
3. Potineni, A., Lynn, D.M., Langer, R. & Amiji, M.M. Poly(ethylene oxide)-modified poly(beta-amino ester) nanoparticles as a pH-sensitive biodegradable system for paclitaxel delivery. *J Control Release* **86**, 223-234 (2003).
4. Yoo, H.S., Lee, E.A. & Park, T.G. Doxorubicin-conjugated biodegradable polymeric micelles having acid-cleavable linkages. *J Control Release* **82**, 17-27 (2002).
5. Jia, J., *et al.* Mechanisms of drug combinations: interaction and network perspectives. *Nat Rev Drug Discov* **8**, 111-128 (2009).
6. Wagner, V., Dullaart, A., Bock, A.K. & Zweck, A. The emerging nanomedicine landscape. *Nat Biotechnol* **24**, 1211-1217 (2006).
7. Torchilin, V.P. Recent advances with liposomes as pharmaceutical carriers. *Nat Rev Drug Discov* **4**, 145-160 (2005).
8. Duncan, R. Polymer conjugates as anticancer nanomedicines. *Nat Rev Cancer* **6**, 688-701 (2006).
9. Harris, J.M. & Chess, R.B. Effect of pegylation on pharmaceuticals. *Nat Rev Drug Discov* **2**, 214-221 (2003).
10. Davis, M.E., Chen, Z.G. & Shin, D.M. Nanoparticle therapeutics: an emerging treatment modality for cancer. *Nat Rev Drug Discov* **7**, 771-782 (2008).
11. Torchilin, V.P. Micellar nanocarriers: pharmaceutical perspectives. *Pharm Res* **24**, 1-16 (2007).
12. Kim, T.Y., *et al.* Phase I and pharmacokinetic study of Genexol-PM, a cremophor-free, polymeric micelle-formulated paclitaxel, in patients with advanced malignancies. *Clin Cancer Res* **10**, 3708-3716 (2004).
13. Kim, D.W., *et al.* Multicenter phase II trial of Genexol-PM, a novel Cremophor-free, polymeric micelle formulation of paclitaxel, with cisplatin in patients with advanced non-small-cell lung cancer. *Ann Oncol* **18**, 2009-2014 (2007).
14. Lee, K.S., *et al.* Multicenter phase II trial of Genexol-PM, a Cremophor-free, polymeric micelle formulation of paclitaxel, in patients with metastatic breast cancer. *Breast Cancer Res Treat* **108**, 241-250 (2008).
15. Stolnik, S., *et al.* Surface modification of poly(lactide-co-glycolide) nanospheres by biodegradable poly(lactide)-poly(ethylene glycol) copolymers. *Pharm Res* **11**, 1800-1808 (1994).
16. Bazile, D., *et al.* Stealth Me.PEG-PLA nanoparticles avoid uptake by the mononuclear phagocytes system. *J Pharm Sci* **84**, 493-498 (1995).
17. Gref, R., *et al.* Biodegradable long-circulating polymeric nanospheres. *Science* **263**, 1600-1603 (1994).
18. Farokhzad, O.C., *et al.* Targeted nanoparticle-aptamer bioconjugates for cancer chemotherapy in vivo. *Proc Natl Acad Sci U S A* **103**, 6315-6320 (2006).
19. Cheng, J., *et al.* Formulation of functionalized PLGA-PEG nanoparticles for in vivo targeted drug delivery. *Biomaterials* **28**, 869-876 (2007).

20. Li, Y., *et al.* PEGylated PLGA nanoparticles as protein carriers: synthesis, preparation and biodistribution in rats. *J Control Release* **71**, 203-211 (2001).
21. Kim, S.Y., Shin, I.G., Lee, Y.M., Cho, C.S. & Sung, Y.K. Methoxy poly(ethylene glycol) and epsilon-caprolactone amphiphilic block copolymeric micelle containing indomethacin. II. Micelle formation and drug release behaviours. *J Control Release* **51**, 13-22 (1998).
22. Shin, I.G., Kim, S.Y., Lee, Y.M., Cho, C.S. & Sung, Y.K. Methoxy poly(ethylene glycol)/epsilon-caprolactone amphiphilic block copolymeric micelle containing indomethacin. I. Preparation and characterization. *J Control Release* **51**, 1-11 (1998).
23. Brown, K.T. Fatal pulmonary complications after arterial embolization with 40-120-micrometre tris-acryl gelatin microspheres. *J Vasc Interv Radiol* **15**, 197-200 (2004).
24. Westedt, U., *et al.* Deposition of nanoparticles in the arterial vessel by porous balloon catheters: localization by confocal laser scanning microscopy and transmission electron microscopy. *AAPS PharmSci* **4**, E41 (2002).
25. Moghimi, S.M., Hunter, A.C. & Murray, J.C. Long-circulating and target-specific nanoparticles: theory to practice. *Pharmacol Rev* **53**, 283-318 (2001).
26. Moghimi, S.M. & Szebeni, J. Stealth liposomes and long circulating nanoparticles: critical issues in pharmacokinetics, opsonization and protein-binding properties. *Prog Lipid Res* **42**, 463-478 (2003).
27. Davis, F.F. The origin of pegnology. *Adv Drug Deliv Rev* **54**, 457-458 (2002).
28. Gref, R., *et al.* 'Stealth' corona-core nanoparticles surface modified by polyethylene glycol (PEG): influences of the corona (PEG chain length and surface density) and of the core composition on phagocytic uptake and plasma protein adsorption. *Colloids Surf B Biointerfaces* **18**, 301-313 (2000).
29. Fang, C., *et al.* In vivo tumor targeting of tumor necrosis factor-alpha-loaded stealth nanoparticles: effect of MePEG molecular weight and particle size. *Eur J Pharm Sci* **27**, 27-36 (2006).
30. Behr, T.M., *et al.* Reduction of the renal uptake of radiolabeled monoclonal antibody fragments by cationic amino acids and their derivatives. *Cancer Res* **55**, 3825-3834 (1995).
31. Matsumura, Y. & Maeda, H. A new concept for macromolecular therapeutics in cancer chemotherapy: mechanism of tumorotropic accumulation of proteins and the antitumor agent smancs. *Cancer Res* **46**, 6387-6392 (1986).
32. Maeda, H., Wu, J., Sawa, T., Matsumura, Y. & Hori, K. Tumor vascular permeability and the EPR effect in macromolecular therapeutics: a review. *J Control Release* **65**, 271-284 (2000).
33. Folkman, J. Angiogenesis: an organizing principle for drug discovery? *Nat Rev Drug Discov* **6**, 273-286 (2007).
34. Jain, R.K. Transport of molecules, particles, and cells in solid tumors. *Annu Rev Biomed Eng* **1**, 241-263 (1999).
35. Hobbs, S.K., *et al.* Regulation of transport pathways in tumor vessels: role of tumor type and microenvironment. *Proc Natl Acad Sci U S A* **95**, 4607-4612 (1998).
36. Yuan, F., *et al.* Vascular permeability in a human tumor xenograft: molecular size dependence and cutoff size. *Cancer Res* **55**, 3752-3756 (1995).

37. Dellian, M., Yuan, F., Trubetskoy, V.S., Torchilin, V.P. & Jain, R.K. Vascular permeability in a human tumour xenograft: molecular charge dependence. *Br J Cancer* **82**, 1513-1518 (2000).
38. Verma, A. & Stellacci, F. Effect of surface properties on nanoparticle-cell interactions. *Small* **6**, 12-21.
39. Zhang, S., Li, J., Lykotrafitis, G., Bao, G. & Suresh, S. Size-Dependent Endocytosis of Nanoparticles. *Adv Mater Deerfield* **21**, 419-424 (2009).
40. Jiang, W., Kim, B.Y.S., Rutka, J.T. & Chan, W.C.W. Nanoparticle-mediated cellular response is size-dependent. *Nature Nanotechnology* **3**, 145-150 (2008).
41. Chithrani, B.D., Ghazani, A.A. & Chan, W.C. Determining the size and shape dependence of gold nanoparticle uptake into mammalian cells. *Nano Lett* **6**, 662-668 (2006).
42. Decuzzi, P., Pasqualini, R., Arap, W. & Ferrari, M. Intravascular delivery of particulate systems: does geometry really matter? *Pharm Res* **26**, 235-243 (2009).
43. Jain, R.K. & Baxter, L.T. Mechanisms of heterogeneous distribution of monoclonal antibodies and other macromolecules in tumors: significance of elevated interstitial pressure. *Cancer Res* **48**, 7022-7032 (1988).
44. Jain, R.K. Delivery of molecular and cellular medicine to solid tumors. *Adv Drug Deliv Rev* **46**, 149-168 (2001).
45. Gottesman, M.M., Fojo, T. & Bates, S.E. Multidrug resistance in cancer: role of ATP-dependent transporters. *Nat Rev Cancer* **2**, 48-58 (2002).
46. Allen, T.M. Ligand-targeted therapeutics in anticancer therapy. *Nat Rev Cancer* **2**, 750-763 (2002).
47. Peer, D., *et al.* Nanocarriers as an emerging platform for cancer therapy. *Nat Nanotechnol* **2**, 751-760 (2007).
48. Decuzzi, P. & Ferrari, M. The adhesive strength of non-spherical particles mediated by specific interactions. *Biomaterials* **27**, 5307-5314 (2006).
49. Decuzzi, P. & Ferrari, M. Design maps for nanoparticles targeting the diseased microvasculature. *Biomaterials* **29**, 377-384 (2008).
50. Riechmann, L., Clark, M., Waldmann, H. & Winter, G. Reshaping human antibodies for therapy. *Nature* **332**, 323-327 (1988).
51. Dassie, J.P., *et al.* Systemic administration of optimized aptamer-siRNA chimeras promotes regression of PSMA-expressing tumors. *Nat Biotechnol* **27**, 839-849 (2009).
52. Keefe, A.D. & Cload, S.T. SELEX with modified nucleotides. *Curr Opin Chem Biol* **12**, 448-456 (2008).
53. White, R.R., Sullenger, B.A. & Rusconi, C.P. Developing aptamers into therapeutics. *J Clin Invest* **106**, 929-934 (2000).
54. Reichert, J.M., Rosensweig, C.J., Faden, L.B. & Dewitz, M.C. Monoclonal antibody successes in the clinic. *Nat Biotechnol* **23**, 1073-1078 (2005).
55. Hong, S., *et al.* The binding avidity of a nanoparticle-based multivalent targeted drug delivery platform. *Chem Biol* **14**, 107-115 (2007).
56. Adams, G.P., *et al.* High affinity restricts the localization and tumor penetration of single-chain fv antibody molecules. *Cancer Res* **61**, 4750-4755 (2001).
57. Devlin, J.J., Panganiban, L.C. & Devlin, P.E. Random peptide libraries: a source of specific protein binding molecules. *Science* **249**, 404-406 (1990).

58. Boder, E.T. & Wittrup, K.D. Yeast surface display for screening combinatorial polypeptide libraries. *Nat Biotechnol* **15**, 553-557 (1997).
59. Ellington, A.D. & Szostak, J.W. In vitro selection of RNA molecules that bind specific ligands. *Nature* **346**, 818-822 (1990).
60. Tuerk, C. & Gold, L. Systematic evolution of ligands by exponential enrichment: RNA ligands to bacteriophage T4 DNA polymerase. *Science* **249**, 505-510 (1990).
61. Vegas, A.J., Fuller, J.H. & Koehler, A.N. Small-molecule microarrays as tools in ligand discovery. *Chemical Society Reviews* **37**, 1385-1394 (2008).
62. Carothers, J.M., Oestreich, S.C. & Szostak, J.W. Aptamers selected for higher-affinity binding are not more specific for the target ligand. *J Am Chem Soc* **128**, 7929-7937 (2006).
63. Park, J.W., *et al.* Anti-HER2 immunoliposomes: enhanced efficacy attributable to targeted delivery. *Clin Cancer Res* **8**, 1172-1181 (2002).
64. Milowsky, M.I., *et al.* Vascular targeted therapy with anti-prostate-specific membrane antigen monoclonal antibody J591 in advanced solid tumors. *J Clin Oncol* **25**, 540-547 (2007).
65. Kalluri, R. Basement membranes: structure, assembly and role in tumour angiogenesis. *Nat Rev Cancer* **3**, 422-433 (2003).
66. Eliaz, R.E. & Szoka, F.C., Jr. Liposome-encapsulated doxorubicin targeted to CD44: a strategy to kill CD44-overexpressing tumor cells. *Cancer Res* **61**, 2592-2601 (2001).
67. Nasongkla, N., *et al.* cRGD-functionalized polymer micelles for targeted doxorubicin delivery. *Angew Chem Int Ed Engl* **43**, 6323-6327 (2004).
68. Sanz, L. & Alvarez-Vallina, L. The extracellular matrix: a new turn-of-the-screw for anti-angiogenic strategies. *Trends Mol Med* **9**, 256-262 (2003).
69. Mueller, J., Gaertner, F.C., Blechert, B., Janssen, K.P. & Essler, M. Targeting of tumor blood vessels: a phage-displayed tumor-homing peptide specifically binds to matrix metalloproteinase-2-processed collagen IV and blocks angiogenesis in vivo. *Mol Cancer Res* **7**, 1078-1085 (2009).
70. Peters, D., *et al.* Targeting atherosclerosis by using modular, multifunctional micelles. *Proc Natl Acad Sci U S A* (2009).
71. Cuesta, A.M., *et al.* In vivo tumor targeting and imaging with engineered trivalent antibody fragments containing collagen-derived sequences. *PLoS One* **4**, e5381 (2009).
72. Sanz, L., Kristensen, P., Russell, S.J., Ramirez Garcia, J.R. & Alvarez-Vallina, L. Generation and characterization of recombinant human antibodies specific for native laminin epitopes: potential application in cancer therapy. *Cancer Immunol Immunother* **50**, 557-565 (2001).
73. O'Neil, C.P., *et al.* Extracellular matrix binding mixed micelles for drug delivery applications. *J Control Release* (2009).
74. Rothenfluh, D.A., Bermudez, H., O'Neil, C.P. & Hubbell, J.A. Biofunctional polymer nanoparticles for intra-articular targeting and retention in cartilage. *Nat Mater* **7**, 248-254 (2008).
75. Fidler, I.J. Review: biologic heterogeneity of cancer metastases. *Breast Cancer Res Treat* **9**, 17-26 (1987).
76. Rajan, P., Elliott, D.J., Robson, C.N. & Leung, H.Y. Alternative splicing and biological heterogeneity in prostate cancer. *Nat Rev Urol* **6**, 454-460 (2009).

77. Wu, J.M., *et al.* Heterogeneity of breast cancer metastases: comparison of therapeutic target expression and promoter methylation between primary tumors and their multifocal metastases. *Clin Cancer Res* **14**, 1938-1946 (2008).
78. Vance, G.H., *et al.* Genetic heterogeneity in HER2 testing in breast cancer: panel summary and guidelines. *Arch Pathol Lab Med* **133**, 611-612 (2009).
79. Ruoslahti, E. & Pierschbacher, M.D. New perspectives in cell adhesion: RGD and integrins. *Science* **238**, 491-497 (1987).
80. Heath, T.D., Fraley, R.T. & Papahdjopoulos, D. Antibody targeting of liposomes: cell specificity obtained by conjugation of F(ab')₂ to vesicle surface. *Science* **210**, 539-541 (1980).

Chapter 2. Design and Engineering of Hybrid Lipid-Polymeric Core-Shell Nanoparticles.

Abstract

Current approaches to encapsulate and deliver therapeutic compounds have focused on developing liposomal and biodegradable polymeric nanoparticles (NPs), resulting in clinically approved therapeutics such as Doxil/Caelyx and Genexol-PM, respectively. Given the clinical success of liposomes and polymeric NPs, we hypothesized that the development of a hybrid may combine their individual strengths. We report the design and engineering of lipid-polymer hybrid NPs as a robust drug delivery platform. These core-shell NPs consist of three distinct functional components: (i) a hydrophobic polymeric core, (ii) a hydrophilic polymeric shell and (iii) a soybean lecithin monolayer at the core-shell interface. The NPs were synthesized by a single-step nanoprecipitation method combined with self-assembly in a reproducible and predictable manner, making it potentially suitable for scale-up. Herein we report the formulation parameters that alter their physicochemical characteristics, plasma stability, drug release rates and cytotoxicity values. Our data suggests that the lipid-polymeric core-shell NPs may be a useful new controlled release drug delivery system.

The content of this chapter has been published in whole or in part in the following journal articles:

Zhang, L., Chan, J.M., Gu, F.X., Rhee, J.W., Wang, A.Z., Radovic-Moreno, A.F., Alexis, F., Langer, R. Farokhzad, O.C. Self-assembled lipid-polymer hybrid nanoparticles: a robust drug delivery platform. *ACS Nano* (2008). **2**, 1696-1702. Reproduced with permission from ACS Nano. American Chemical Society © 2008.

Chan, J.M., Zhang, L., Yuet, K.P., Liao, G., Rhee, J.W., Langer, R., Farokhzad, O.C. PLGA-lecithin-PEG core-shell nanoparticles for controlled drug delivery. *Biomaterials* (2009). **30**, 1627-1634. Reproduced with permission from Biomaterials. Elsevier Limited Inc. © 2009.

Introduction

The clinical use of liposomes as drug delivery vehicles began in 1995 when Doxil®/Caelyx®, the first liposomal drug formulation encapsulating doxorubicin, was FDA-approved for the treatment of AIDS-related Kaposi's sarcoma^{1,2}. Subsequently, more liposomal formulations were approved and Doxil was also permitted for use in oncologic indications such as ovarian cancer and multiple myeloma. Liposomes are spherical lipid vesicles with a bilayer membrane of natural or synthetic amphiphilic lipid molecules. They show favorable safety profiles and systemic circulation half-lives that can reach days after being surface modified with hydrophilic polymers such as poly(ethylene glycol) (PEG)^{3,4}. However, due to their hydrophilic interiors, the loading of poorly water-soluble drugs into liposomes is limited.

Polymeric NPs, especially those which are formulated with biocompatible and biodegradable polymers, are being increasingly applied in both academic and clinical medicine⁵. Polymeric NPs are advantageous for their ability to load hydrophobic drugs with high capacity and to control drug release based on the polymer chosen. One such example is Genexol-PM®, a PLGA- β -methoxyPEG paclitaxel-encapsulated micelle approved for metastatic breast cancer therapy in South Korea⁶⁻⁸.

Not surprisingly, previous hybrids of lipid and polymer materials have been designed to take advantage of their individual strengths. In these studies, polymeric NPs were mixed with liposomes to form lipid-polymer complexes (lipopolyplexes) where the lipid bilayer or lipid multilayer was fused onto the surface of polymeric NPs⁹⁻¹¹. In one such formulation, doxorubicin-polymer conjugates were encapsulated in PEGylated lipid shells and delivered to the neovasculature of tumors *in vivo*¹². All of these complexes were made by a two-step formulation process: (i) synthesis of polymeric NP cores, and (ii) encapsulation of polymeric NPs within liposomes that were rehydrated and extruded from lipid membranes. The two-step synthesis of polymer cores followed by liposome extrusion gives poor control over the final NP structure and this may ultimately hinder clinical translation. It is desirable to develop lipid-polymer hybrid NPs that are well-defined and require a single-step formulation method to facilitate future scale-up.

In this study, we design sub-100 nm lipid-polymer hybrid NPs through a combination of nanoprecipitation and self-assembly. The NPs are comprised of (i) a biodegradable hydrophobic polymeric core that can encapsulate poorly water-soluble drugs and release them at a sustained rate, (ii) an antibiofouling hydrophilic shell to enhance NP stability, evade recognition by the immune system and increase systemic circulation half-life, and (iii) a lipid monolayer at the core-shell interface to prevent both drug diffusion out of the core and water penetration into the core, thereby slowing drug release from the NPs and preventing NP degradation.

Towards the goal of finding an optimal hybrid NP formulation, we evaluate parameters that affect the core-shell nanostructure. Subsequently, we characterize the NPs for physical stability, controlled drug release kinetics, post-formulation purification, long-term storage and material cytotoxicity. Various formulation parameters such as the lipid/polymer mass ratio and lipid/lipid-PEG molar ratio control NP physical stability, size and surface zeta-potential. We encapsulate docetaxel (Dtxl) in the NPs and show that changing the amount of lipid coverage affects drug release kinetics, establishing the role of the lipid monolayer in the hybrid NPs. Next, we demonstrate a potentially scalable process for the formulation, purification, and storage of NPs. Finally, the biocompatibility of these NPs *in vitro* is evaluated using MTT assays on two model human cell lines, HeLa and HepG2. This hybrid NP system may represent a new way of combining existing lipid and polymer materials for controlled drug delivery applications.

Methods

Materials.

Poly(D,L-lactide-co-glycolic acid) (PLGA) with a 50:50 monomer ratio, ester-terminated, and viscosity of 0.72–0.92 dl/g was purchased from Durect Corporation (Pelham, AL). Soybean lecithin consisting of 90–95% phosphatidylcholine (soybean phosphatidylcholine, sPC) was obtained from MP Biomedicals (Solon, OH). DSPE–PEG–COOH (1,2-distearoyl-*sn*-glycero-3-phosphoethanolamine-N-carboxy(polyethylene glycol)2000) was obtained from Avanti (Alabaster, AL). All organic solvents, docetaxel (Dtx1) and bovine serum albumin (BSA) were purchased from Sigma-Aldrich (St Louis, MO).

Synthesis of PLGA–lipid–PEG NPs.

NPs were synthesized from PLGA, soybean lecithin and DSPE–PEG–COOH using a modified nanoprecipitation technique combined with self-assembly. PLGA was first dissolved in organic solvent (acetonitrile, unless specified) with concentrations ranging from 1 to 25 mg/mL. Lecithin and DSPE–PEG–COOH (7:3, molar ratio) were dissolved in a 3 mL 4% ethanol aqueous solution at 20% of the PLGA polymer weight and heated to 65 °C to ensure all lipids were in the liquid phase. The PLGA/acetonitrile solution was then added dropwise into the preheated lipid aqueous solution (1 mL/min) under gentle stirring followed by vigorous vortexing for 3 min. The NPs were allowed to self-assemble for 2 h at room temperature (RT) with continuous gentle stirring for solvent evaporation. The remaining organic solvent and free molecules were removed by washing the NP solution three times using a 10 kDa MWCO Amicon Ultra-4 centrifugal filter (Millipore, Billerica, MA) before resuspending the NPs in water to obtain a final desired concentration. The NPs were used immediately, stored at 4 °C or snap frozen in liquid nitrogen and lyophilized for long-term storage at -80 °C.

NP Size and Surface Charge Characterization.

NP size (diameter, nm), polydispersity index and surface charge (zeta potential, mV) were determined by quasi-elastic laser light scattering using a ZetaPALS dynamic light scattering (DLS) detector (15 mW laser, incident beam=676 nm; Brookhaven Instruments Corporation, Holtsville, NY) at RT. Viscosity and refraction indices were set equal to those specific of water. Particle concentration was calculated based on the PLGA polymer concentration in the NPs.

Transmission Electron Microscopy (TEM) Characterization.

TEM experiments were carried out on a JEOL JEM-200CX instrument at an acceleration voltage of 200 kV. TEM samples were prepared by administering the NP suspension (2 mg/mL) onto 300-mesh Formvar-coated copper grids that had previously been hydrophilized under UV light (Electron Microscopy Sciences, Hatfield, PA). Samples were blotted away after 30 min and the grids were negatively stained for 10 min at RT with freshly prepared and sterile-filtered 3% (w/v) uranyl acetate solution. The grids were washed twice with distilled water and air dried prior to imaging.

Drug Loading and Release Kinetics.

To prepare drug-encapsulated NPs, Dtx1 at 10 wt% of the polymer was dissolved into the PLGA/acetonitrile solution before nanoprecipitation. To measure the drug loading yield and release profile of Dtx1 from each type of NP, 3 mL NP solutions at a concentration of 0.5 mg/mL were split equally into 30 Slide-A-Lyzer MINI dialysis microtubes, 10 kDa MWCO (Pierce, Rockford, IL) and dialyzed against 3 L distilled water at RT. Distilled water was changed periodically during the dialysis process. At the indicated times, the total solution in each microtube was recorded (n=3) and 0.1 mL of the solution per tube was mixed with an equal volume of acetonitrile to dissolve the NPs. The Dtx1 content was quantified by reverse-phase high performance liquid chromatography (RP-HPLC) using an Agilent 1100 HPLC (Paolo Alto, CA) equipped with a pentafluorophenyl column (Curosil-PFP, 250 x 4.6 mm, 5 µm; Phenomenex, Torrance, CA). Dtx1 absorbance was measured at 227 nm using a UV-Vis detector with a retention time of ~12-14 min in a 1 mL/min 50/50 acetonitrile/water non-gradient mobile

phase. The Dtxl content per microtube was calculated for the actual volume from the 0.1 mL sample measured.

NP In Vitro Stability.

NPs at a polymer concentration of 1 mg/mL were incubated with 10 vol% BSA and 10 vol% human plasma (BioChemMed, Winchester, VA) solutions at 37 °C under gentle stirring. At each time point, an aliquot was collected for NP size measurements. DLS measurements were performed in triplicate at RT.

NP Cytotoxicity Assays.

NP cytotoxicity was evaluated using MTT assays. HeLa and HepG2 cells were cultured in DMEM supplemented with 10% heat-inactivated FBS, 100 units/mL penicillin and 100 µg/mL streptomycin at 5% CO₂, 37 °C. Cells were seeded for 24 h in a 96-well plate at densities of 10,000 cells/well. The media was replaced with 200 µL of media-containing NPs at the required concentrations and incubated for 24 h in triplicate. The NP/media was aspirated and 0.5 mg/mL of MTT solution in media was incubated with the cells for another 4 h. The MTT containing media was removed and cells were rinsed three times with PBS. 200 µL of isopropanol/DMSO was added in a 1:1 ratio for 5 min at 37 °C to lyse the cells. MTT absorbance was measured at 570 nm against a reference wavelength of 660 nm using a SpectraMax Plus 384 microplate spectrophotometer (Molecular Devices, Sunnyvale, CA). Higher MTT absorbance values with background subtraction indicate higher relative cell viability. The results were plotted on a graph and fitted using the OriginPro 8 software (OriginLab Corp, Northampton, MA).

PLGA–Lipid–PEG Microparticle Synthesis and Self-Assembly.

50 mg of PLGA in 4 mL of ethyl acetate was added to 1 mg DSPE–PEG2000–COOH in 8 mL of 4% EtOH solution. Alternatively, 1.7 mg DSPE–PEG3400–COOH (Laysan Bio, Arab, AL) can be used to replace DSPE–PEG2000–COOH (molar ratio kept constant). The PLGA/DSPE–PEG mixture was homogenized for ~1 min at 9,000-10,000 rpm with a L4RTA Homogenizer and Mixer (Silverson Inc., East Longmeadow, MA). The resulting emulsion was immediately added to 50 mL of DI H₂O and magnetically stirred overnight (~12-16 h) to evaporate the solvent and self-assemble the microparticles (MPs). The MPs were washed three times using a 100 kDa MWCO Amicon filter.

Scanning Electron Microscopy (SEM) Characterization.

Samples were dried on a silicon wafer chip overnight. After drying, samples were mounted on an aluminum stub using double sided carbon tape and sputter-coated with a thin gold-palladium film using an automated sputter coater. Samples were imaged with a JEOL JSM 6060 scanning microscope (Peabody, MA) using a 2.5-5 kV accelerating voltage at 10-mm working distances.

Results

Self-assembly of PLGA–lipid–PEG NPs.

As shown schematically in **Figure 1A**, the lipid-polymer hybrid NPs are self-assembled from PLGA, lecithin and DSPE–PEG conjugates through a single-step nanoprecipitation method. Specifically, the PLGA polymers precipitate to form a hydrophobic core to encapsulate poorly water-soluble drugs, while lecithin and DSPE–PEG in the appropriate molar ratio form a lipid monolayer and PEG shell around the PLGA polymeric core. Dtxl, a model chemotherapy drug, was used for drug encapsulation in all subsequent studies.

The lipids were heated at 65 °C before adding the Dtxl/PLGA mixture and vortexing for 3 min. The increase in thermal and mechanical energy causes the lipids to disperse and self-assemble as a monolayer around the PLGA/organic solvent core to shield their hydrophobic fatty acid tails. After 2 h, self-assembly and solvent evaporation was considered complete (**Figure 1A**). To remove the residual solvent and free lipid molecules, the NPs were purified either by ultracentrifugation or dialysis prior to characterization.

Characterization of PLGA–lipid–PEG NP Properties.

DLS measurements were taken to characterize NP hydrodynamic size, polydispersity and zeta potential of each preparation. The average diameter of synthesized NPs ranged between 60 and 70 nm. The zeta potential ranged between -40 mV and -60 mV in water, depending on the size and composition of the NPs. The negative zeta potential values measured here will appear closer to neutral in PBS buffers from charge screening. NP sizes and zeta potentials remained in the same range with or without Dtxl loading. A schematic shows the core–shell structure of the NPs (**Figure 1B**).

To characterize the structure of the NPs, samples were negatively stained by uranyl acetate and imaged by transmission electron microscopy (TEM) (**Figure 1C**). The TEM images revealed that the NPs are dispersed as sub-100 nm particles with a well-defined spherical shape, and that the incorporation of Dtxl did not appear to cause morphological changes.

PLGA–lipid–PEG NP Lipid Formulation Parameters.

The lipid/polymer weight ratio may be changed to fine-tune NP size (diameter, nm) and surface charge (ζ potential, mV) for optimal NP compatibility *in vivo*.

Taking PLGA/acetonitrile concentration (1mg/mL of 0.82 dl/g PLGA) and lipid/lipid–PEG molar ratio (9:1) to be constant, we first investigated the effect of total lipid (lecithin + DSPE–PEG–COOH)/polymer mass ratio on NP size. At 0% total lipid/polymer mass ratio, the formulation of pure PLGA NPs aggregated immediately in PBS to form $\sim 2 \mu\text{m}$ particles. An increase in total lipid/polymer mass ratio to 10%, 15%, 20%, or 100% did not affect the $\sim 2 \mu\text{m}$ aggregation (**Figure 2**). This suggests that even good coverage of the PLGA polymeric core by a lipid monolayer is insufficient for charge screening in PBS buffers. Next, we investigated the effect of lipid/lipid–PEG (lecithin/DSPE–PEG–COOH) molar ratio on NP size. We expanded our study to include lipid/lipid–PEG molar ratios of 8:2, 7.5:2.5 or 7:3, against total lipid/polymer mass ratios of 10%, 15% or 20% (**Figure 2**). In contrast to the $\sim 2 \mu\text{m}$ aggregation observed with 9:1 molar ratios, increasing the lipid–PEG representation in the lipid monolayer gave significantly better PBS stability. As denoted by asterisks (*) in **Figure 2**, we chose formulations with diameters less than 100 nm for further characterization.

The end result of investigating the lipid/polymer mass ratio and lipid–PEG/lipid molar ratio formulation parameters was the identification of a minimum requirement for a 15% lipid/polymer mass ratio and 7.5:2.5 lipid/lipid–PEG molar ratio to form sub-100 nm NPs (**Figure 2**). Hence, an optimal NP formulation consists of (i) sufficient total lipid coverage so that the PLGA hydrophobic core is not exposed, and also (ii) sufficient PEG surface density to provide charge screening in PBS (**Figure 3**). With the addition of other types of drugs, higher drug loadings, or functionalized PEG end-groups, it may be necessary to recalibrate the formulation as done in **Figure 2** to derive a new optimal formulation.

PLGA–lipid–PEG NP Polymer Formulation Parameters.

Another parameter we can use to control NP size is polymer inherent viscosity, which corresponds approximately to polymer molecular weight. Using an optimal formulation of 20% total lipid/polymer mass ratio with 7:3 lipid/lipid–PEG molar ratio denoted by an asterisk (*) in **Figure 2**, we varied the PLGA polymer inherent viscosity. The NPs were stable in PBS, had relatively similar polydispersities and showed a gentle decrease in size with increasing polymer inherent viscosity (**Figure 5C**). The effect of polymer inherent viscosity on NP size is consistent with previous reports for PLGA–PEG polymeric NPs¹³. A possible mechanism is that higher molecular weight polymers precipitate to form more compact structures during nanoprecipitation as compared to lower molecular weight polymers. 0.82 dl/g PLGA inherent viscosity was used in all subsequent experiments to form the polymeric core.

The organic phase was studied using organic solvents of increasing dielectric constants that exhibit increasing polarity and water miscibility. We chose four organic solvents, tetrahydrofuran (THF), acetone, acetonitrile and dimethylformamide (DMF), all which have been commonly used to solubilize and formulate NPs, to study the effect of the organic solvent used to solubilize the PLGA polymer¹³. The trend towards larger NPs was observed as the solvent used became less water miscible and the polymer concentration was raised (**Figure 4A**). Interestingly, when very non-polar organic solvents such as THF was used, we obtained extremely low polydispersities around ~0.100, whereas when very polar organic solvents such as DMF was used, polydispersities were higher at ~0.300; acetonitrile and acetone gave polydispersities around ~0.200. The effect of vortexing for 3 min after nanoprecipitation should not only disperse random lipid micelles but also disperse the solvent droplets. Presumably, the PLGA/THF droplets showed inefficient solvent dispersion and in a more predictable fashion than PLGA/DMF droplets, giving differences in polydispersities and sizes observed. Subsequently, we used acetonitrile as a model organic solvent, as it is a good solvent for Dtx1. Acetone, however, was used in **Chapters 6 and 7** to precipitate smaller NPs.

It is possible to vary polymer concentrations to control the size and zeta potential of NPs. As polymer concentrations were increased from 1 to 25 mg/mL in acetonitrile (with a corresponding scale-up of lipid in the aqueous phase), we observed the trend of increasing NP size from 65 to 160 nm along with an increase in zeta potential from -40 mV to -70 mV in water

(values are much closer to ± 0 mV in buffer due to charge screening) (**Figure 4A**). Finally, we tested the effect of varying solvent/water ratios on the size and zeta potential of NPs. When our typical solvent/water ratio of 0.33 was modified from 0.1 to 1, we observed NP sizes to be almost constant at ~ 65 nm with a slight trend of size increase. However, when the solvent/water ratio was increased to 5 and 10, NP sizes increased to 88.1 ± 0.4 nm and 105.3 ± 2.2 nm, respectively (**Figure 4B**). The solvent/water ratio is typically kept at 1 or less to bias the system towards drug encapsulation and NP self-assembly. At solvent/water ratios of greater than 1, the efficiency of NP self-assembly and drug loading yield may be reduced.

In Vitro Controlled Drug Release Kinetics of PLGA–lipid–PEG NPs.

We next wanted to understand how the three functionally different layers of our PLGA–lipid–PEG NPs controlled the release of Dtx1; namely, the total lipids present at the interface, the length of the PLGA polymer in the core, and the PEG surface density (**Figure 5A**). This experiment was performed in H₂O instead of PBS buffer solution as we took into consideration that some formulations were not optimized for stability in PBS. This experiment characterizes fundamental properties of the NPs as opposed to simulating a physiological environment.

An inset in **Figures 5A–C** shows the diameters and zeta potentials of the NPs in H₂O. When we changed total lipid/polymer mass ratio on three log scales from 0.1% to 100% (wt/wt), we observed different *in vitro* drug release rates. Drug release rates for 0% lipid compared to 100% lipid differed as much as 20 h for 50% release (**Figure 5A**).

In a separate experiment, we changed the PLGA polymer length in the core. Previously, PLGA polymeric NPs with longer PLGA chains were shown to release drugs more slowly than NPs with shorter polymer chains¹³. Our study shows a small contribution of polymer inherent viscosity in controlled drug release, but the dominant contribution in these core-shell NPs come from the lipid monolayer density (**Figure 5B**).

Likewise, in an experiment to examine the contribution of PEG surface density to drug release, the PEG surface density was changed from 0% to 40% (mol/mol) with the total number of lipid and lipid–PEG molecules kept constant. Drug release was also observed to be relatively similar (**Figure 5C**).

Next, we examined the drug encapsulation efficiency, loading and release profile of the hybrid NPs in comparison with PLGA-PEG NPs and PLGA NPs. We hypothesized that the addition of a lipid monolayer at the interface of the PLGA core and the PEG shell may serve two distinct functions: (i) to prevent small drug molecules from freely diffusing out of the PLGA core, thereby improving drug encapsulation efficiency and loading yield, and (ii) to reduce water penetration rate into the PLGA core, thereby decreasing the rate of polymer hydrolysis and drug release from the NPs. As shown in **Figure 6A**, when Dtxl was mixed with PLGA (5 wt%) and dissolved in acetonitrile for the preparation of lipid-polymer hybrid NPs, $59 \pm 4\%$ (mean \pm SD, n=3) of Dtxl was encapsulated. In contrast, Dtxl encapsulation efficiencies of PLGA-PEG NPs and PLGA NPs were approximately $19 \pm 3\%$ (mean \pm SD, n=3) and $37 \pm 4\%$ (mean \pm SD, n=3), respectively. The lower encapsulation efficiencies of PLGA-PEG NPs may stem from the possibility that some PEG blocks are buried inside the PLGA-PEG NP cores during nanoprecipitation, giving a less hydrophobic core compared to PLGA cores of hybrid NPs and PLGA NPs.

The encapsulated Dtxl was released from the hybrid NPs at a sustained rate over 120 h (**Figure 6B**). When hybrid NPs, PLGA-PEG NPs and PLGA NPs were loaded with Dtxl at approximately 3 wt%, it took the hybrid NPs around 20 h to release 50% of Dtxl versus 10 h and 7 h for PLGA-PEG NPs and PLGA NPs, respectively. The results indicate that the lipid core-shell interface acts as a molecular fence that slows down drug release from the NP core. Next, we observed that the high Dtxl encapsulation efficiency and sustained release is retained across a range of drug loadings. For example, when the initial Dtxl input was 5, 10 and 15 wt% of the PLGA polymer, the measured drug loading yield reached 3.0, 6.1 and 8.5 wt% respectively, which corresponded to a nearly constant encapsulation efficiency of 60%. Dtxl encapsulation efficiency dropped when the initial drug input was increased to 20 wt% (**Figure 6C**). We also found that Dtxl was released from the hybrid NPs in a sustained manner until its loading yield was higher than ~6 wt% (**Figure 6D**).

In Vitro Stability of PLGA–lipid–PEG NPs.

NP stability in serum is an important criterion for utility as drug carriers *in vivo*. Using the change in NP size in the presence of plasma as a surrogate for protein adsorption and biofouling, we next studied the serum stability of lipid-polymer hybrid NPs. We incubated NPs with 10 wt% BSA and 10 vol% human plasma solution and monitored changes in NP size over time. PLGA-PEG NPs and PLGA NPs were tested in parallel as controls. From **Figures 7A-B**, the hybrid NPs and PLGA-PEG NPs were stable in 10% BSA solutions, retaining their size of 90 ± 2 nm (polydispersity = 0.223 ± 0.011 , mean \pm SD, n=3), while a slight increase in size was observed in 10% plasma solution. In contrast, PLGA NPs showed a dramatic size increase from 90 to 200-300 nm within 10 min of incubation in BSA or plasma. Hence, we observed that the presence of PEG prevented protein adsorption on the NP surface, which is consistent with previous reports that a decrease in NP biofouling can prolong NP systemic circulation half-life¹⁴.

Next, we performed assays of long-term *in vitro* stability and protein binding on a formulation of 20% total lipid/PLGA mass ratio, 7:3 lipid/lipid–PEG molar ratio, and 0.82 dl/g PLGA polymer inherent viscosity core. PBS stability assays for long-term stability were carried out where the NPs were dialyzed in PBS over 120 h at 37 °C and withdrawn at 24 h intervals. DLS sizing measurements demonstrate that the NPs remain stable over five days with no significant change in size and polydispersities (**Figure 7C**). This result suggests that the DSPE–PEG density on the NPs does not drop below the range of full electrostatic and steric stabilization over the course of 120 h. It could be that the DSPE–PEG covalent bond in PEGylated lipid molecules is very stable and the PEG group is not hydrolyzed off, or that the lipid monolayer does not peel off over 120 h. Thus, the NPs prepared in this study should remain stable *in vitro* for relatively long periods. Plasma stability assays for protein binding were performed in which NPs were incubated in 10 vol% human plasma solution (diluted in PBS) or 100% fetal bovine serum (FBS) for 120 h at 37 °C. After an initial ~20 nm increase in size, the NPs maintained size stability throughout the 120 h study (**Figure 7C**), suggesting that plasma protein binding was not a significant factor. This result suggests that the current formulation has sufficient stability derived from steric repulsion by the PEG chain, electrostatic repulsion from the negatively charged carboxylic end group and adequate lecithin coverage of the polymeric core.

The mechanism of drug release from a polymeric core is typically bulk or surface erosion, or in some cases a combination of both. These *in vitro* stability assays also suggest a mechanism of drug release from the PLGA–lipid–PEG NPs. Surface erosion of particles results in a gradual decrease in NP mean diameter over 120 h, while bulk erosion of particles results in constant NP mean diameters over 120 h. Our data shows almost constant mean diameters with no gradual mean diameter reduction over time (**Figure 7C**). We postulate that the mechanism of drug release from PLGA–lipid–PEG NPs occurs by bulk erosion, in which Dtx1 diffuses out through channels that form within the NP core before bulk degradation, as opposed to gradual surface erosion from the PEG shell.

Post-formulation Purification and Storage of PLGA–lipid–PEG NPs.

NPs made by nanoprecipitation contain 10-15 vol% organic solvent which fail to evaporate during the self-assembly stage. Post-formulation purification of the NPs is necessary to remove trace amounts of organic solvent contamination which causes NP instability and degradation. We analyzed the diameter, polydispersity and zeta potential of our NPs after purification by either dialysis or ultrafiltration with a commercially available centrifuge filtration device. We found there to be no observed difference using either methods, even after multiple washing steps using the ultrafiltration method (**Figure 8A**). The two purification methods can be used together to achieve gentle organic solvent removal and to change NP concentrations or buffer solutions. Potential pharmaceutical use of these NPs requires scalable processes for the storage of larger batches of NPs. We encapsulated Dtx1 in the NPs (5 wt%), freeze-dried the NP solution in liquid nitrogen and lyophilized the NPs at -80 °C. The addition of cryoprotectants such as 10% (wt/vol) sucrose allowed for recovery of 87.0 ± 0.6 nm NPs, similar to the original 64.5 ± 0.5 nm diameters. In the absence of 10% sucrose, NPs aggregated significantly to ~ 2.1 μm (**Figure 8B**).

Scalability of PLGA–lipid–PEG NPs.

As a first attempt to demonstrate the potential scalability of this process, we synthesized 300 mg (polymer weight) batches of NPs. The NPs maintained the biological and physicochemical properties as previously described. Currently, we have made reproducible ~1 g batches of sub-100 nm drug-encapsulated NPs and these are described in **Chapter 7**. It is vital that the concentration and total volume of the reaction be optimized carefully because NP size increases with polymer concentration (**Figure 4A**). Large volumes may suffer from inadequate mixing and stirring during the self-assembly stage, resulting in a polydisperse batch of micron-sized particles. More seriously, inadequate mixing results in the improper encapsulation of hydrophobic drugs that are unprotected in aqueous environments. These drugs will subsequently precipitate out in physiological buffers. Our ~1 g batches in **Chapter 7** allow us to dissolve very hydrophobic drugs to high concentrations in physiological buffers and release these drugs with well-defined kinetics *in vitro*. In an academic setting, our scalability is now only limited by equipment at our disposal (large centrifuges and magnetic stirring plates) rather than feasibility, reproducibility and manpower. It is likely that in an industrial setting, equipment would be more accessible, removing the current limitations of scale-up.

In Vitro Cytotoxicity of PLGA–lipid–PEG NPs.

HeLa and HepG2 cell lines were used to assess the cellular cytotoxicity of the NPs. Cytotoxic activity was evaluated at twofold dilutions in triplicate ranging from 25 mg/mL to 0.1 mg/mL. Following 24 h exposure to the NPs, cell viability was assessed by the MTT assay. The results were plotted onto a fitted curve and expressed as treatment over control (T/C) values for cell survival. The NPs did not cause significant cytotoxicity against either cell line. Experimental TC_{50} values of the NPs grown on HeLa cells were found to be 5.55 mg/mL for HeLa cells (**Figure 9A**) and 4.58 mg/mL for HepG2 cells (**Figure 9B**). Representative photographs of HeLa and HepG2 cells are shown with no NPs added (left column), incubated with NPs at TC_{50} values (middle column), and incubated with NPs at TC_{100} values (right column) (**Figure 9C**).

PLGA–Lipid–PEG Microparticle Synthesis by the Homogenization Emulsion Technique.

Finally, to develop a spectrum of hybrid particles that are either relatively small (sub-100 nm) or large (1-2 μm) defined in terms of systemic delivery, we synthesized PLGA–lipid–PEG hybrid microparticles (MPs) with similar properties to PLGA–lipid–PEG NPs. The MPs were made by the homogenization emulsion technique using ethyl acetate, but other solvents such as dichloromethane (DCM) and chloroform are also possible. Particle size was confirmed by DLS to be 950 ± 23.5 nm (polydispersity= 0.253 ± 0.022 , $n=3$). Representative images of the MPs with a field emission scanning electron microscope (SEM) showed that the use of DSPE–PEG2000–COOH (**Figure 10A, 10B**) or DSPE–PEG3400–COOH (**Figure 10C, 10D**) resulted in monodisperse hybrid MPs with spherical morphology. The MP batches shown in **Figure 10** have not undergone any size fractionation. In **Figure 11**, we analyzed the diameters of representative MPs from **Figure 10A**. Generally, the sizes of the MPs are approximately 1-2 μm , and their minimum to maximum sizes range from 0.6 to 2.6 μm .

MPs made by the emulsion technique typically require surfactants such as 0.1% to 1% polyvinyl alcohol (PVA) in the aqueous phase to stabilize the emulsions and prevent coalescence¹⁵. Here, surfactants are not required aside from DSPE–PEG2000 or DSPE–PEG3400 lipid–polymer conjugates. The elimination of PVA surfactants which may not be completely washed away during purification steps results in the synthesis of highly biocompatible MPs.

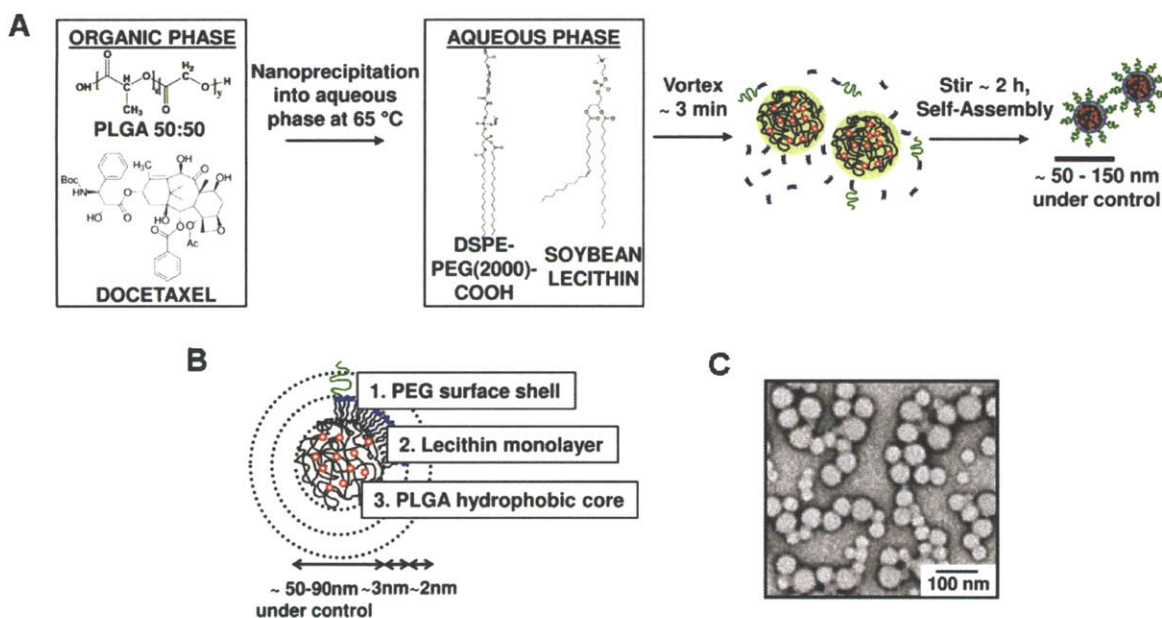


Figure 1. Synthesis of PLGA–lipid–PEG core–shell NPs.

(A) The illustration shows the synthesis of PLGA–lipid–PEG NPs by a modified nanoprecipitation method and self-assembly. (B) NPs are comprised of a hydrophobic PLGA core, a hydrophilic PEG shell, and a lecithin monolayer at the interface of the hydrophobic core and the hydrophilic shell. (C) A TEM image shows the core–shell structures of the NPs. NPs were negatively stained with uranyl acetate to enhance the electron contrast between polymers and lipids.

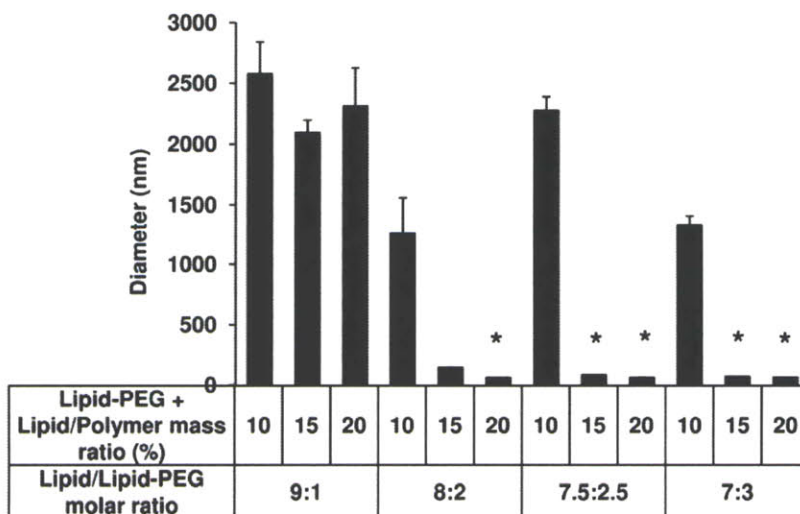


Figure 2. Lipid/lipid–PEG to polymer ratios.

By varying the parameters of total lipid/polymer mass ratio and lipid/lipid–PEG molar ratio, we can tune NP size in physiological buffers. The asterisk (*) refers to optimal NP formulations (mean \pm SD, n=3).

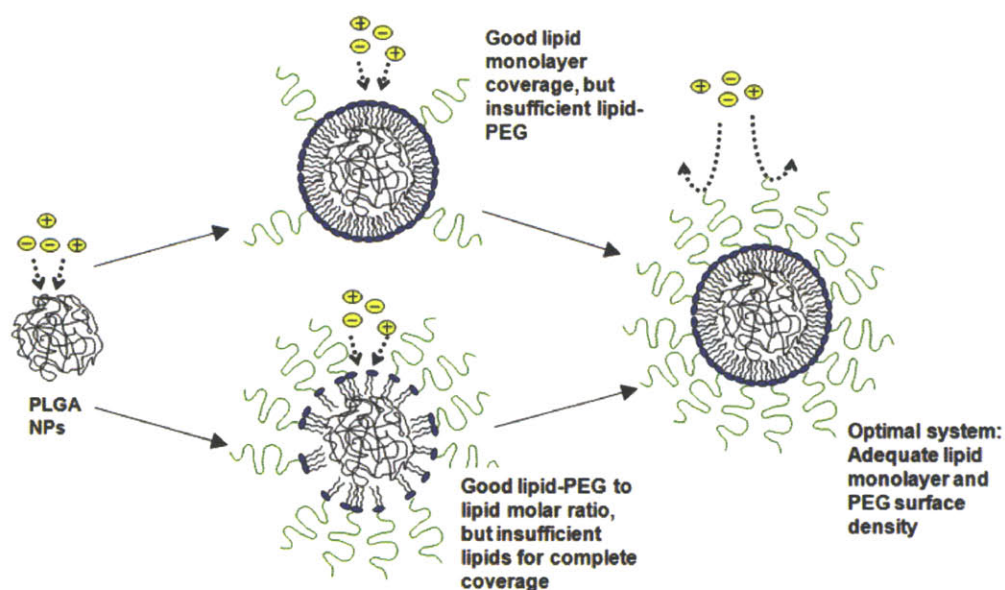


Figure 3. Requirements for an optimal PLGA–lipid–PEG system.

Optimal formulations result from an adequate lipid monolayer and PEG surface density surrounding the hydrophobic PLGA polymeric core. The NPs are stabilized by the PEG layer which provides a steric barrier and a net repulsive force during collision events with other NPs. The reduction in strength of the Coulomb interaction is referred to as the screening of electrical charges on the surface of NPs and results in a sterically stabilized dispersion. Without PEG screening, hydrophobic PLGA NPs decrease the surface area (and electrostatic interactions) in contact with other NPs by aggregation, resulting in MP formation. Two requirements for PEG charge screening are (i) adequate lipid monolayer coverage of the PLGA polymeric core, and (ii) adequate lipid–PEG to lipid ratio (i.e. overall adequate lipid–PEG).

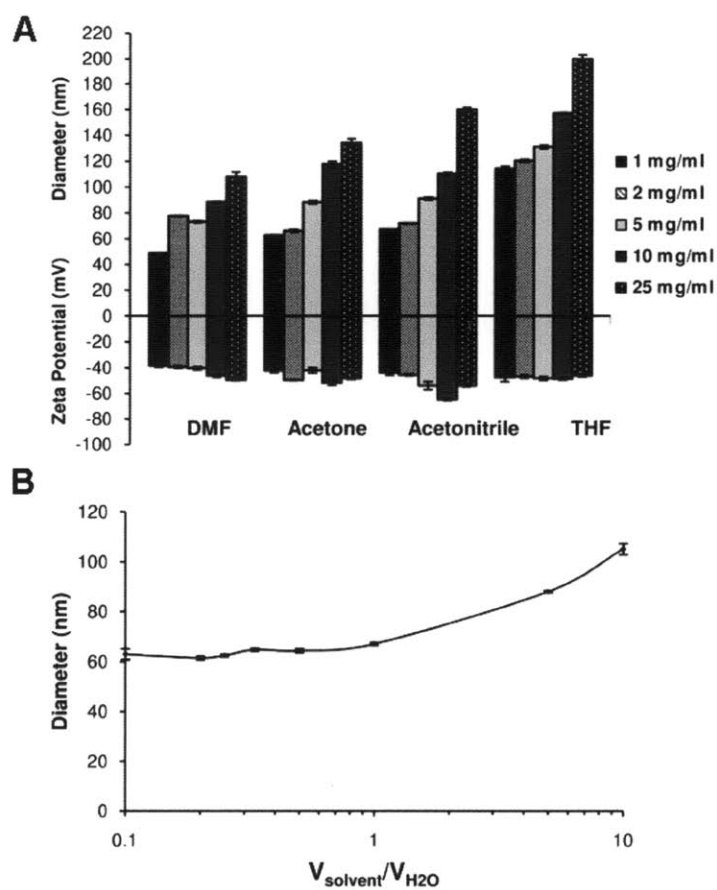


Figure 4. The effect of formulation parameters on the size and zeta potential of PLGA-lipid-PEG NPs.

(A) The effect of polymer concentration on NP size and zeta potential in various organic solvents with different water miscibilities. (B) The effect of solvent/water ratio on NP size, taking acetonitrile as the organic solvent. All results are mean \pm SD, n=3.

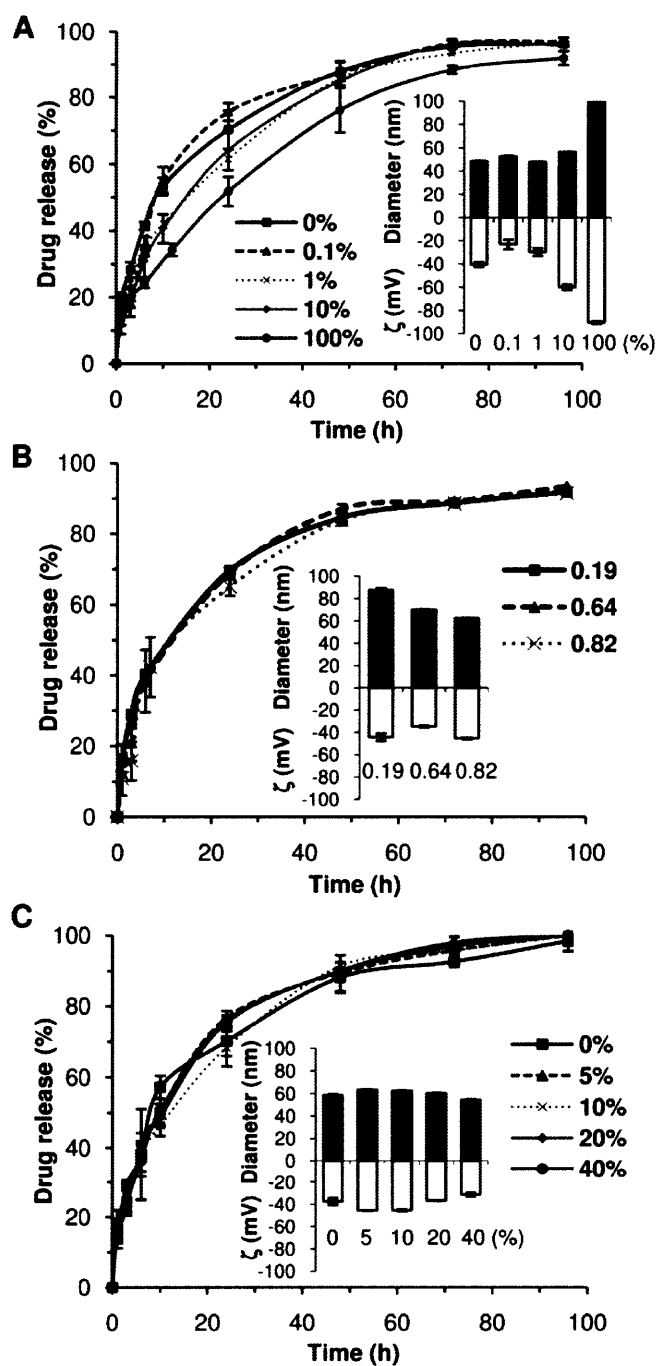


Figure 5. Controlled and sustained drug release profiles of PLGA–lipid–PEG NPs. (A) The effect of total lipid/polymer weight ratio on drug release from the NPs. Inset: percentage units indicate total lipid/PLGA mass ratio. (B) The effect of PLGA inherent viscosity on drug release. Inset: units are in dl/g. (C) The effect of lipid–PEG/lipid molar ratio on drug release. Inset: percentage units indicate lipid–PEG/lipid molar ratio. The inset of each panel shows the diameter and zeta potential (denoted as ζ) of corresponding NP formulations. All results are mean \pm SD, n=3.

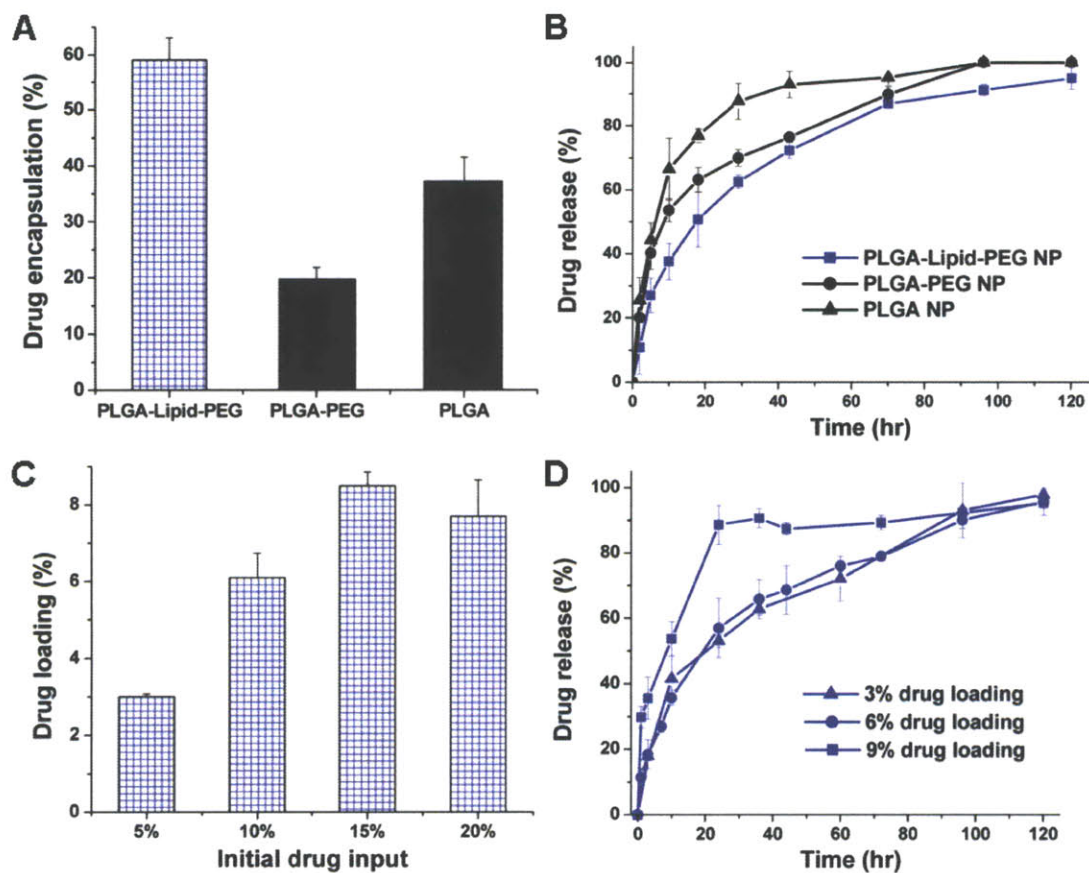


Figure 6. Drug loading capacity and release profile of PLGA–lipid–PEG hybrid NPs versus PLGA–PEG and PLGA polymeric NPs.

(A) Drug encapsulation efficiency of Dtx1 in PLGA–lipid–PEG NPs versus PLGA–PEG NPs and PLGA NPs. The initial drug input was 5 wt% of PLGA polymer weight for each type of NP. (B) Drug release profiles from PLGA–lipid–PEG NPs, PLGA–PEG NPs and PLGA NPs. Drug loading was ~3 wt% for each type of NP. (C) Drug loading of PLGA–lipid–PEG NPs at various initial drug inputs based on PLGA polymer weight. (D) Drug release profiles from PLGA–lipid–PEG NPs with 3, 6 and 9 wt% drug loading. All results are mean \pm SD, n=3.

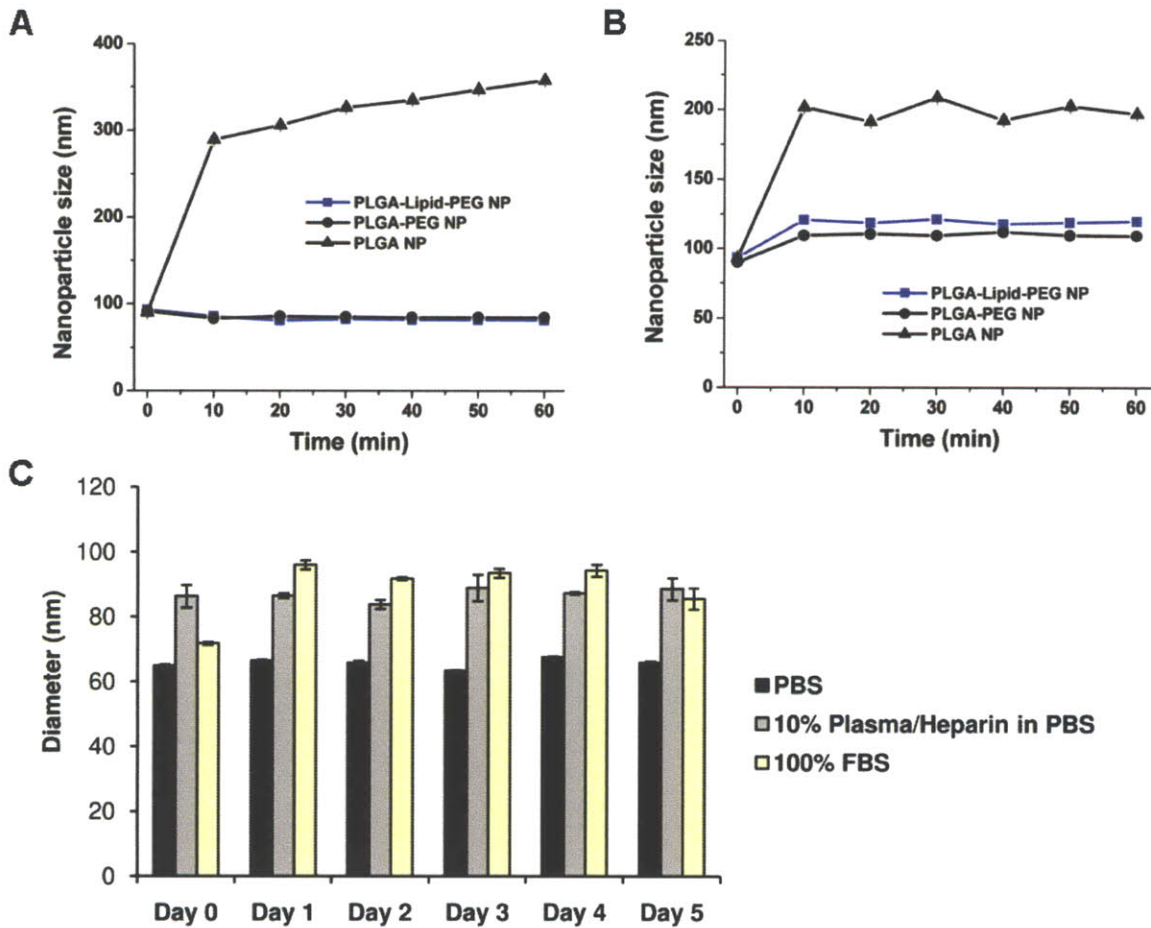


Figure 7. NP temporal stability in vitro.

PLGA-lipid-PEG NPs (blue squares), PLGA-PEG NPs (black circles), and PLGA NPs (black triangles) were incubated in a (A) 10 wt% BSA solution, and (B) 10 vol% plasma with heparin solution at 37 °C under gentle stirring. (C) *In vitro* stability of PLGA-lipid-PEG NPs over 120 h. NPs were incubated with PBS, 10 vol% plasma/heparin in PBS and 100% FBS for five days at 37 °C. At each time point, an aliquot was taken for DLS size measurements. All results are mean \pm SD, n=3.

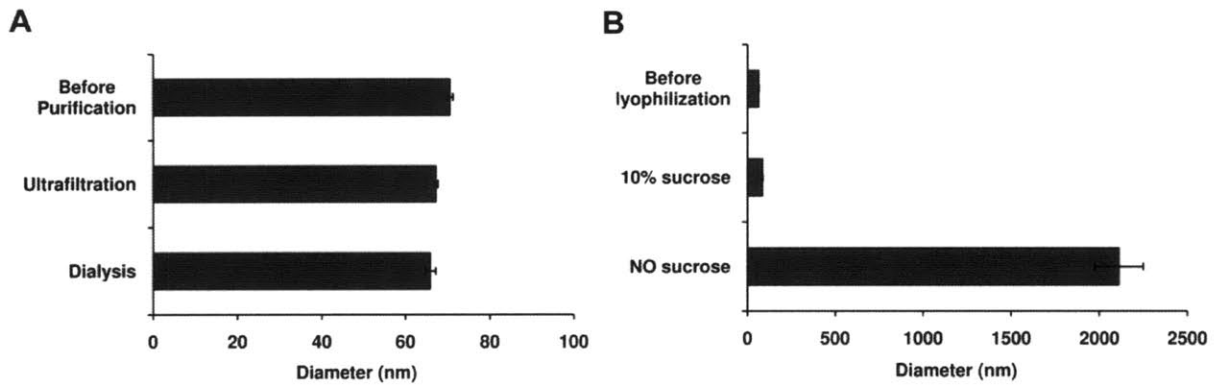


Figure 8. Post-formulation stability of PLGA–lipid–PEG NPs.

(A) Post-formulation stability of the NPs upon purification by ultrafiltration or dialysis. (B) Post-formulation stability of the NPs upon liquid nitrogen freeze-drying and lyophilization with 10% sucrose cryoprotectant. All results are mean \pm SD, n=3.

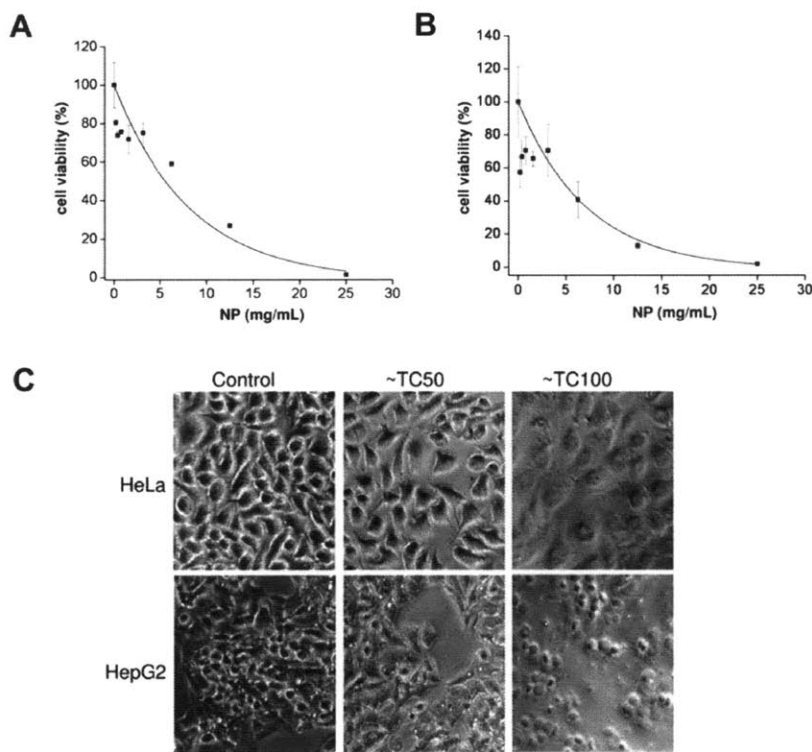


Figure 9. Cytotoxicity of PLGA–lipid–PEG NPs on HeLa and HepG2 cell lines.

Fitted curves show cell viability of (A) HeLa and (B) HepG2 cell lines with twofold dilutions of NPs from 25 to 0.1 mg/mL. All results are mean \pm SD, n=3. (C) Photographs of control HeLa and HepG2 cells without NP incubation (left column); HeLa and HepG2 cells at TC₅₀ concentrations of NPs (middle column); HeLa and HepG2 cells with the highest concentration (25 mg/mL) of NPs (right column).

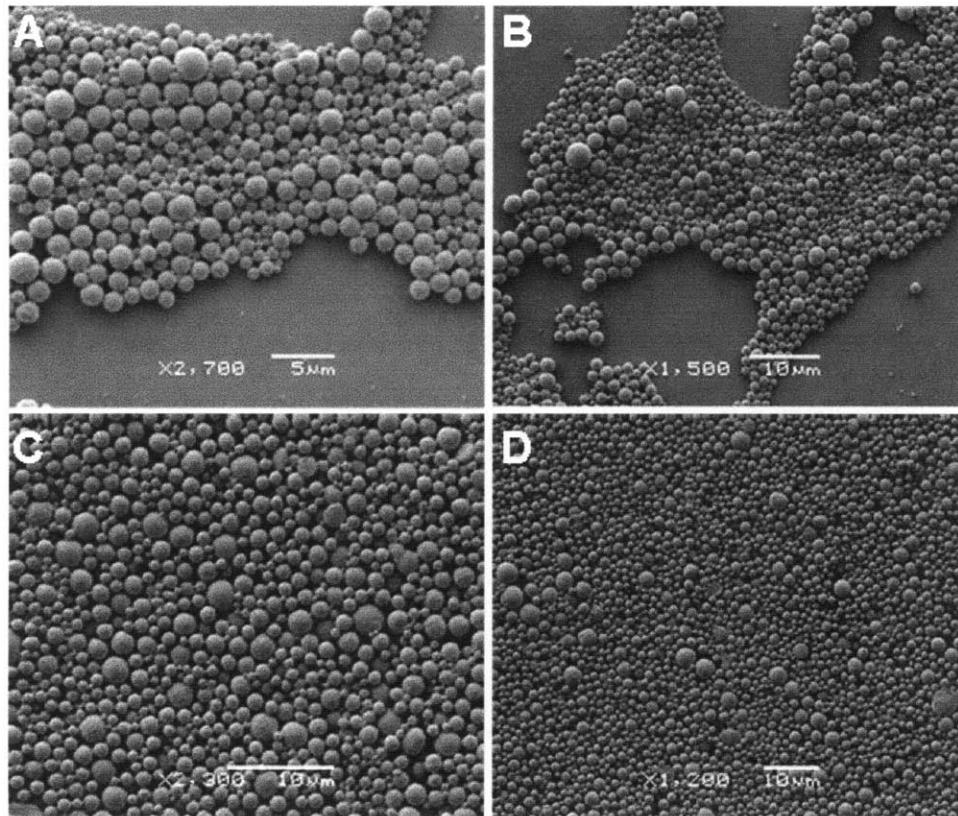


Figure 10. SEM images of PLGA-lipid-PEG MPs.

Scanning electron microscopy (SEM) images of the MPs. The MPs shown here have not been size-fractionated prior to imaging. (A) PLGA-lipid-PEG2000 MPs at 2,700x magnification. Scale bar, 5 μm. (B) PLGA-lipid-PEG2000 MPs at 1,500 x magnification. Scale bar, 10 μm. (C) PLGA-lipid-PEG3400 MPs at 2,300x magnification. Scale bar, 10 μm. (D) PLGA-lipid-PEG3400 MPs at 1,200x magnification. Scale bar, 10 μm.

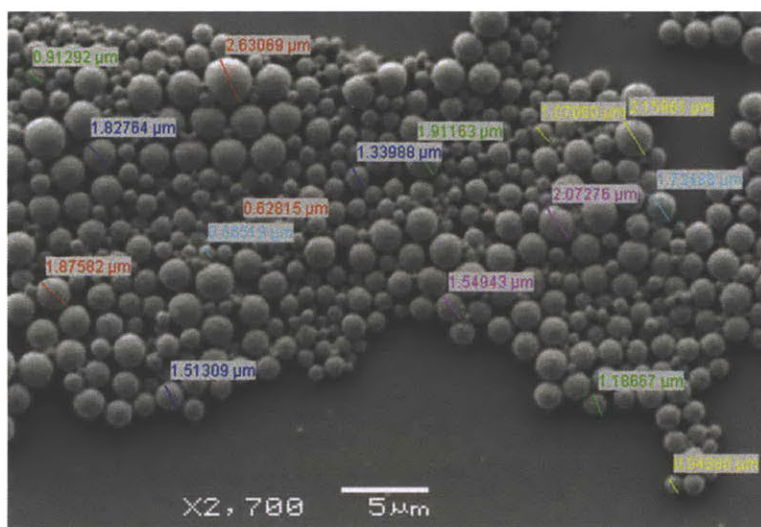


Figure 11. Representative diameters of PLGA–lipid–PEG MPs.

Scanning electron microscopy (SEM) images of PLGA–lipid–PEG2000 MPs at 2,700x magnification. Scale bar, 5 µm. Annotations on representative MPs show that the diameters of MPs range from ~1-2 µm with lower and upper limits at approximately 0.6 µm and 2.6 µm respectively. The MPs shown here have not undergone size-fractionation prior to imaging.

Discussion

In this study, we used ester-terminated poly(_{D,L}-lactic-*co*-glycolic acid) (PLGA) as a model hydrophobic polymer to form the polymeric core of the NPs; polyethylene glycol (PEG) covalently conjugated to 1,2-distearoyl-*sn*-glycero-3-phosphoethanolamine (DSPE) as a model hydrophilic polymer to form the ‘stealth’ shell of the NPs; and lecithin as a model lipid to form the lipid monolayer at the interface of the PLGA core and PEG shell. Both PLGA and PEG polymers have been approved by the FDA for medical applications. Lecithin is a natural lipid extract from soybean and is Generally Regarded as Safe (GRAS). Compared with synthetic alternatives, soybean phosphatidylcholine (sPC) can be totally biodegraded and metabolized since it is an integral part of biological membranes. Hence, these three materials are regarded as well tolerated for potential pharmaceutical applications. We expect the hybrid NPs to be a biocompatible, biodegradable and safe drug carrier for potential clinical use.

The hybrid NPs show improved drug encapsulation and release profiles when compared to PLGA-PEG and PLGA systems. We have shown in **Figures 5A-C** that the lipid monolayer contributes to the consistently higher drug encapsulation efficiency and slower release observed. Based on these experimental results, we propose a model where the lipid monolayer acts as a molecular fence – it promotes drug retention in the hydrophobic polymeric core and restricts water access into the core to slow down PLGA polymer erosion and drug release. Furthermore, in the range of polymeric inherent viscosities and PEG surface densities tested, we were unable to observe any changes in drug release when lipid monolayer coverage was kept constant (**Figure 5B and C**). Therefore, the lipid monolayer may be a limiting factor for drug release and can be manipulated to alter drug release rates. However, it is also important that the overall lipid concentration not be increased beyond the critical micellar concentration (CMC) of lecithin (~0.4 mg/mL, data from manufacturer) or DSPE-PEG (1.1×10^{-5} M or ~0.33 mg/mL)¹⁶ which may result in the assembly of lecithin liposomes (typical sizes are about 100-1000 nm) and ~10-15 nm DSPE-PEG micelles. The coexistence of these liposomes would enhance the overall measured size of the hybrid NPs. Conversely, when the lipid/polymer weight ratio is too low, there is a paucity of lipids and DSPE-PEG to shield the PLGA core, resulting in a lack of stability in physiological conditions.

For targeted delivery, the wide variety of available DSPE-PEG end-groups means that surface functionalization of hybrid NPs with targeting molecules can be easily achieved. In this study, we used DSPE-PEG2000-COOH which can be easily conjugated to amine-terminated targeting ligands such as peptides, small molecules and aptamers by coupling agents such as 1-ethyl-3-(3-dimethylaminopropyl)carbodiimide hydrochloride and N-hydroxysuccinimide (EDC/NHS) (**Chapter 3**). In later chapters (**Chapters 4, 6 and 7**), we switch to using DSPE-PEG2000 with maleimide terminal end-groups for thiomaleimide conjugation to cysteine-containing peptide ligands. This type of covalent conjugation can be completed within 30 min to 2 h and does not need the conjugation chemicals required by carbodiimide chemistry. The disadvantage is that thiomaleimide chemistry is more suitable for ligands that expose only one cysteine group for site-specific conjugation and which do not contain internal sulfhydryl bonds that are required for conformational activity, since conjugation of the wrong cysteine or reduction of sulfhydryl bonds may inadvertently denature the ligand. Finally, the commercial

availability of DSPE–PEG2000–biotin makes conjugation reactions based on the biotin–avidin interaction also possible.

Increasingly, DSPE–PEG conjugates have been used to design micelles with hydrophobic cores surrounded by lipid layers. Mixed micelles of egg PC/DSPE–PEG^{16,17} and mAb-targeted DSPE–PEG micelles¹⁸ have been the focus of the Vladimir Torchilin group. In the lab of Darrell Irvine, hybrid NPs and MPs with PLGA polymeric cores and lipid–PEG shells have been designed using the sonication emulsion technique¹⁹. DSPE–PEG has been used to encapsulate hydrophobic CdSe quantum dots for imaging²⁰, and one study used these DSPE–PEG functionalized dots to observe *Xenopus* embryogenesis *in vivo*²¹. In particular, our hybrid NP design has already been applied to design similar hybrid NPs²². In short, other researchers have similarly explored the use of liposome-like NPs with hydrophobic cores for parenteral delivery of imaging agents and therapeutic payloads.

Although the focus of this project is on systemic uses of sub-100 nm NPs, we have designed similar particles in the low micron range. Unlike typical preparations of PLGA MPs, our MPs do not require the use of chemical surfactants such as PVA²³. The uses of these MPs may range from intramuscular or subcutaneous depots that elute over weeks and months for the delivery of anesthetic or contraceptive drugs. For systemic delivery, hybrid MPs may be used as viral and cancer vaccines since their 1 μm size range make them suitable candidates for phagocytosis. The MPs may be used to present adjuvants and pathogen-associated molecular patterns (PAMPs) such as lipopolysaccharide, double-stranded RNA and unmethylated CpG motifs for recognition by cells of the innate immune system.

In summary, we developed a lipid-polymer hybrid NP platform consisting of a hydrophobic polymeric core, a hydrophilic polymeric shell and a lipid monolayer at the interface of the core and shell. The hybrid NPs have tunable size and surface charge, high drug loading yield, sustained drug release profile and favorable stability in physiological conditions. The NPs were well tolerated by human cell lines and prepared by a potentially scalable nanoprecipitation process. Thus, these hybrid NPs may be suitable as a potential drug delivery system. In **Chapter 3**, we further characterize the *in vivo* pharmacokinetic and pharmacodynamic properties of these NPs.

References

1. Torchilin, V.P. Recent advances with liposomes as pharmaceutical carriers. *Nat Rev Drug Discov* **4**, 145-160 (2005).
2. Zhang, L., *et al.* Nanoparticles in medicine: therapeutic applications and developments. *Clin Pharmacol Ther* **83**, 761-769 (2008).
3. Northfelt, D.W., *et al.* Pegylated-liposomal doxorubicin versus doxorubicin, bleomycin, and vincristine in the treatment of AIDS-related Kaposi's sarcoma: results of a randomized phase III clinical trial. *J Clin Oncol* **16**, 2445-2451 (1998).
4. Moghimi, S.M. & Szebeni, J. Stealth liposomes and long circulating nanoparticles: critical issues in pharmacokinetics, opsonization and protein-binding properties. *Prog Lipid Res* **42**, 463-478 (2003).
5. Soppimath, K.S., Aminabhavi, T.M., Kulkarni, A.R. & Rudzinski, W.E. Biodegradable polymeric nanoparticles as drug delivery devices. *J Control Release* **70**, 1-20 (2001).
6. Kim, T.Y., *et al.* Phase I and pharmacokinetic study of Genexol-PM, a cremophor-free, polymeric micelle-formulated paclitaxel, in patients with advanced malignancies. *Clin Cancer Res* **10**, 3708-3716 (2004).
7. Kim, D.W., *et al.* Multicenter phase II trial of Genexol-PM, a novel Cremophor-free, polymeric micelle formulation of paclitaxel, with cisplatin in patients with advanced non-small-cell lung cancer. *Ann Oncol* **18**, 2009-2014 (2007).
8. Lee, K.S., *et al.* Multicenter phase II trial of Genexol-PM, a Cremophor-free, polymeric micelle formulation of paclitaxel, in patients with metastatic breast cancer. *Breast Cancer Res Treat* **108**, 241-250 (2008).
9. Thevenot, J., Troutier, A.L., David, L., Delair, T. & Ladaviere, C. Steric stabilization of lipid/polymer particle assemblies by poly(ethylene glycol)-lipids. *Biomacromolecules* **8**, 3651-3660 (2007).
10. Wong, H.L., *et al.* A new polymer-lipid hybrid nanoparticle system increases cytotoxicity of doxorubicin against multidrug-resistant human breast cancer cells. *Pharm Res* **23**, 1574-1585 (2006).
11. Wong, H.L., Rauth, A.M., Bendayan, R. & Wu, X.Y. In vivo evaluation of a new polymer-lipid hybrid nanoparticle (PLN) formulation of doxorubicin in a murine solid tumor model. *Eur J Pharm Biopharm* **65**, 300-308 (2007).
12. Sengupta, S., *et al.* Temporal targeting of tumour cells and neovasculature with a nanoscale delivery system. *Nature* **436**, 568-572 (2005).
13. Cheng, J., *et al.* Formulation of functionalized PLGA-PEG nanoparticles for in vivo targeted drug delivery. *Biomaterials* **28**, 869-876 (2007).
14. Gref, R., *et al.* Biodegradable long-circulating polymeric nanospheres. *Science* **263**, 1600-1603 (1994).
15. Wischke, C. & Schwendeman, S.P. Principles of encapsulating hydrophobic drugs in PLA/PLGA microparticles. *Int J Pharm* **364**, 298-327 (2008).
16. Lukyanov, A.N., Gao, Z. & Torchilin, V.P. Micelles from polyethylene glycol/phosphatidylethanolamine conjugates for tumor drug delivery. *J Control Release* **91**, 97-102 (2003).
17. Gao, Z., Lukyanov, A.N., Chakilam, A.R. & Torchilin, V.P. PEG-PE/phosphatidylcholine mixed immunomicelles specifically deliver encapsulated taxol to

- tumor cells of different origin and promote their efficient killing. *J Drug Target* **11**, 87-92 (2003).
18. Torchilin, V.P., Lukyanov, A.N., Gao, Z. & Papahadjopoulos-Sternberg, B. Immunomicelles: targeted pharmaceutical carriers for poorly soluble drugs. *Proc Natl Acad Sci U S A* **100**, 6039-6044 (2003).
 19. Bershteyn, A., *et al.* Polymer-supported lipid shells, onions, and flowers. *Soft Matter* **4**, 1787-1791 (2008).
 20. Park, J.H., von Maltzahn, G., Ruoslahti, E., Bhatia, S.N. & Sailor, M.J. Micellar hybrid nanoparticles for simultaneous magnetofluorescent imaging and drug delivery. *Angew Chem Int Ed Engl* **47**, 7284-7288 (2008).
 21. Dubertret, B., *et al.* In vivo imaging of quantum dots encapsulated in phospholipid micelles. *Science* **298**, 1759-1762 (2002).
 22. Liu, Y., Li, K., Pan, J., Liu, B. & Feng, S.S. Folic acid conjugated nanoparticles of mixed lipid monolayer shell and biodegradable polymer core for targeted delivery of Docetaxel. *Biomaterials* **31**, 330-338.
 23. Jain, R.A. The manufacturing techniques of various drug loaded biodegradable poly(lactide-co-glycolide) (PLGA) devices. *Biomaterials* **21**, 2475-2490 (2000).

Chapter 3. Pharmacokinetic-Pharmacodynamic Studies of Hybrid Lipid-Polymeric Nanoparticles.

Abstract

This study analyzes the pharmacokinetic-pharmacodynamic (PK-PD) profile of hybrid lipid-polymeric NPs for the systemic delivery of therapeutic drugs. To understand their PK profile, the plasma circulation half-life of hybrid NPs was compared against PLGA-PEG NPs by radioisotope-tracking of tritium-labeled PLGA polymers (^3H -PLGA) in the NP core. Radiolabeled NPs delivered by intravenous injection showed circulation half-lives of approximately 3 h and 12 h for PLGA-PEG NPs and hybrid NPs, respectively (n=6). Our earliest targeting studies were initiated using RNA aptamers to study the PD profile of hybrid NPs. A10 RNA aptamers recognize the extracellular domain of the prostate-specific membrane antigen (PSMA), a well characterized membrane glycoprotein expressed on LNCaP prostate epithelial cells. The hybrid NPs were self-assembled from DSPE-PEG-A10 RNA aptamer triblock polymers. *In vitro* fluorescence microscopy studies showed greater uptake of fluorescent dye-encapsulated aptamer-NPs by PSMA-expressing LNCaP prostate adenocarcinoma cell lines versus non-expressing PC3 cell lines. For *in vivo* biodistribution studies, radiolabeled aptamer-NPs were delivered by intravenous injection in mouse xenograft models of prostate cancer. The addition of aptamers altered the distribution of hybrid NPs as a function of aptamer surface density, with 5% and 10% aptamer surface coverage to PEG end-groups giving the best tumor localization. Hence, the use of targeting ligands may improve hybrid NP localization to prostate tumors but require extensive optimization for systemic delivery.

The content of this chapter has been published in whole or in part in the following journal article:

Zhang, L., Chan, J.M., Gu, F.X., Rhee, J.W., Wang, A.Z., Radovic-Moreno, A.F., Alexis, F., Langer, R. Farokhzad, O.C. Self-assembled lipid-polymer hybrid nanoparticles: a robust drug delivery platform. *ACS Nano* (2008). **2**, 1696-1702. Reproduced with permission from ACS Nano. American Chemical Society © 2008.

Introduction

In the design of biocompatible NPs for therapeutic drug delivery, a desired feature includes NPs which have long-circulating plasma half-lives. There are several reasons why long-circulating or ‘macrophage-evading’ NPs are desired¹. An important and direct reason is to provide a reservoir in the blood compartment from which the drug can be released in a continuous and controlled manner – above the therapeutic levels required for efficacy and below toxic levels that cause harmful side-effects. Considering that the encapsulated drugs and therapeutic agents themselves may have short elimination half-lives (e.g. proteins, hydrophobic drugs, siRNA and plasmids), long-circulating NPs may help to slow down the clearance kinetics of the system and present a pharmacologically-desired free drug profile. Furthermore, one would expect that because of prolonged residence in the blood, long-circulating NPs with the appropriate sub-100 nm size range also have a better chance of reaching target sites such as solid tumors and atherosclerotic plaques, giving improved imaging diagnosis or treatment efficacy.

To study the *in vivo* pharmacokinetic (PK) properties of a new NP formulation, plasma half-life can be calculated by measuring its concentration in the blood or serum of animals over time based on a one-component model, which assumes a rapid equilibration in drug concentrations throughout the body. The calculated half-life helps to estimate the length of time the NPs stay in circulation and this is useful in deciding dosing frequencies for dose-response studies. Here, we derived the circulation half-life profile of hybrid NPs and PLGA–PEG NPs from tracking radioisotope levels in animals over time using tritium-labeled poly(lactic-*co*-glycolic acid) (³H–PLGA) polymers encapsulated in the NP core. Blood samples were collected at indicated time points and subject to scintillation counting to quantify remaining radioisotope levels in the blood.

Next, to study the PD profile of the NPs, we functionalized the hybrid NPs with A10 2'-fluoropyrimidine RNA aptamer (Apt) ligands against the PSMA antigen upregulated in metastatic prostate adenocarcinomas. We synthesized triblock lipid–PEG–Apt conjugates which were then used to self-assemble the NPs. For *in vitro* cellular uptake studies, Dtx1–NP–Apts (10% aptamer surface coverage to PEG end-groups) showed preferential uptake by PSMA-positive LNCaP cell lines over PSMA-negative PC3 cell lines. For *in vivo* biodistribution

studies, we delivered radiolabeled Dtx1–NP–Apts in mouse LNCaP xenograft models of prostate cancer and show that the addition of aptamers alter NP distribution as a function of aptamer surface density. Inadequate aptamer surface coverage (~1%) and over-coverage (25%, 50% and 100%) resulted in poor localization to prostate xenografts compared to optimal aptamer surface coverage at 5% and 10%. Taken together, this suggests that while *in vitro* cellular uptake of NPs may be improved from aptamer functionalization, the direct relationship of aptamer functionalization and cell uptake may not correspond *in vivo*. When systemically delivered, the aptamer surface coverage on these NPs needs to be carefully optimized to achieve maximal tumor uptake.

Hence, these PK-PD studies provide invaluable information before this hybrid NP system can be used in medical applications. They form the rationale for the intended therapeutic dose, dose-frequency and for the design of dose-ranging efficacy studies described in **Chapter 7**. Finally, these studies allow for the formulation of hypotheses regarding the contribution of targeting ligands to NP localization *in vivo*.

Methods

Materials.

BD Matrigel matrix phenol-red free was bought from BD Biosciences (San Jose, CA). 2.5% avertin was made from 100% avertin added dropwise with constant stirring into PBS at 37 °C. 100% avertin was made from 10 g of 2,2,2-tribromoethanol (99%) mixed with 10 mL of tertiary amyl alcohol (Sigma). Custom synthesized ³H–PLGA, Solvable tissue solubilizer and Hionic-Fluor scintillation cocktail were purchased from Perkin-Elmer (Waltham, MA). 0.5 M EDTA, pH 8.0 and NBD-cholesterol (22-(*N*-(7-nitrobenz-2-oxa-1,3-diazol-4-yl)amino)-23,24-bisnor-5-cholesterol-3 β -ol) were both from Invitrogen (Carlsbad, CA). 1-ethyl-3-(3-dimethylaminopropyl) carbodiimide (EDC) and sulfo-N-hydroxysuccinimide (Sulfo-NHS) were both from Pierce Thermo Scientific (Rockford, IL).

Animals.

Animal care and experimental procedures were performed in accordance with the regulations of the Massachusetts Institute of Technology Division of Comparative Medicine and the Principles of Laboratory Animal Care of the National Institutes of Health. ~300-400 g male and female Sprague-Dawley rats were purchased from Charles River Laboratories (Wilmington, MA) for pharmacokinetic studies. Male, 8-week-old, BALB/c scid mice were purchased from Jackson Laboratory (Bar Harbor, ME) for xenograft and pharmacodynamic studies.

In vivo Circulation Half-Life Studies.

³H-PLGA encapsulated NP samples were intravenously (i.v.) injected into Sprague-Dawley rats (n=6) at t=0 h. ~100 uL of blood was drawn from alternate saphenous leg veins at the indicated time points. For each procedure, animals were restrained for less than 5 min using a Decapicone restrainer (Braintree Scientific, Braintree, MA). Samples were immediately added into previously-weighed scintillation vials containing 100 uL of 0.5 M EDTA, pH 8.0. Blood samples were weighed. 400 µL of Solvable solubilizer was added to dissolve the sample and 200 µL of 30% H₂O₂ was added for 1 h at 60 °C to decolorize the sample. After cooling, Hionic-Fluor scintillation cocktail was added to the maximum height of the 7-mL vial. ³H levels were counted using a Packard TriCarb Scintillation Analyzer (Downers Grove, IL). Data is presented as percent injected dose per organ or per gram of tissue.

Lipid-PEG-Aptamer Triblock Synthesis.

A10 aptamer sequence (28 kDa): 5'-NH₂-spacer GGG/AGG/ACG/AUG/CGG/AUC/AGC/CAU/GUU/UAC/GUC/ACU/CCU/UGU/CAA/UCC/UCA/UCG/GCIT-3'. Aptamers were custom synthesized with 2' fluoropyrimidines, a 5'-amino group attached by a hexaethyleneglycol spacer and a 3'-inverted T cap by Integrated DNA Technologies (IDT, Leuven, Belgium). Aptamers were stored as a lyophilized powder at -80°C and resuspended in DNase- and RNase-free water (Invitrogen). Lipid-PEG-COOH molecules were activated for 15 min with a 1/10 molar ratio to EDC/Sulfo-NHS. Aptamers were activated at 90 °C for 3 min and snap cooled on ice. Lipid-PEG-COOH and aptamers were mixed at a 10/1 ratio and incubated

for 4 h at RT with gentle shaking. Samples were dialyzed using a 5 kDa MWCO Slide-a-Lyzer cassette for 5 h (Pierce Thermo Scientific) with water changes to remove unconjugated lipid-PEG-COOH molecules. Absorbance spectroscopy at 280 nm was used to quantify lipid-PEG-aptamer triblock molecules based on the assumption that retained aptamers are conjugated to lipid-PEG. The same procedure was used to synthesize lipid-PEG-random oligonucleotides for *in vivo* biodistribution studies. NPs were filter-sterilized before i.v. injection into animals.

Cellular Uptake Studies by Fluorescence Microscopy.

To visualize the NPs, NBD-cholesterol was encapsulated in the NPs. The fluorescence emission spectrum of NBD (ex/em=460 nm/534 nm) was detected in the green channel (490 nm/528 nm) of a Delta Vision RT deconvolution microscope. Prostate LNCaP and PC3 cell lines were grown in 8-well microscope chamber slides in RPMI-1640 and Ham's F-12K medium, respectively, both supplemented with 100 units/mL aqueous penicillin G, 100 µg/mL streptomycin and 10% FBS (fetal bovine serum). The cells were plated at concentrations that allow for 70% confluence in 24 h (i.e., 40 000 cells/cm²). On the day of experiments, the cells were washed with prewarmed PBS buffer and incubated with prewarmed fresh media for 30 min before adding NPs with a final concentration of ~250 µg/mL (n=4). After a 2 h incubation at 37 °C, the wells were washed two times with PBS (300 µL per well), fixed with 4% formaldehyde and mounted with Vectashield nonfluorescent mounting medium containing DAPI (Vector Laboratory, Burlingame, CA). The cells were then imaged using a Delta Vision RT deconvolution microscope.

LNCaP Xenograft Mouse Model.

LNCaP cells were cultured as described in the *Cellular Uptake Studies* section. Cells were grown to 90% confluency, counted and resuspended to give 15 million cells/mL in complete growth media with 1x penicillin/streptomycin and 10% FBS for fast-growing tumors. The mice were weighed and anesthetized intraperitoneally with 2.5% avertin (200 mg/kg body weight). The same volume of Matrigel was added to LNCaP suspensions for a 1/1 media/Matrigel volume ratio. 3 x 10⁶ LNCaP cells in 200 µL media/Matrigel mixture suspensions were subcutaneously

injected into the left flank of each mouse. The LNCaP tumors were allowed to develop for ~3 weeks. Tumor length and width was measured by digital calipers using the formula: $(\text{width}^2 \times \text{length})/2$. When the tumors were sufficiently large (~250-300 mm³), the mice were divided randomly into groups (n=5) and NPs were prepared for administration.

In vivo Biodistribution Studies.

³H-PLGA NP formulations were resuspended in 200 μL PBS before administration. The mice were anesthetized and dosed with NPs via retro-orbital injection. After dosing, animals were sacrificed at 24 h. 200 μL of blood was drawn by cardiac puncture while the tumor, heart, lungs, liver, spleen and kidneys were harvested from each animal. All samples, including blood samples, were weighed in scintillation vials that were pre-weighed prior to sample collection. Due to the size of the liver, it had to be homogenized and only ~100 mg of tissue was analyzed. Each organ was solubilized with 2 mL of Solvable for ~12 h at 60 °C. 200 μL of 0.5 M EDTA was added to each vial, followed by 200 μL of 30% H₂O₂. Blood samples were prepared as discussed in the method for *Circulation half-Life Studies*. Samples were incubated for 1 h at 60 °C to decolorize the samples. After samples were cooled, scintillation cocktail was added to the maximum height of the 7-mL vial. ³H levels were counted using a Packard TriCarb Scintillation Analyzer (Downers Grove, IL). To determine the 100% dose, injected formulations were counted as well. Data is presented as percent injected dose per organ or per gram of tissue.

Results

In Vivo Circulation Half-Life of PLGA–lipid–PEG NPs.

To measure the duration of the hybrid NPs in blood plasma, we conducted PK circulation half-life studies comparing radioisotope-encapsulated PLGA–lipid–PEG NPs against PLGA–PEG NPs. Samples were intravenously injected into Sprague-Dawley rats at t=0 h and blood was drawn from alternate saphenous leg veins at indicated time points. The blood samples were processed and circulatory ³H levels were analyzed by liquid scintillation counting, with counts adjusted for blood weight. Average reads per time point were plotted against time as a percentage of ³H readings taken immediately after injection at t=0 h. The circulation half-life of PLGA–lipid–PEG NPs and PLGA–PEG NPs were found to be ~12 h and ~3 h respectively (mean ± SD, n=6) (**Figure 1**).

Aptamer Targeted–NP Synthesis.

The suitability of the hybrid NPs for targeted drug delivery applications was analyzed *in vitro* and *in vivo* using A10 aptamers as a model ligand. The A10 aptamer is a nuclease-stabilized 2'-fluoropyrimidine RNA molecule with 57 base pairs, and it has shown high binding affinity to the extracellular domain of the prostate specific membrane antigen (PSMA) overexpressed by late-stage and metastatic prostate cancer². Amine-terminated aptamers were covalently conjugated to carboxyl-functionalized lipid–PEG conjugates using EDC/sulfo-NHS activation chemistry, followed by dialysis to remove unconjugated lipid–PEG molecules.

The lipid–PEG–Apt conjugates were used in the nanoprecipitation and self-assembly of NPs as illustrated in **Figure 2**. After self-assembly, the NPs were washed using ultracentrifugation as described previously. To characterize and quantify aptamer surface coverage, lipid–PEG–Apt conjugates were added at various amounts (from 0 µg to 240 µg aptamer weight) to the 4% ethanol aqueous phase, replacing unconjugated lipid–PEG–COOH molecules until an excess of lipid–PEG–Apt was added. The NPs were incubated at pH 11 for 30 min to hydrolyze ester linkages in the aptamers. Samples were spun down using Pall Microsep centrifuge devices (10 kDa MWCO) to collect the hydrolyzed nucleotides in the flow-through

(**Figure 3A**). RNA concentrations were measured to estimate 0-100% lipid-PEG-Apt surface coverage of hybrid NPs. In **Figure 3B**, the amount of aptamers added (as lipid-PEG-Apt conjugates) on the X-axis is shown against the amount present after self-assembly and washing steps on the Y-axis. As the curve starts to plateau at 240 μg lipid-PEG-aptamer addition, $\sim 20 \mu\text{g}$ lipid-PEG-Apt coverage was considered to represent 100% NP surface coverage. Subsequently, $\sim 240 \mu\text{g}$ lipid-PEG-Apt/1 mg of NP was added to give 100% surface coverage. It is not surprising that the triblock incorporation efficiency of aptamers is approximately 8-10%, since the large size and hydrophilic nature of aptamers affect the amphiphilic balance of the lipid-PEG molecules. If small molecule ligands such as folate and peptides are used, the triblock incorporation efficiency is expected to be much higher.

Cellular Uptake Studies.

The uptake of A10 aptamer-targeted NPs by different cell lines was analyzed *in vitro*. LNCaP prostate adenocarcinomas which express the PSMA antigen on their plasma membrane were chosen as the target cell line and PC3 prostate adenocarcinomas which do not express the PSMA antigen were used as negative controls. To visualize cell uptake of the NPs using fluorescence microscopy, a hydrophobic fluorescent probe, NBD cholesterol (ex/em=460 nm/534 nm), was encapsulated in the hybrid NPs. In **Figure 4**, the PSMA-targeted hybrid NPs at 10% aptamer surface coverage to PEG end-groups were taken up by LNCaP cells (PSMA positive) (**Figure 4A**) but not by PC3 cells (PSMA-negative) (**Figure 4C**). The small amount of NBD signal from PC3 cells may represent a portion of free NBD dye released from NPs during incubation or alternatively may represent nonspecific uptake of particles by the PC3 cells. When the PSMA aptamer was not used, negligible amounts of non-targeted NPs were delivered to LNCaP (**Figure 4B**) and PC3 (**Figure 4D**) cells.

In Vivo Biodistribution of PLGA–lipid–PEG NPs.

For *in vivo* pharmacodynamics studies, NPs were formulated with both radioisotopes and therapeutic payloads in the polymeric core. ^3H -PLGA (100 $\mu\text{Ci}/1\text{ mg}$ PLGA) was added to the PLGA/acetonitrile solution for radiolabel detection, while 100 μg Dtx1 (10 wt% initial load) was added to form a therapeutically relevant NP formulation.

Tumor xenografts were induced by subcutaneous injections of LNCaP prostate adenocarcinomas onto the left flanks of mice. When tumors were sufficiently large at $\sim 250\text{-}300\text{ mm}^3$, the mice were randomly divided into groups ($n=5$) and NPs were prepared for PK studies. Sample NP groups with 0%, 1%, 5%, 10%, 25%, 50% and 100% aptamer surface coverage, as well as 10% random oligonucleotide surface coverage, were delivered by i.v. injection into xenografted mice. The mice were sacrificed after 24 h for blood draw by cardiac puncture and to harvest their vital organs. After the samples were weighed, circulatory and organ ^3H levels were analyzed by liquid scintillation and adjusted for blood and organ weights. Average ^3H readings were taken as a percentage of the injected dose per organ (**Figure 5**). From **Figure 5**, most of the NP can be found in the liver, blood and kidneys at 24 h, which is an expected profile observed from previous studies with PLGA–PEG polymeric NPs³.

From the observation of ^3H readings taken as a percentage of the injected dose per weight of tumor tissue, different amounts of aptamer coverage can change the tumor distribution profile of NPs (**Figure 6**). At 5% and 10% aptamer surface coverage, NPs localize more to the xenograft compared to inadequate 1% aptamer coverage. When too much of the NP surface is covered by aptamers (25%, 50% and 100%), an increased localization effect is not observed. The NPs may be cleared more quickly by the reticulo-endothelial system (RES) of the liver and spleen because (i) the high levels of double-stranded RNAs on NP surfaces may act as pathogen-associated molecular patterns (PAMPs) that are recognized by cells of the innate system; or (ii) the higher surface density of aptamers may hinder the shielding function of the PEG layer leading to greater clearance. Hence, for targeting ligands to improve NP localization to sites of interest such as prostate tumors, formulations need to be carefully optimized for systemic delivery.

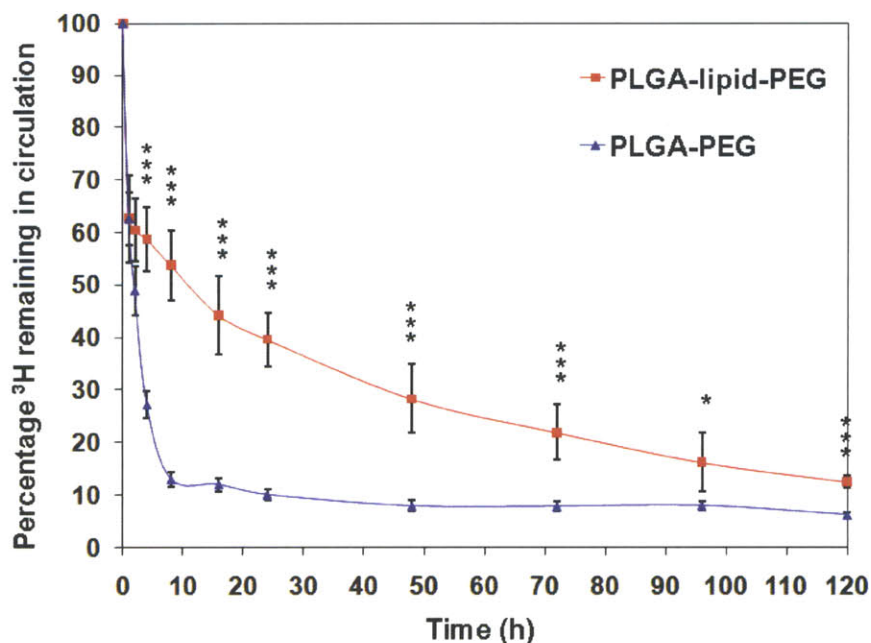


Figure 1. Circulation half-life of PLGA–lipid–PEG and PLGA–*b*–PEG NPs.

Samples were i.v. injected into Sprague-Dawley rats at t=0 h and blood was drawn from alternate saphenous leg veins at the indicated time points. Circulatory ^3H levels were analyzed by liquid scintillation and counts were adjusted for blood weight. Average reads per time point were plotted against time as a percentage of ^3H readings taken immediately after injection at t=0 h. The circulation half-life of PLGA–lipid–PEG and PLGA–*b*–PEG NPs are ~12 h and ~3 h respectively (mean \pm SD, n=6, 3 male/3 female per group). *, P < 0.05; ***, P < 0.001, by one-way ANOVA with Tukey post hoc test.

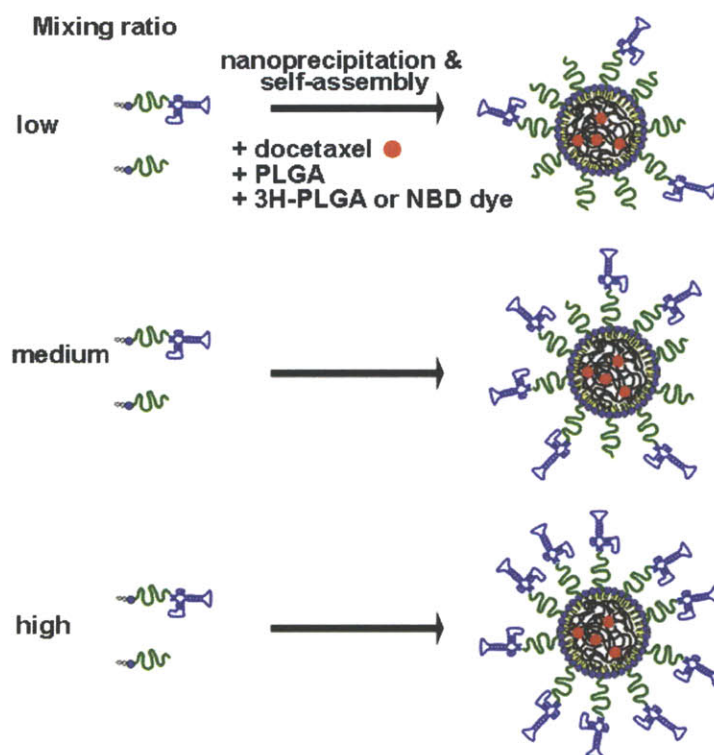


Figure 2. Hybrid NPs with varying aptamer surface densities.

Aptamer surface density can be directly controlled by using different ratios (0%, 1%, 5%, 10%, 25%, 50% and 100%) of lipid-PEG-aptamer conjugates. The NPs were visualized by fluorescence microscopy using NBD-cholesterol or quantified by scintillation counting using radioisotope labeled ^3H -PLGA polymers.

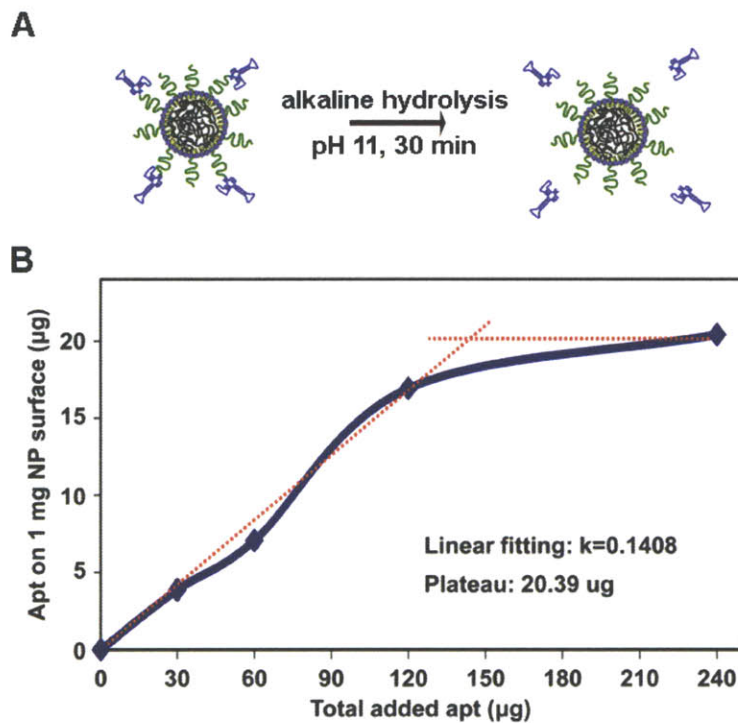


Figure 3. Calibration of A10 aptamer surface coverage on hybrid NPs.

(A) Alkaline hydrolysis (pH 11) of the RNA aptamers. (B) The amount of aptamers added (as lipid-PEG-Apt conjugates) is measured against the amount of aptamers that remain on the NPs after self-assembly and purification. The maximum aptamer surface coverage is approximately 20 µg aptamers/mg of hybrid NPs, achieved by the addition of 240 µg of aptamers/mg of hybrid NPs.

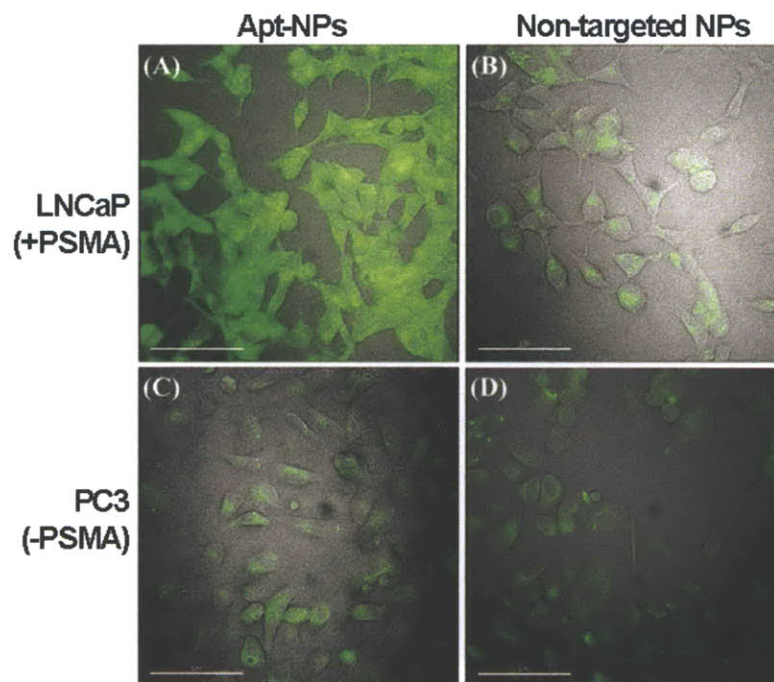


Figure 4. Cellular uptake of hybrid NPs surface-modified with the A10 RNA aptamer. The A10 aptamer binds to the extracellular domain of the prostate specific membrane antigen (PSMA) overexpressed in prostate epithelial cancer cell lines. For imaging, NBD-cholesterol dyes (green) were encapsulated inside the NPs. Fluorescence microscopy images show that aptamer-targeted NPs were delivered to (A) LNCaP cells which overexpress the PSMA protein but not (C) PC3 cells which do not express PSMA protein. Non-targeted NPs did not preferentially bind to either (B) LNCaP (+PSMA) cells or (D) PC3 (-PSMA) cells. Scale bar, 100 μm .

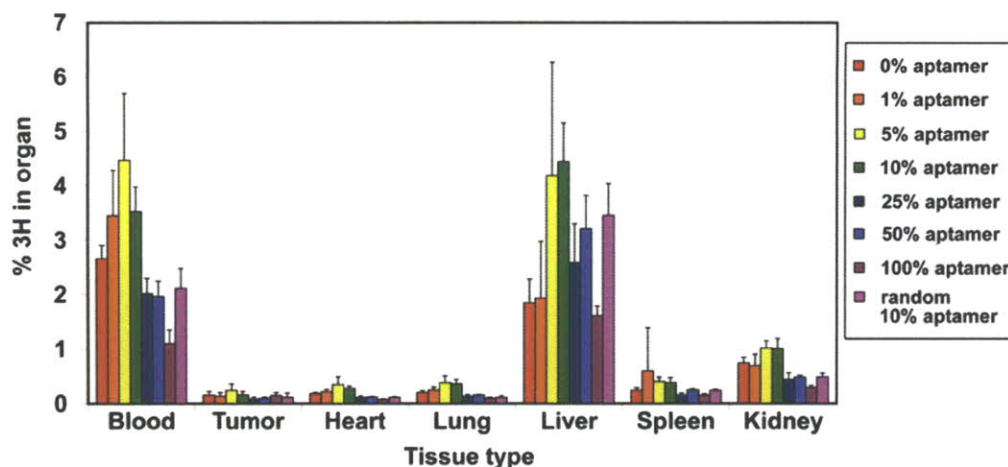


Figure 5. Average ³H readings taken as a percentage of injected dose per organ. ³H-PLGA biodistribution at 24 h after injection. % aptamer refers to the surface-coverage of lipid-PEG-aptamers on NPs. Results are expressed as mean ± SD, n=5 per group.

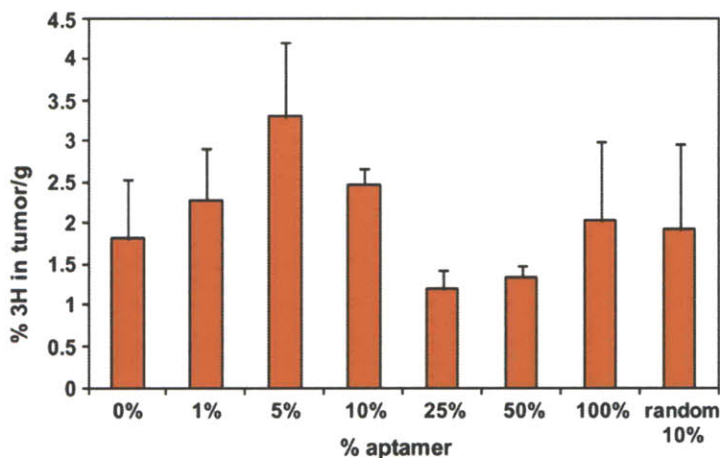


Figure 6. Average ³H readings in tumors taken as a percentage of injected dose per gram of tumor tissue.

³H-PLGA biodistribution at 24 h after injection in tumor tissue. % aptamer refers to the surface-coverage of lipid-PEG-aptamers on NPs. Results are expressed as mean ± SD, n=5 per group.

Discussion

A major objective underlying these *in vivo* PK assessments is to show that the NPs exhibit dose-independent and time-independent PK, or that the NP clearance and volume of distribution is constant across doses and over time. In this PK study, the *in vivo* circulation half-lives of PLGA–lipid–PEG NPs and PLGA–*b*–PEG NPs were found to be ~12 h and ~3 h respectively. Other reports also point to the same conclusion. Previous studies with PLGA–PEG diblock NPs and Genexol-PM gave circulation half-life values of ~4.5 h^{4,5}. On the other hand, stealth liposomes (PEG-coated liposomes) have an average circulation half-life of ~3 days (76 h) in patients⁶, similarly reported for Doxil (55 h, reports vary)^{7,8}. Hence, this suggests that the liposome-like shell on hybrid NPs may significantly contribute to their extended *in vivo* circulation half-life.

The second objective of these studies is to extrapolate the PK data for both dose and dosing frequency selection in dose-ranging studies. However, the dosing frequency derived from PK data may either overestimate or underestimate the concentration needed for PD responses. For example, if the PK data shows that there is insufficient NP in circulation after several days, there may still be sufficient NP deposition in tissues to help with PD responses. On the other hand, the PK data may indicate there is sufficient NP in the blood circulation, but the NPs may be bound strongly to plasma proteins (50% of which are serum albumins) and exhibit lower volumes of distribution. Hence, the plasma and BSA temporal stability studies described in **Chapter 2** were necessary to show that the hybrid NPs were not overwhelmingly bound by albumin.

Even if the NPs are not albumin bound, simply enhancing NP plasma half-life may not necessarily lead to an increase in therapeutic effect. In experimental tumors, the movement of drugs and particulates into the extravascular compartment of tumors was shown to be limited by high interstitial pressures, partly due to a lack of functional lymphatic drainage coupled with lower intravascular pressure⁹. Interstitial pressure tends to be higher at the center of solid tumors, creating a mass flow movement of fluid to the periphery⁹. Despite these potential barriers to delivery, long-circulating NPs may have a more tolerable safety profile in terms of systemic

cytotoxicity compared to the unencapsulated drugs. They have been shown to reduce dosing frequency, improve drug biodistribution and allow more drugs to reach the tumor site¹.

As a step towards improving the PD profile of hybrid NPs, they were conjugated with aptamers against the PSMA antigen upregulated in prostate tumors. Lipid-PEG-Apt triblock conjugates were synthesized by carbodiimide chemistry and used to self-assemble hybrid NPs. It is expected that the hybrid NP system may need to be functionalized with different types of ligands. In **Chapter 2**, a variety of conjugation chemistries based on the different terminal end-groups on DSPE-PEG was discussed. Here, a detailed account is given of the standard three methods of assembling the ligand-bearing DSPE-PEG molecules into NPs. Considering that similarities can be drawn between the surfaces of hybrid NPs and PEG-coated liposomes, existing methods used to functionalize the end-groups of PEGylated liposomes can be extrapolated for the hybrid NPs.

In the first method, the hybrid NPs can be preformed, washed to remove free lipid-PEG molecules and then conjugated to the desired ligand. This method was used for studies described in **Chapter 6**. While this is a straightforward method that requires lower amounts of conjugation ligands, the conformational cloud of PEG chains may interfere with the reaction between the reactive PEG end-group and ligand, and this strategy may lead to NPs bearing some surface unreacted groups which may need to be quenched. Furthermore, the chemicals used for conjugation may disrupt NP structures. Another strategy is based on the formation of lipid-PEG-ligand conjugates and simple incubation with the preformed NPs. Here, the conjugates exchange with other lipid-PEG molecules forming the micellar layer and is incorporated into the lipid layer. In the third approach, lipid-PEG-ligand conjugates are preformed and used directly during preparation (**Chapter 3, 4 and 7**). With the last two approaches however, the larger ligand-bearing conjugates may not be incorporated into the micellar layer, instead favoring smaller and more plentiful lipid-PEG molecules. Hence, it is important to quantify ligand incorporation after purification steps regardless which of the three methods is chosen.

A previous report from our laboratory used the third approach to synthesize aptamer-targeted NPs. Preformed PLGA-PEG-Apt triblock copolymers were mixed with PLGA-PEG diblock copolymers in a single-step nanoprecipitation process¹⁰. Our study uses lipid-PEG-Apt triblock copolymers for the nanoprecipitation and self-assembly of hybrid NPs. Likewise, Wu *et*

al. also formed lipid-PEG-DNA aptamer micelles using this triblock strategy¹¹. However, problems arise when generalizing these systems for protein-based ligands such as antibodies or affibodies because proteins cannot tolerate the harsh organic solvents and chemicals for conjugation to PLGA-PEG polymers. The use of lipid-PEG-protein conjugates may likely overcome the problem of solvent incompatibility. One can conjugate protein-based targeting ligands with lipid-PEG in aqueous conditions to form lipid-PEG-ligand triblock polymers before nanoprecipitation. The lipid-PEG-ligand conjugates may also be stored in aqueous buffers for days to weeks, minimizing production time and NP batch-to-batch variation, allowing for larger-scale production of targeted NPs.

In conclusion, this study showed that optimal formulations of surface-functionalized aptamers (5% and 10%) could improve the tumor localization of hybrid NPs up to 2.5-fold over other aptamer-targeted NP groups. Hence, it is important to balance the requirement for improved avidity by displaying more aptamers versus maintaining an exposed PEG shield that helps to keep the NPs in circulation.

In a shift from larger ligands (28 kDa) with fixed three-dimensional conformations, we explored the use of small, linear peptide ligands (~1 kDa) for targeting in **Chapter 4**. Here, triblock lipid-PEG-peptides are used instead of lipid-PEG-aptamers and a previously-characterized peptide was applied to target hybrid NPs to atherosclerotic plaques.

References

1. Moghimi, S.M., Hunter, A.C. & Murray, J.C. Long-circulating and target-specific nanoparticles: theory to practice. *Pharmacol Rev* **53**, 283-318 (2001).
2. Lupold, S.E., Hicke, B.J., Lin, Y. & Coffey, D.S. Identification and characterization of nuclease-stabilized RNA molecules that bind human prostate cancer cells via the prostate-specific membrane antigen. *Cancer Res* **62**, 4029-4033 (2002).
3. Cheng, J., *et al.* Formulation of functionalized PLGA-PEG nanoparticles for in vivo targeted drug delivery. *Biomaterials* **28**, 869-876 (2007).
4. Li, Y., *et al.* PEGylated PLGA nanoparticles as protein carriers: synthesis, preparation and biodistribution in rats. *J Control Release* **71**, 203-211 (2001).
5. Kim, T.Y., *et al.* Phase I and pharmacokinetic study of Genexol-PM, a cremophor-free, polymeric micelle-formulated paclitaxel, in patients with advanced malignancies. *Clin Cancer Res* **10**, 3708-3716 (2004).
6. Harrington, K.J., *et al.* Effective targeting of solid tumors in patients with locally advanced cancers by radiolabeled pegylated liposomes. *Clinical Cancer Research* **7**, 243-254 (2001).
7. Northfelt, D.W., *et al.* Pegylated-liposomal doxorubicin versus doxorubicin, bleomycin, and vincristine in the treatment of AIDS-related Kaposi's sarcoma: results of a randomized phase III clinical trial. *J Clin Oncol* **16**, 2445-2451 (1998).
8. Gottlieb, J.J., Washenik, K., Chachoua, A. & Friedman-Kien, A. Treatment of classic Kaposi's sarcoma with liposomal encapsulated doxorubicin. *Lancet* **350**, 1363-1364 (1997).
9. Jain, R.K. Delivery of molecular and cellular medicine to solid tumors. *Adv Drug Deliv Rev* **46**, 149-168 (2001).
10. Gu, F., *et al.* Precise engineering of targeted nanoparticles by using self-assembled biointegrated block copolymers. *Proc Natl Acad Sci U S A* **105**, 2586-2591 (2008).
11. Wu, Y., Sefah, K., Liu, H., Wang, R. & Tan, W. DNA aptamer-micelle as an efficient detection/delivery vehicle toward cancer cells. *Proc Natl Acad Sci U S A* **107**, 5-10 (2010).

Chapter 4. Fibrin Targeted Nanoparticles for Delivery to Diverse Atherosclerotic Lesion Types in Coronary Artery Disease.

Abstract

Morphologically diverse coronary lesions often co-exist in high-risk individuals, ranging from stenotic lesions with thick fibrous caps, to the more numerous non-stenotic lesions with large lipid cores and thin fibrous caps susceptible to rupture and thrombosis. This mixed clinical manifestation requires multi-pronged management by both revascularization and pharmacotherapy. Our study aims to combine the management of diverse lesion types with peptide-targeted NP drug delivery. Fibrin is a significant component of plaque architecture and is also deposited following basal lamina exposure during percutaneous angioplasty. ~60 nm PLGA–lipid–PEG hybrid NPs were conjugated with anti-fibrin peptide ligands and tested for binding in animal models of early- to mid-stage lesions modeled by apolipoprotein E-knockout mice fed an atherogenic diet. In this model of atherosclerosis, targeted-NPs localized to primary lesions in the aortic arch and brachiocephalic artery branch points. Revascularized stenotic lesions were modeled using balloon-angioplastied rat abdominal aortas and targeted-NPs showed greater binding over control NP groups. These results indicate that targeted nanotechnology against thrombotic elements may potentially be used in the management of coronary artery disease.

Introduction

Atherothrombotic vascular disease (ATVD), the number one cause of mortality in developed countries, is a growing problem due to the worldwide epidemic of obesity and insulin resistance¹. Although oral drugs that lower systemic risk factors have been successful^{2,3}, there is a tremendous treatment gap that leaves up to 70% of the high-risk population at continued risk. The morphology of lesions in human coronary atherosclerosis is staggering, with two extremes from stenotic lesions (thick caps and fibrosis) to thin-cap fibroatheromas (thin caps and a large lipid-rich pool prone to rupture and thrombosis)⁴. Most lesions lie between these two extremes and usually coexist in a given high-risk individual⁵. Hence, optimum management often requires both systemic therapy and revascularization (**Figure 1A**).

A *sine qua non* of the disrupted atherosclerotic plaque is fibrin deposition. The coagulation cascade and fibrin formation plays a crucial role in atherogenesis^{6,7} and fibrin deposition accelerates sharply with the severity of the lesion^{8,9}. Not only does fibrin deposition give one of the earliest signs of plaque rupture or erosion, but along with intraplaque hemorrhage, also forms a considerable part of the core of the growing lesion. A disrupted plaque may be diagnosed by the detection of small deposits of fibrin in erosions or microfractures. Fibrin deposition may also be used to characterize a 'vulnerable' lesion before a high-grade stenosis develops that requires cardiac intervention. Likewise, vascular injury from percutaneous transluminal angioplasty (PCTA) or stent placement in stenotic lesions may result in endothelial denudation, extracellular matrix exposure and activation of the coagulation cascade. The end point of this cascade is fibrin deposition in the lumen of affected vessels which may contribute to subsequent thrombotic events¹⁰.

The peptide ligand CREKA (cys-arg-glu-lys-ala) was identified from an *in vivo* phage screen in a transgenic mouse model of breast cancer as a fibrin-binding ligand¹¹. In a separate study, targeted micelles were shown to accumulate in Apolipoprotein-E knockout (ApoE^{-/-}) mice fed a western diet for 16 weeks, a mouse model of plaques that resemble advanced lesions¹².

This study aims to apply the signature of fibrin deposition to manage diverse lesion types in coronary artery disease (CAD) (**Figure 1A**). We designed CREKA-targeted ~60 nm hybrid NPs^{13,14} with a hydrophobic PLGA polymeric core for sustained drug release and an anti-biofouling PEG shell covalently-conjugated with peptide targeting ligands. In the first study, CREKA-NPs localized to mid-stage aortic lesions in ApoE^{-/-} mice models fed an atherogenic diet for 8 weeks and not to healthy aortas of C57BL/6 mice fed a regular chow diet. In the second study, CREKA-NPs targeted revascularized stenotic lesions in a rat model of angioplasty, where balloon catheter injury mimics angioplasty of pre-existing stenotic lesions in human patients. Together, these results indicate the potential use of CREKA-targeted NPs throughout atherogenesis and following revascularization of stenotic lesions.

Methods

Materials.

Soybean lecithin was purchased from Alfa Aesar (Ward Hill, MA). 1,2-Distearoyl-*sn*-Glycero-3-Phosphoethanolamine-N-[Maleimide (PolyethyleneGlycol) 2000] (DSPE-PEG-Mal) (ammonium salt) was purchased from Avanti Polar Lipids (Alabaster, AL). 50:50 poly(D,L-lactic-co-glycolic acid) (PLGA) polymer, carboxylate end group (inherent viscosity range: 0.15-0.25 dL/g in HFIP) was purchased from Durect Corporation (Cupertino, CA). Alexa Fluor 647 hydrazide tris(triethylammonium) salt was purchased from Invitrogen (Carlsbad, CA). All peptides were custom synthesized and purified by reverse-phase high-performance liquid chromatography (RP-HPLC) to >98% purity by SynBioSci Corporation with mass spectral analysis (Livermore, CA).

Animals.

Animals care and experimental procedures were performed in accordance with the regulations of the Massachusetts Institute of Technology Division of Comparative Medicine and the Principles of Laboratory Animal Care of the National Institutes of Health. Homozygous male ApoE^{-/-} mice

(B6.129P2-*ApoE*^{tm1Unc}/Crl) and male C57BL/6 mice were purchased from Jackson Laboratories (Bar Harbor, Me). Male Sprague-Dawley rats weighing ~400-500 g were obtained from Charles River Laboratories (Wilmington, MA) and fed a normal rodent diet.

Synthesis of Lipid-PEG-Peptide Copolymers.

1 mg peptide (MW=600 Da) was dissolved in 0.1 mL PBS buffer and incubated with Bond-Breaker™ (Tris(2-carboxyethyl)phosphine) (TCEP) (Pierce, Rockford, IL) for disulfide bond reduction at a 10:1 TCEP:peptide molar ratio. The reaction was carried out for 30 min at RT. Reduced peptides were mixed with 2.5 mg DSPE-PEG-Mal (5 mg/mL in PBS buffer) to achieve a 2:1 molar ratio. The mixture was incubated at 4 °C for 24 h and then dialyzed in 3.5 kDa MWCO Spectrapor cassettes (Spectrum Laboratories, Houston, TX) for 24 h with two water changes.

Synthesis of Fluorescent Dye-PLGA Copolymers.

Alexa Fluor 647 (A647) dyes were covalently conjugated to PLGA (viscosity 0.19 dL/g) using EDC/NHS chemistry in DMF. The reaction was continued overnight in the dark at RT with gentle stirring. A647-PLGA conjugates were precipitated in 2/1 ethyl ether/methanol by centrifugation, dried in vacuum, weighed and resuspended in acetonitrile for NP preparation.

Preparation of Peptide-NP Conjugates.

0.09 mg DSPE-PEG-peptide copolymer (1 mg/mL) was mixed with 0.06 mg lecithin (1 mg/mL) in 3 mL of 4% ethanol aqueous solution. 1 mg PLGA-A647 was dissolved in acetonitrile. The DSPE-PEG-peptide/lecithin mixture solution was heated to 65°C for 3 min under gentle stirring. Next, the PLGA solution was added dropwise, vortexed vigorously for 3 min and gently stirred for 2 h. The remaining organic solvent and free molecules were removed by washing the NP solution three times using a 10 kDa MWCO Amicon Ultra-4 centrifugal filter (Millipore, Billerica, MA). NP size (diameter, nm) and surface charge (zeta potential, mV) was evaluated

using a ZetaPALS DLS detector (15 mW laser, incident beam=676 nm; Brookhaven Instruments, Holtsville, NY).

Induction of Early Stage Atherogenesis in ApoE^{-/-} Mice.

8-week old ApoE^{-/-} mice were fed high-fat rodent diet containing 21% pork lard supplemented with 0.15% cholesterol for 8 weeks until they were 16-week old (diet #TD12079B, Research Diets, New Jersey). Control C57BL/6 mice were fed a normal chow diet for 8 weeks.

Ex Vivo ApoE^{-/-} Mouse Aorta Targeting Studies.

16-week old mice were sacrificed for open abdominal cavity surgery *in situ*. After flushing the aorta with Hanks buffer, 0.5 mg of peptide-NP conjugates (1 mg/mL) were delivered by left-ventricle injection and incubated in the aorta for 10 min under constant pressure using silk threads to secure the ascending aorta, aorta branch points and abdominal aorta. After incubation, non-adsorbed NPs were washed away using Hanks buffer. The aortic arch to abdominal aorta was fixed in 4% paraformaldehyde, paraffin-embedded and sectioned. Adjacent H&E stained and unstained sections were cut followed by an 80 µm interval to the next pair of sections. All histology preparations were done by the Koch Institute Histology Core Facility. Slides were imaged using a Delta Vision RT Deconvolution Microscope using the 20x objective (Applied Precision Inc, Issaquah, DC).

Ex Vivo Balloon-Injured Rat Aorta Targeting Studies.

Rats were sacrificed for open abdominal cavity surgery *in situ*. The aorta was flushed with Hanks buffer solution and a Fogarty® arterial embolectomy catheter (Model: 120602F, Edwards Lifesciences, Irvine, CA) was inserted into the aorta from the distal end. The aorta was injured five times using the expanded balloon catheter containing 0.2 mL of air. 6 mg of peptide-NP conjugates (6 mg/mL) were incubated in the aorta for 10 min under constant pressure, using silk threads to secure both ends of the aorta. Non-adsorbed NPs were washed away using Hanks buffer and the abdominal aorta was sectioned at serial intervals of 90 µm.

Results

Synthesis of Fibrin-Targeted Hybrid NPs.

To assemble the targeted-NPs, peptides were covalently conjugated via their thiol end-groups to maleimide-terminated DSPE-PEG polymers (DSPE-PEG-Mal) (**Figure 2A**). The peptide-targeted lipid-polymer NPs were self-assembled from these components through a single-step nanoprecipitation technique (**Figure 2B**). The polymer/solvent was added dropwise into a lipid solution heated above the phase transition temperature, vortexed, and allowed to undergo self-assembly and solvent evaporation for 2 h at RT. An ultracentrifugation step removed excess solvent and lipid molecules.

Characterization of Physicochemical Properties of Targeted-NPs.

As shown in **Figure 2C**, non-targeted bare NPs were 60.2 ± 0.6 nm (mean \pm SD, n=3) and the attachment of pentapeptide sequences to NP surfaces resulted in a minimal increase in NP size to 61.8 ± 0.4 nm. In **Figure 2D**, the surface charge of the NPs became more negative from -17.75 ± 0.46 mV (mean \pm SD, n=3) to -56.22 ± 1.24 mV in water. Presumably, peptide conjugation presents a carboxylic acid terminal group at the NP corona, which resulted in a more negative surface charge. These zeta potential values will be closer to neutral in PBS buffers from charge screening. Transmission electron microscopy (TEM) images show that spherical sub-100 nm NPs were formed by nanoprecipitation (**Figure 2E**).

Targeting of Thin-Cap Fibroatheroma in ApoE^{-/-} Mice Fed an Atherogenic Diet.

The targeting of CREKA-NPs to fibroatheromas in ApoE^{-/-} mice was examined *ex vivo*. Two negative controls were designated: D-amino acid optical isomers (D-CREKA) and scrambled CEAKR sequences (S-CREKA). For this study, A647-PLGA encapsulated targeted-NPs were used to visualize the NPs while excluding interference from tissue autofluorescence.

A647-PLGA encapsulated NPs were incubated in mice aortas for 10 min under constant pressure. Subsequently, non-adsorbed NPs were washed away using Hanks buffer. The aortic arch and left brachiocephalic artery branch points were harvested for H&E staining and fluorescence imaging. First, a preliminary visual inspection of H&E stained sections using bright field microscopy was done to screen for plaques (**Figure 3**, bottom row). The selected cross-sections that had plaques were used as a reference to investigate NP binding in adjacent unstained sections by fluorescence microscopy (**Figure 3**, top row). An overlay of A647 fluorescence and phase contrast images (**Figure 3**, middle row) shows fluorescent NPs bound to plaques.

Effective binding was observed in representative cross-sections of CREKA-NPs to ApoE^{-/-} mice aortas (**Figure 3A**), whereas minimal binding was observed for NPs surface-modified with D-CREKA (**Figure 3B**) or S-CREKA (**Figure 3C**), suggesting that general non-specific adsorption or ionic interactions were insufficient for effective targeting. Control C57BL/6 mice fed a chow diet were used as controls for healthy aorta. CREKA-NPs showed negligible binding to these aortas (**Figure 3D**) which suggests that low-affinity NP adsorption may be removed by *in vivo* circulatory blood flow, or from multiple washes in this study.

Targeting of Revascularized Stenotic Lesions in Balloon-Injury Rat Models.

Revascularization of stenotic lesions creates significant endothelial denudation and basement membrane exposure, leading to a concerted action of platelets, a cascade of coagulation factors and fibrin production on the vessel wall that forms the bulk of the clot. We used a rat model of balloon-catheter injury to model an angioplasty procedure and confirmed that balloon injury caused severe damage to the vascular endothelium (**Figure 4**). H&E and Verhoeff-van Gieson (VvG) stained cross-sections show normal aortas with intact endothelial cell layers. Cross-sections of balloon-injured rat aortas show an absent endothelial monolayer.

The binding of CREKA-NPs *ex vivo* was examined in rat models of percutaneous angioplasty. A647-PLGA encapsulated targeted-NPs were incubated in aortas for 10 min under constant pressure. Non-adsorbed NPs were washed away using Hanks buffer and aortas were harvested for histological sectioning. Representative fluorescence images of aorta cross-sections

showed that CREKA-NPs bound to the balloon-injured rat aorta (**Figure 5A**). The overlay of fluorescence and phase contrast images identifies the arterial wall where the NPs are bound. In parallel experiments, NPs surface-modified with D-CREKA (**Figure 5B**) or S-CREKA (**Figure 5C**) showed negligible binding to balloon-injured rat aortas. CREKA-NPs incubated with uninjured rat aortas also showed undetectable binding to intact arteries (**Figure 5D**).

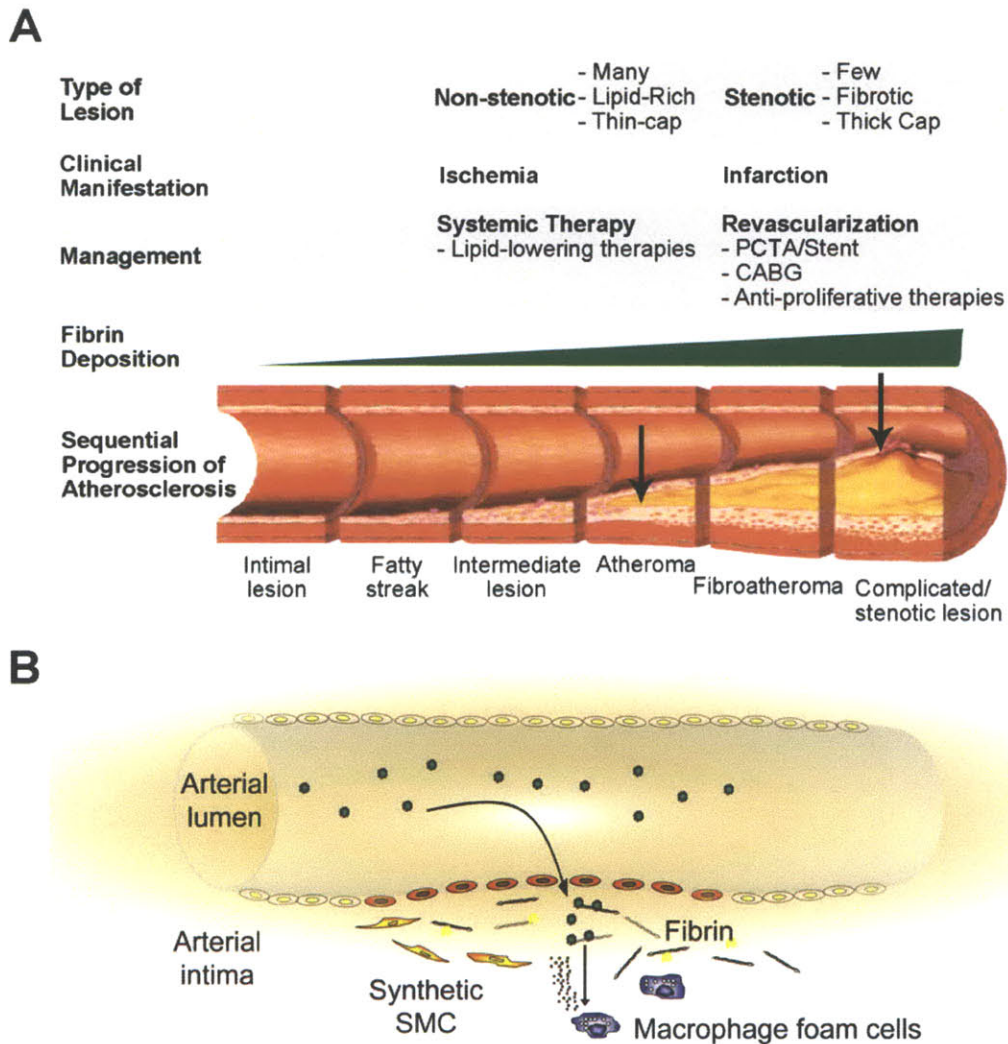


Figure 1. Fibrin-targeting for a diversity of lesions in human coronary atherosclerosis.

(A) Schematic of the progression of atherosclerosis. During atherogenesis, there is a corresponding increase in endothelial dysfunction and fibrin deposition, which may result in complicated, stenotic lesions that require revascularization. Arrows indicate suggested points of intervention and treatment. (B) Enhanced vascular permeability due to endothelial inflammation and reduced tight-junction integrity allow the NPs to extravasate into the plaque. By binding to fibrin deposits at lesions, targeted-NPs can act as a drug depot for sustained drug release against lipid-laden macrophage foam cells and proliferating smooth muscle cells (SMC).

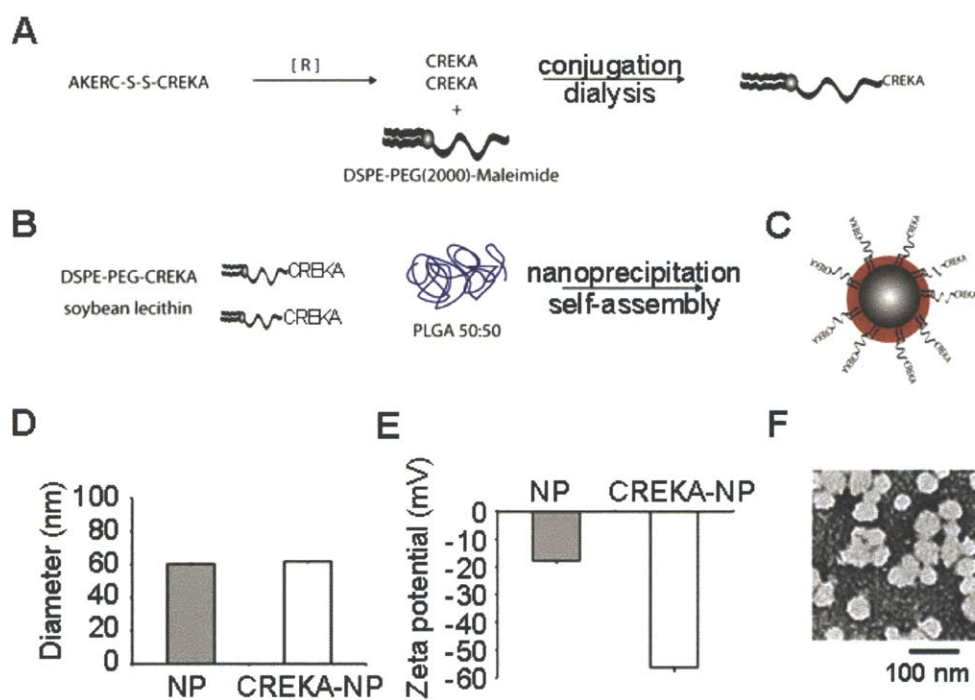


Figure 2. NP synthesis for fibrin-targeted drug delivery.

(A) Synthesis of lipid-PEG-peptide copolymers. Peptides are reduced, conjugated with DSPE-PEG2000 and dialyzed to remove unconjugated peptides. (B) Targeted NP synthesis by modified nanoprecipitation and self-assembly. (C) CREKA-functionalized lipid-polymer hybrid NPs have a PLGA hydrophobic core, a hydrophilic lipid-PEG-CREKA shell and a soybean lecithin interface (red). (D) Diameter of hybrid NPs before and after peptide conjugation, respectively (mean \pm SD, n=3). (E) Zeta potential of hybrid NPs before and after peptide conjugation, respectively (mean \pm SD, n=3). (F) Transmission electron microscopy (TEM) image of peptide-functionalized NPs stained with 3% uranyl acetate solution. Scale bar, 100 nm.

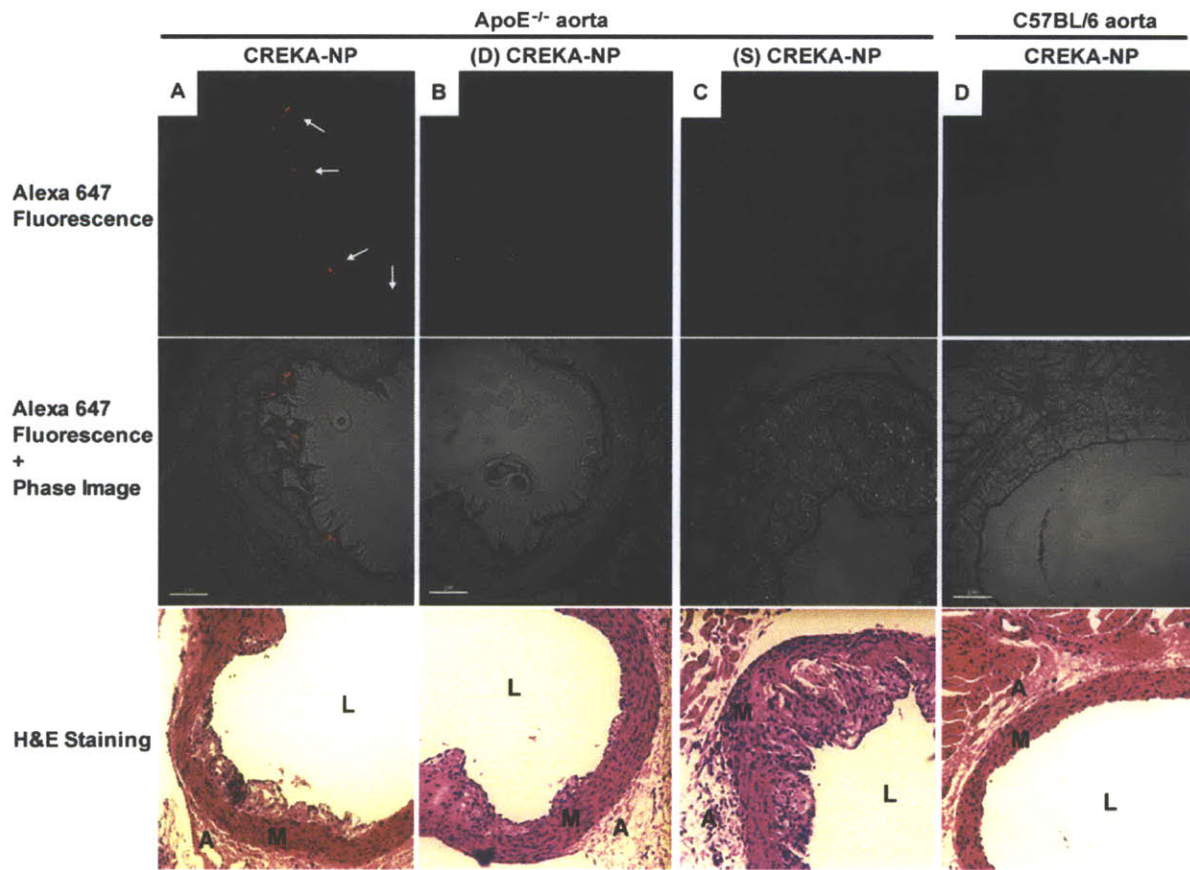


Figure 3. Targeting of thin-cap fibroatheroma in ApoE^{-/-} mouse aortas.

Top row: Fluorescence images of ApoE^{-/-} mouse aortas incubated with NPs that were surface-modified with (A) CREKA, (B) D-amino acid CREKA, (C) scrambled CREKA and (D) C57BL/6 mice aortas incubated with CREKA-NPs. A647-PLGA encapsulated NPs were incubated for 10 min and non-adsorbed NPs were washed away using Hanks buffer. Arrows indicate regions of NP deposition. Middle row: Overlay of the fluorescence and corresponding phase contrast image. Bottom row: H&E stained cross-sections showing plaque pathology corresponding to fluorescent images in the top row. L, lumen; M, media; A, adventitia. Scale bar, 100 μ m.

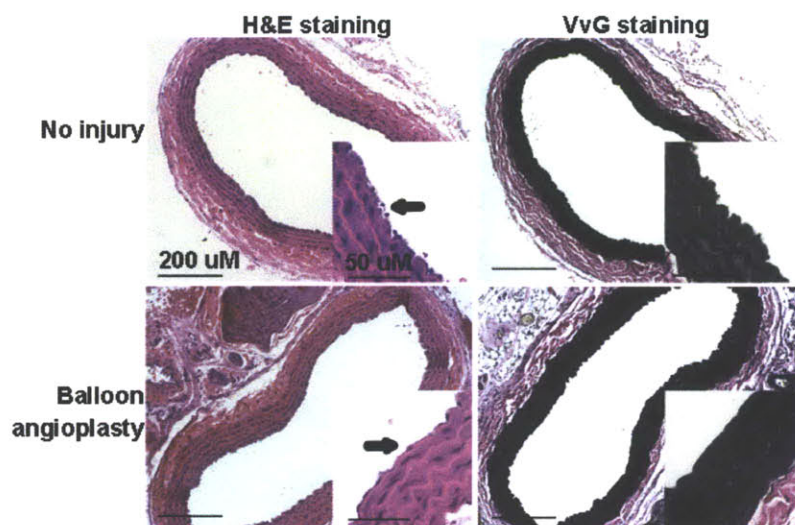


Figure 4. Uninjured and balloon-angioplastied aortas.

Representative H&E and Verhoeff-van Gieson (VvG) stained cross-sections of balloon-injured rat aortas and uninjured rat aortas. Arrows indicate the presence or absence of an endothelial monolayer. Scale bar, 200 μm . Inset: scale bar, 50 μm .

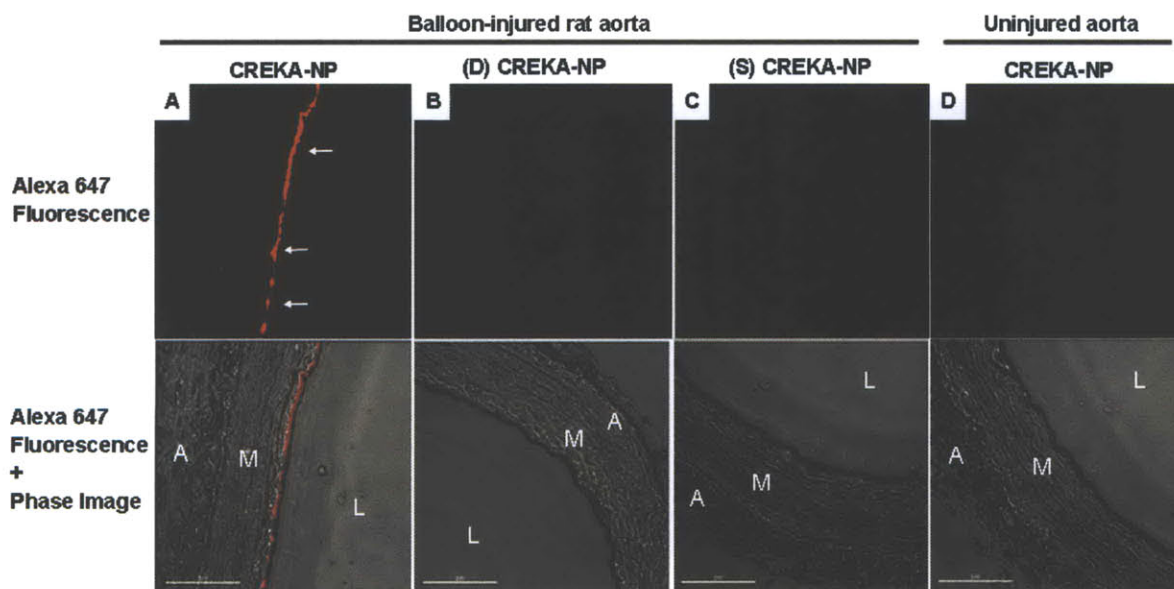


Figure 5. Targeting of revascularized lesions in balloon-injured rat aortas.

Top row: Fluorescence images of balloon-injured rat aortas incubated with NPs surface-modified with (A) CREKA, (B) D-amino acid CREKA, (C) scrambled CREKA and (D) uninjured rat aortas incubated with CREKA-NPs. Arrows indicate regions of NP deposition. Bottom row: Overlay of the fluorescence and phase contrast image. A647-PLGA encapsulated NPs were incubated for 10 min and non-adsorbed NPs were washed away using Hanks buffer. L, lumen; M, media; A, adventitia. Scale bar, 100 μm .

Discussion

The ideal features of a vascular-targeted NP platform are: (i) long circulating half-life to facilitate plaque accumulation, (ii) small size to enhance permeability into the endothelium, (iii) molecular targeting to enhance retention in the plaque, and (iv) controlled release of active agents from this extracellular depot (**Figure 1B**). The studies discussed here utilize biodegradable and biocompatible hybrid NPs which have a PLGA core for sustained drug release and a PEG shell for prolonged *in vivo* circulation half-life¹⁵. The lipid corona at the interface of the core and the shell allows for increased drug loading and lipid membrane-like properties^{13,14}. The molecular targeting ligand was a small-molecule peptide, CREKA, discovered from *in vivo* phage display screening in transgenic breast cancer mice¹¹. In both this study and Peters, D.A. *et al.*¹⁶, the targeting ligand was applied in a cardiovascular model despite being first discovered from a screen in a tumorigenesis model. This is possible because the general molecular mechanisms of neoangiogenesis can be applied to both oncologic and cardiovascular indications. These observations have led Folkman, J. *et al.* to describe neoangiogenesis as an ‘organizing principle’ which conceptually may be extrapolated across various diseases¹⁷.

Although therapy in humans is generally designed for subjects with advanced plaques, it is well known that these individuals also have plaques at earlier stages⁵. This study shows the targeting of early- to mid-stage lesions which may have single or multiple lipid cores and a thin fibrotic layer. Atherothrombosis is a complex interaction between lipids, inflammation and thrombosis, with vascular injury to the endothelium causing endothelial cells to lose their natural thromboresistance, leading sequentially to platelet activation, deposition of platelet and fibrin thrombi formation^{3,18}. Lipid-lowering statin therapies at doses lower than required for oral delivery may be delivered to plaques to reduce foam cell formation and inflammation².

For revascularized stenotic lesions, it may be possible to inhibit smooth muscle hyperplasia at the time of angioplasty with anti-proliferative drugs such as paclitaxel and sirolimus^{19,20}. Targeted-NP treatment presents a few advantages: it is independent of the revascularization method and stent implantation, avoids drug eluting stent (DES)-related long-term safety issues such as late stent thrombosis²¹, and allows for intervention at vascular branch

points²², multiple lesions, longer lesions and smaller arteries, all of which are currently off-label uses of DES²³.

Besides the therapeutic approaches discussed here, fibrin-targeting conjugates have been widely used as imaging agents in thromboembolic disease. Antibody fragments with high affinity for certain cross-linked fibrin peptide domains were used for imaging with either ultrasound or magnetic resonance imaging (MRI) contrast agents by Lanza, G. *et al.* in 1996²⁰. Using these fragments, thrombi formed *in situ* in canine carotid arteries were detectable within 30 min by ultrasound imaging²⁰. Another study used gadolinium-DTPA conjugates with fibrin-specific cyclic peptides as MRI probes for thrombosis^{24,25}. Fibrin is a useful target because it is the major protein constituent of clots and is present at 10-100 μM in the thrombus, a concentration range compatible for detection by gadolinium-based contrast agents.

In conclusion, CREKA-targeted NPs were able to differentially target fibrin in both a fat-fed mouse model genetically predisposed to atherosclerosis and in a balloon-injury rat model of angioplasty. Combined with previous studies of CREKA targeted micelles to complicated lesions in ApoE^{-/-} mice fed a 16-week high-fat diet¹⁶, the results reported here suggest a general application of fibrin-targeted NPs against diverse lesion types in atherosclerotic disease.

The knowledge built in **Chapter 4** from the design of peptide-targeted hybrid NPs and working with two animal models of atherosclerosis are applied in **Chapters 6** and **7**. Before that, we explore novel options for peptide-targeted NP drug delivery in **Chapter 5** through the investigation of alternative targets and discovery of novel ligands.

References

1. Braunwald, E. Shattuck lecture--cardiovascular medicine at the turn of the millennium: triumphs, concerns, and opportunities. *N Engl J Med* **337**, 1360-1369 (1997).
2. Sposito, A.C. & Chapman, M.J. Statin therapy in acute coronary syndromes: mechanistic insight into clinical benefit. *Arterioscler Thromb Vasc Biol* **22**, 1524-1534 (2002).
3. Hansson, G.K. Inflammation, atherosclerosis, and coronary artery disease. *N Engl J Med* **352**, 1685-1695 (2005).
4. Libby, P. & Theroux, P. Pathophysiology of coronary artery disease. *Circulation* **111**, 3481-3488 (2005).
5. Cheruvu, P.K., *et al.* Frequency and distribution of thin-cap fibroatheroma and ruptured plaques in human coronary arteries: a pathologic study. *J Am Coll Cardiol* **50**, 940-949 (2007).
6. Libby, P. Current concepts of the pathogenesis of the acute coronary syndromes. *Circulation* **104**, 365-372 (2001).
7. Libby, P. & Simon, D.I. Inflammation and thrombosis: the clot thickens. *Circulation* **103**, 1718-1720 (2001).
8. Stary, H.C., *et al.* A definition of advanced types of atherosclerotic lesions and a histological classification of atherosclerosis. A report from the Committee on Vascular Lesions of the Council on Arteriosclerosis, American Heart Association. *Arterioscler Thromb Vasc Biol* **15**, 1512-1531 (1995).
9. Eitzman, D.T., Westrick, R.J., Xu, Z., Tyson, J. & Ginsburg, D. Plasminogen activator inhibitor-1 deficiency protects against atherosclerosis progression in the mouse carotid artery. *Blood* **96**, 4212-4215 (2000).
10. Westrick, R.J., Winn, M.E. & Eitzman, D.T. Murine models of vascular thrombosis (Eitzman series). *Arterioscler Thromb Vasc Biol* **27**, 2079-2093 (2007).
11. Simberg, D., *et al.* Biomimetic amplification of nanoparticle homing to tumors. *Proc Natl Acad Sci U S A* **104**, 932-936 (2007).
12. Peters, D., *et al.* Targeting atherosclerosis by using modular, multifunctional micelles. *Proc Natl Acad Sci U S A* **106**, 9815-9819 (2009).
13. Zhang, L., *et al.* Self-assembled lipid-polymer hybrid nanoparticles: a robust drug delivery platform. *ACS Nano* **2**, 1696-1702 (2008).
14. Chan, J.M., *et al.* PLGA-lecithin-PEG core-shell nanoparticles for controlled drug delivery. *Biomaterials* **30**, 1627-1634 (2009).
15. Gref, R., *et al.* Biodegradable long-circulating polymeric nanospheres. *Science* **263**, 1600-1603 (1994).
16. Peters, D., *et al.* Targeting atherosclerosis by using modular, multifunctional micelles. *Proc Natl Acad Sci U S A* (2009).
17. Folkman, J. Angiogenesis: an organizing principle for drug discovery? *Nat Rev Drug Discov* **6**, 273-286 (2007).
18. Ross, R. Atherosclerosis--an inflammatory disease. *N Engl J Med* **340**, 115-126 (1999).
19. Brito, L. & Amiji, M. Nanoparticulate carriers for the treatment of coronary restenosis. *Int J Nanomedicine* **2**, 143-161 (2007).
20. Lanza, G., *et al.* Nanomedicine opportunities in cardiology. *Ann N Y Acad Sci* **1080**, 451-465 (2006).

21. Slottow, T.L. & Waksman, R. Drug-eluting stent safety. *Am J Cardiol* **100**, 10M-17M (2007).
22. Pendyala, L., *et al.* Review of percutaneous therapy for bifurcation lesions in the era of drug-eluting stents. *Minerva Cardioangiol* **56**, 89-105 (2008).
23. Mehran, R. & Dangas, G.D. Off-label use of drug-eluting stents: assessing the risk. *Nat Clin Pract Cardiovasc Med* **4**, 594-595 (2007).
24. Overoye-Chan, K., *et al.* EP-2104R: a fibrin-specific gadolinium-Based MRI contrast agent for detection of thrombus. *J Am Chem Soc* **130**, 6025-6039 (2008).
25. Nair, S.A., *et al.* Monovalent and bivalent fibrin-specific MRI contrast agents for detection of thrombus. *Angew Chem Int Ed Engl* **47**, 4918-4921 (2008).

Chapter 5. Screening of a Phage Display Library for the Discovery of Novel Targeting Peptides.

Abstract

In this study, we report a screen to identify novel materials that target vascular antigens of the endothelial basement membrane which are exposed in disease. We screened a M13 bacteriophage display library against collagen IV, the major component (50%) of the subendothelium. Combined with fibronectin, laminin, heparan sulfate proteoglycans and minor components, collagen IV provides a two-dimensional reticular network that supports the endothelial layer above it. After five rounds of phage display, one phage clone was found to bind with an IC_{50} value of 117 nM in competition binding assays against synthetic peptide equivalents on a Matrigel extract rich in collagen IV and laminin. In titer count analyses, this clone bound ~900-fold and ~300-fold over the original library to collagen IV and Matrigel respectively. NPs conjugated to these targeting peptides may potentially deliver therapeutic agents directly into the intimal and medial layers of arterial walls to improve treatment efficacy and reduce systemic side-effects. This type of non-cellular targeting may be relevant in a myriad of human diseases where the endothelial lining is compromised, including oncologic and cardiovascular inflammatory disease, or in diseases where neoangiogenesis is commonly observed.

The content of this chapter has been published in whole or in part in the following journal article:

Chan, J.M., Zhang, L., Tong, R., Ghosh, D., Gao, W., Liao, G., Yuet, K.P., Gray, D., Rhee, J.W., Cheng, J., Golomb, G., Libby, P., Langer, R. Farokhzad, O.C. Spatiotemporal controlled delivery of nanoparticles to injured vasculature. *Proc Natl Acad Sci U S A* (2010) **107**, 2213-2218. Reproduced in part with permission from *Proceedings of the National Academy of Sciences USA*. National Academy of Sciences © 2010.

Introduction

Phage display describes a powerful selection technology to engineer polypeptides that bind to a given target, such as to antibodies, enzymes and cell-surface receptors¹⁻³. It is a technique in which the protein or peptide library is expressed on the coat of a phage virion, while the genetic information encoding each variant resides on the inside. The physical linkage between each variant protein sequence and the DNA encoding it enables rapid and easy identification of individual variants based on binding affinity to a given target. High-affinity binders can be selected from a library of displayed proteins through an *in vitro* process called panning, by incubating the library on immobilized target molecules, washing away the unbound phages and eluting the bound phages⁴. The eluted phages are then amplified and taken through additional panning and amplification cycles to enrich the pool in favor of binding sequences (**Figure 1**). After 3-5 rounds, the sequences of individual clones can be rapidly deduced by DNA sequencing and characterized by enzyme-linked immunosorbant assays (ELISA).

Many phage display systems are based on M13 bacteriophage vectors¹⁻³. M13 filamentous bacteriophages (900 x 6 nm) are viruses composed of circular single stranded DNA (ssDNA) which is 6407 nucleotides long. The genome in a mature M13 virion is encapsulated in ~2700 copies of pVIII, the major coat protein, and capped with five copies of pIII, the minor coat protein clustered at the rounded end⁴. The pIII protein modulates phage infectivity by being the first protein to interact with its *Escherichia coli* host. During bacterial infection, the pIII protein attaches to the TolA protein receptor at the F-pilus tip. Likewise, the pIII protein is also the last point of contact as the phage buds from the bacterial surface, during which the N-terminal leader sequence is cleaved off. Infection with filamentous phages is not lethal and forms turbid non-lytic plaques in *E. coli*, with a modest decrease in the growth rate of infected cells. Peptides have been displayed in monovalent low-copy formats (1-5 copies) on the M13 phage through N-terminal fusions to the minor coat protein, pIII (**Figure 2**). Since the displayed peptide is sufficiently short (< 50 residues), the infectivity function of pIII is not affected and all five copies can carry displayed peptides without any measurable attenuation of phage infectivity³. Thus, monovalent phage display has been used to affinity mature many different proteins and to discover moderate to high affinity ligands (K_D of 10 μ M or better).

In this study, we utilized a M13 filamentous bacteriophage library to screen for ligands that may be used to target across a range of diseases in a consistent and reproducible manner⁵. Conventional molecular targeting of relevant cell-based protein epitopes can be confounded by inter- and intra-patient heterogeneity in cell surface antigen expression. Human cancers result from a complex series of genetic alterations that contribute to the complexity of the disease. Intratumoral heterogeneity is observed in 5-30% of breast tumors due to subclonal diversity within the tumor, such that less than 50% of tumor cells show HER2/neu epidermal growth factor receptor gene amplification and upregulation⁶. Advances in molecular profiling have also shown heterogeneous cell phenotypes in prostate cancer from key genetic processes such as alternative pre-mRNA splicing⁷. In mouse models, analysis of MMTV-Myc breast cancers reveal substantial heterogeneity in both histological and expression phenotypes⁸. Hence, human cancers are naturally heterogeneous disease states, making the targeting of cell-surface receptors less desirable in cases where heterogeneity is observed.

Many human diseases are associated with compromised vasculature and increased vascular permeability^{9,10}. This knowledge has enabled investigators to explore abundant non-cellular targets such as the coagulation cascade¹¹, intra-articular cartilage¹² and extracellular matrix¹³. Although it is widely known that endothelial denudation can cause a serious prothrombogenic stimulus¹⁴, we hypothesized that the exposed basement membrane may present a large surface area that can be targeted (**Figure 3**). Towards this goal, we selected for heptapeptide ligands by biopanning a phage library (approximately 10^9 independent clones, 100 copies per clone) against collagen IV¹⁵, which represents 50% of the vascular basement membrane¹⁶. We characterized specific ligands for targeting affinity against a Matrigel extract rich in collagen IV and laminin¹⁷. A phage clone displaying the peptide sequence, KLWVLPK, was found to bind to collagen IV with an IC_{50} value of 117 nm in peptide competition ELISA assays. In subsequent titer count analyses, this clone bound ~900-fold and ~300-fold over the original library to collagen IV and Matrigel respectively.

Methods

Materials.

Human collagen IV, human collagen I and Matrigel™ growth factor reduced LDEV-free were purchased from BD Biosciences (San Jose, CA). All peptides were custom synthesized by GenScript (Piscataway, NJ) with C-terminal amidation and purified by RP-HPLC to >95% purity by mass spectral analysis. LB medium, agar plates (LB/IPTG/X-gal, LB/tetracycline) and agarose top were purchased from Teknova (Hollister, CA). PEG8000, Tween-20 and BSA were purchased from Sigma. 96-well enzyme and radioimmunoassay (EIA/RIA) high-binding plates (Cat #3590) were purchased from Corning Life Sciences (Lowell, MA). Gamma-irradiated Linbro plate sealers with adhesive back (Cat #76403) were purchased from MP Biomedicals (Solon, OH).

Screening of Library.

The screen was performed according to the manufacturer's instructions and the Molecular Cloning laboratory manual by Sambrook, J. and Russell, D.W.¹⁸. The Ph.D.-7 phage library was obtained from New England Biolabs Inc. (Beverly, MA). Human collagen IV was diluted with 0.1 M NaHCO₃, pH 8.6 to ~10 µg/mL. A 96-well high binding plate was coated with 100 µL of collagen IV overnight at 4 °C, blocked (0.1 M NaHCO₃, 5 mg/mL BSA, pH 8.6) for 2 h at 4 °C and washed with TBST (50 mM Tris, 150 mM NaCl, pH 7.5, 0.1% Tween-20). Collagen IV-coated plates were incubated with 2×10^{11} plaque forming units (pfu) of phage virions in 100 µL 0.1% TBST for 1 h at RT. Unbound phages were removed by extensive washing with TBST. Bound phage were eluted by incubating for 5 min with 0.2 M glycine-HCl, 1 mg/mL BSA (pH 2.2) and neutralized with 1 M Tris-HCl (pH 9.1). The eluate was amplified (ref. *Amplification method*) and titered (ref. *Titering method*) to calculate an input volume corresponding to 2×10^{11} pfu for the next round of panning. In successive rounds of biopanning from R2-R5, the Tween-20 concentration was raised to 0.5% in both binding and washing steps. Also, the collagen IV enriched phage pool from R1 was subtractively panned against human collagen I for 1 h at RT before biopanning against collagen IV. In R5, 1 µg/mL collagen IV coated plates were used for

increased stringency. 15 clones per round from R3-R5 were randomly selected for DNA sequencing.

Phage Amplification and Precipitation.

A ~20 mL ER2738 *E. coli* culture was grown in a 250 mL Erlenmeyer flask until $OD_{600} = \sim 0.5$. The phage eluate was added to the culture and incubated for 4-5 h at 37 °C with vigorous shaking at ~220 rpm, followed by centrifugation at 10,000 rpm for 10 min at 4 °C (Thermo Scientific Sorvall SS-34 centrifuge). ~3.5 mL of 6x PEG/NaCl (200 g/L PEG8000, 146 g/L NaCl) was added to ~18 mL of the supernatant in a new tube to precipitate phage overnight at 4 °C. The next day, phages were centrifuged at 10,000 rpm for 15 min at 4 °C to precipitate phage. Pellets were resuspended with 1 mL of TBS in a microcentrifuge tube. 200 μ L of 6x PEG/NaCl was added and incubated on ice for 1 h at 4 °C. Phages were centrifuged at 10,000 rpm for 10 min at 4 °C to precipitate phage. Pellets were resuspended in 200 μ L TBS (0.02% NaN_3 for long-term storage) and stored at 4 °C. Plaque titer was counted for the next round of biopanning.

Titering and Measurement of Phage Plaque Forming Units.

PFU is a functional measurement rather than a measurement of the absolute quantity of phages which can be estimated by absorbance spectroscopy. Phages that are defective or which fail to infect bacteria will not produce a plaque and thus will not be counted. Power dilutions were made (e.g. 10^3 dilution: 1 μ L eluate to 1000 μ L LB medium) at suggested dilution ranges for amplified supernatants (10^8 - 10^{11}) and unamplified panning eluates (10^1 - 10^4). 200 μ L of an *E. coli* $OD_{600} = \sim 0.5$ culture was added to 10 μ L of each power dilution in a new centrifuge tube, briefly vortexed and incubated for 1-5 min at RT. The *E. coli*/phage solution was added to 5 mL of melted agarose top (25 g/L LB medium, 1 g/L $MgCl_2 \cdot H_2O$ and 7 g/L agarose) in a 15 mL polystyrene tube, briefly vortexed and poured onto pre-warmed LB/IPTG/X-gal plates. Once solidified, plates were inverted and incubated overnight at 37 °C. Plates with $\sim 10^2$ plaques were counted by the formula: $pfu/10 \mu L = \text{blue spots} \times 10^{\text{level dilution}}$ to derive the phage titer.

DNA Sequencing and Peptide Sequence Analysis.

~3 mL of an $OD_{600} = \sim 0.5$ culture was inoculated with a clone to be sequenced. Only blue colonies were picked as white colonies represent contaminating wild-type phages. Cultures were amplified for 4.5-5 h at 37 °C with shaking before they were centrifuged for 30 s at 10,000 rpm. Phage DNA was lysed and extracted from the supernatant with a QIAprep Spin M13 kit (Qiagen, Valencia, CA) and resuspended in water for storage at 4 °C. ~0.5 µg of phage DNA was sent for automated DNA sequencing at the MIT Biopolymers Laboratory using 20-mer -96 gIII sequencing primers (New England Biolabs).

Phage ELISA Matrigel Binding Studies.

96-well plates were coated with 100 µL 1/50 dilutions of Matrigel in TBS overnight at 4°C, or TBS buffer only. Plates were blocked with 3% BSA/TBS for 2 h at RT and washed three times. 10^{10} pfu of each phage clone was added in 0.5% TBST in triplicate to Matrigel and BSA-coated wells. Bound phage particles were detected with peroxidase-conjugated mouse anti-M13 monoclonal antibodies (mAb) at 1/5000 dilution (Amersham Pharmacia Biotech, Piscataway, NJ). After a 1 h incubation, the reaction was developed with 2,2'-azino-bis(3-ethylbenzthiazoline-6-sulphonic acid) (ABTS) (Amersham). The absorbance at 405 nm was read against a reference wavelength of 490 nm using a SpectraMax Plus 384 microplate reader (Molecular Devices, Sunnyvale, CA).

IC₅₀ Value Determination of Phage Clones.

Matrigel-coated and blocked 96-well plates were incubated in triplicate with 10^{-5} - 10^{-10} M peptide concentrations and 10^9 pfu of phage in 100 µL 0.5% TBST. After 1 h at RT, bound phages were labeled with anti-M13 mAbs and color was developed and detected by ABTS absorbance (405-490 nm). Peptide inhibition curves were normalized on a percentage scale. IC₅₀ values were calculated using a dose-response curve fit by the formula: $Y = \text{Bottom} + (\text{Top} - \text{Bottom}) / (1 + 10^{((\text{LogIC}_{50} - X) * \text{Hill Slope}))}$ (Origin 8 data analysis software, Northampton, MA).

Titer Count Analyses.

Matrigel and collagen IV-coated and blocked plates were incubated with a phage input of 10^{11} pfu per well in 0.5% TBST. Unbound phages were removed by extensive washing with TBST and bound phages were eluted and neutralized. The eluate was titered to get pfu values.

Statistical Analysis.

The student's t-test was used to determine significance. All error bars represent the SD of the mean. Differences were termed statistically significant at $P < 0.05$.

Results

Selection and Characterization of Basement Membrane Targeting Peptides for Vascular Wall Targeting.

To discover a functional vascular targeting peptide, a combinatorial library of random heptamers fused to the minor coat protein (pIII) of M13 filamentous phage was subjected to five rounds of biopanning against human collagen IV (**Figure 4**).

Excellent phage binders may be lost from previous rounds due to reduced fitness¹⁹. Possible reasons include reduced infectivity rates of phages for their *Escherichia coli* hosts due to low pH elution, disulfide-bond formation between cysteine containing phages resulting in the rarity of cysteine-rich sequences, faster growth rates of certain clones, or simply a founder effect when a fraction of amplified phages are input into the next round of biopanning. Hence, fifteen clones per round were randomly sequenced from Round 3 to 5 (R3-R5) (**Figure 5**) with 100% of the clones found to be C-8, HWGSLRA in R5. To find similarities to resident basement membrane structures, we searched the non-redundant version of the current National Center for Biotechnology Information (NCBI) *homo sapiens* sequence database using the pBLAST algorithm against peptides from the screen^{20,21}. Sequences were classified into three groups. The first group consists of peptides with similarity to resident basement membrane proteins such as

nidogen, serum amyloid P component, gelsolin and laminin¹⁶. The second group of peptides were enriched in proline residues, such as Pro-Pro-Ser (PPS) and Pro-Pro-Pro (PPP) runs, which resemble the Gly-Pro-Pro (GPP) motif in collagen triple helices¹⁵. Finally, the third group consists of unique peptides with no identifiable relationship with the basement membrane.

Matrigel ELISA Binding Assays of Phage Clones.

A binding experiment was performed to compare the relative affinities of the sequenced clones for Matrigel (**Figure 5**). 23 unique purified phage clones were incubated in triplicate on 96-well plates against Matrigel and BSA. The bound phages were then detected with HRP-conjugated anti-M13 mAbs. Phages were ranked according to absorbance values indicating their binding capacity to Matrigel (mean \pm SD, n=3). No reactivity was observed against BSA compared with the original library (R0). Despite the similarity of the PP motifs with collagen IV, Group B peptides showed less binding affinity compared to Group A and C, and showed no detectable binding affinity above the library to Matrigel. Clones A-8, A-9, C-10 and C-11 were the best candidates, and we noted that these four clones resembled each other.

Since the amount of target protein coated on the plate is not quantifiable and is present at sufficiently high density to allow multivalent binding to the phage, phage ELISA will not determine absolute affinity constants. However, this method is useful as (i) it provides a qualitative determination of the relative binding affinities of 23 selected clones in parallel with the R0 library, and (ii) it distinguishes true target binding from binding to BSA or polystyrene wells.

Clones A-8, A-9, C-10 and C-11 were aligned pairwise using CLUSTAL 2.0.10 and the Jalview multiple sequence alignment editor. The consensus sequence generated was KIWVLPQ, or more generally, KZWXLPX, where Z is a hydrophobic amino acid and X is any amino acid (**Figure 6A**). The Jalview program gives the Quality, Conservation and Consensus of the alignment. Quality is an ad-hoc measure of the likelihood of observing mutations (if any) in a particular column of the alignment. Conservation is measured as a numerical index reflecting the conservation of physicochemical properties in the alignment. The consensus is the percentage of the modal residue per column (**Figure 6B**).

Sequence Specific Competition Assays of Phage Clones.

For more detailed binding and inhibition studies, free peptides modeled after phage clones A-8, A-9, C-10 and C-11 were synthesized. This allows precise control of peptide concentration without the avidity artifacts associated with pentavalent phage display. Additionally, without the phage attached, the peptide can be used at much higher concentrations. During biopanning, the N-terminus of the displayed sequence was free while the C-terminus was fused to the phage. Consequently, a free C-terminus will introduce a negatively charged group at a position occupied by a neutral peptide bond during panning, which may completely abolish binding. To block the negative charge, the C-terminal carboxylate of the synthetic peptide was amidated. A Gly-Gly-Gly-Ser peptide spacer was also added to the C-terminus of the peptide to resemble the phage-displayed format.

In a sequence-specific competition assay, we analyzed the context-dependence of the phage towards the peptide-collagen IV binding interaction. Synthetic peptides modeled after phage clones A-8, A-9, C-10 and C-11 competitively inhibited their cognate phage in a dose-dependent manner on Matrigel-coated surfaces (**Figure 7**). Phage C-11 showed the best peptide competition which suggests that the binding of C-11 may be independent of the phage context and represent a specific peptide-collagen IV interaction. Peptide A-9 ($IC_{50} = \sim 551$ nM) proved to be less inhibitory than C-11 ($IC_{50} = \sim 117$ nM), although its cognate phage exhibited the highest binding capacity in **Figure 2A**. Even though IC_{50} readings are dependent on conditions at which they are measured and not an absolute indicator of binding affinity, IC_{50} values of half-maximal inhibition on a dose-response curve are related to K_D affinity constants and can approximate for binding affinity.

Titer Count Analyses of Phage Clones.

Considering that phage C-11 gave the best IC₅₀ values, we further examined the binding of phage C-11 in three independent titer count analyses (**Figure 8**). Phage C-11 and the original library (R0) were incubated at an initial input of 10¹²/mL pfu on Matrigel- and collagen IV-coated plates. C-11 showed ~300-fold Matrigel binding and ~900-fold collagen IV binding over the library (p < 0.001, mean ± SD, n=3).

Epitope Mapping by Phage Display.

The A-6 phage clone (TPLPANL) showed similarity to a sequence within the *H. sapiens* serum amyloid P component (SAP), TPLPANIL. A-6 had a leuΔile substitution at the seventh position of the SAP sequence, but the hydrophobic character at this amino acid position is maintained. Furthermore, the eight position on the SAP sequence is also a leucine residue. SAP is the precursor of amyloid P component, a universal constituent of abnormal tissue deposits in amyloidosis. Studies have shown that SAP is a resident of vascular basement membranes²² and more specifically, SAP was shown to bind to both collagen IV²³ and laminin²⁴ *in vitro*. Annotations to the SAP protein structure²⁵ from the RCSB Protein Data Bank showed that the TPLPANIL sequence is found on the exposed face of each pentameric subunit (**Figure 9A**). In the presence of high Ca²⁺ concentrations, SAP rapidly aggregates and precipitates, but in the absence of Ca²⁺ it forms a very stable decameric structure composed of two pentameric discs interacting face-to-face²⁶. The TPLPANIL sequence is still exposed on the surface in SAP decamers (**Figure 9B**). C-reactive protein (CRP), another member of the pentraxin family, was shown to bind to C1q via a sequence²⁷ which aligns to the TPLPANIL sequence (**Figure 9C, 9D**).

Considering the homologous positions of these two sequences, it is possible that the phage display screen may have mapped the SAP epitope for collagen IV. During the divergent evolution of the pentraxin family, amino acid changes of this epitope could have resulted in their divergent locations, with amyloid P as an amyloid deposit and physiological component of basement membranes²², and CRP as an acute-phase protein elevated during inflammation²⁸. A-6 was not chosen for functional studies as it was not the best binder in the affinity assay against Matrigel (**Figure 5**). Taken together, these findings suggest that the pool of phage display

selected peptides may contain biologically-relevant collagen IV binders supported by reports in the literature.

Selection and Characterization of Basement Membrane Targeting Peptides against Matrigel.

In a separate phage display screen, the R0 phage library was subjected to three rounds of biopanning against Matrigel growth factor reduced, LDEV-free (**Figure 10A**) instead of collagen IV. Likewise, sequenced phage clones were subject to pBLAST against the NCBI *homo sapiens* sequence database (**Figure 10B**). A Matrigel ELISA binding assay was performed to compare the affinities of Matrigel-selected clones against collagen IV-selected clones (**Figure 10C**). In contrast to the higher affinity binders from the collagen IV selection, Matrigel-selected clones were poorer Matrigel binders. Considering the higher complexity of the target this time, it was most likely necessary to pan the library for a few more rounds until a consensus sequence is reached. However, since we had a family of lead candidates from the collagen IV selection (**Figure 5**), Matrigel-selected clones were not further characterized.

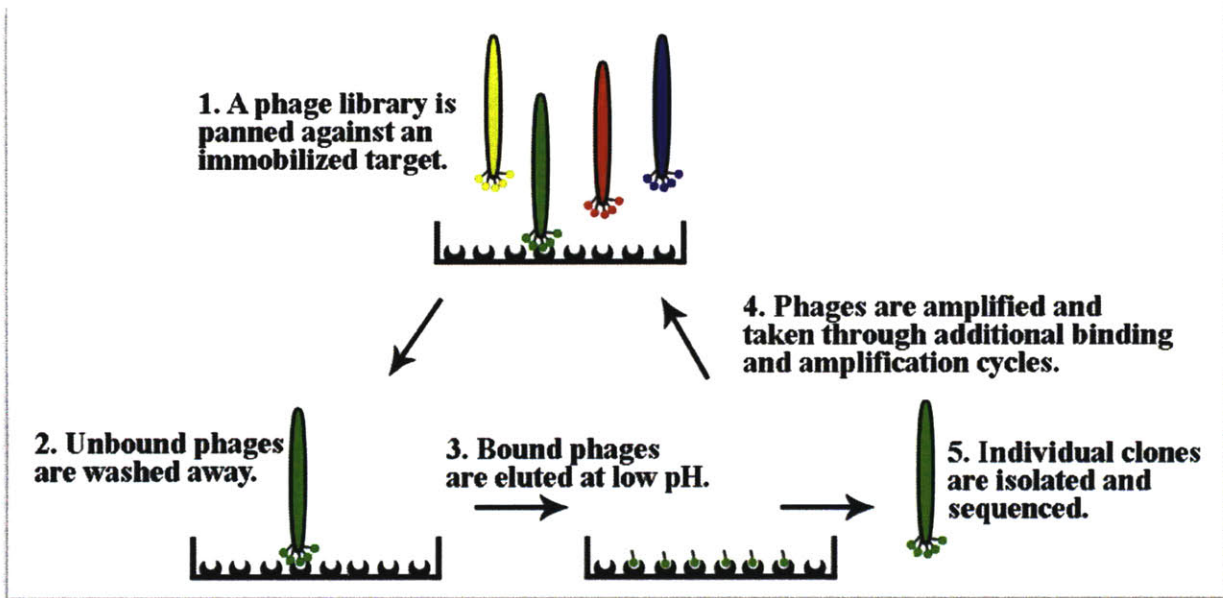


Figure 1. Panning with a pentavalent peptide library displayed on pIII.

From a library of displayed proteins, high-affinity binding phages can be selected *in vitro* by panning on an immobilized target, washing away unbound phages and eluting bound phages. The eluted phages are then amplified and taken through additional binding and amplification cycles to enrich the pool in favor of binding sequences. Individual clones are picked and subject to further characterization and DNA sequencing.

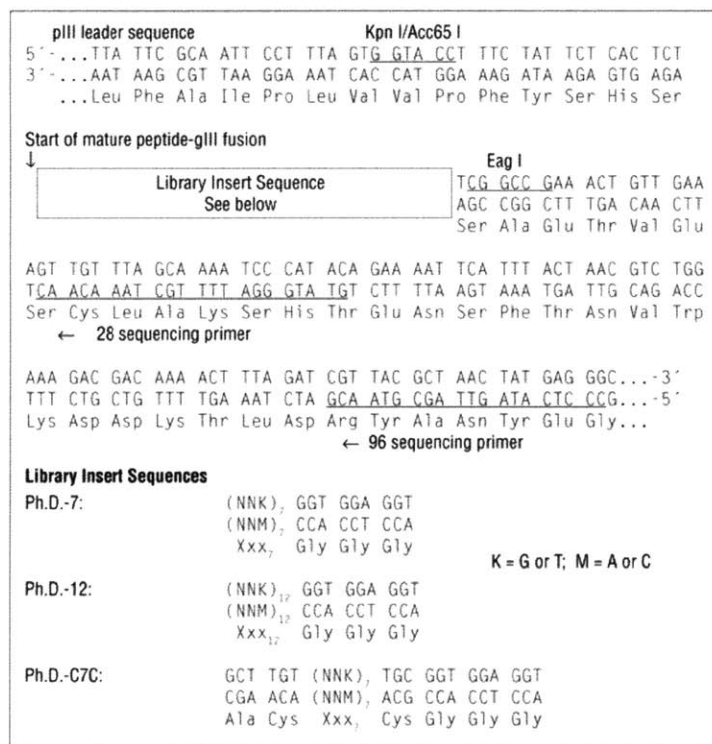


Figure 2. Sequence of the peptide cloning site where the library is inserted into the M13KE phage genome.

Each library is expressed with an N-terminal leader sequence that is removed upon secretion, resulting in the randomized peptide positioned directly as a peptide library–N-terminal fusion to the minor coat protein (pIII). The hybridization positions of the -28 and -96 sequencing primers are indicated. The third position of each codon is limited to G or T at the randomized positions to improve relative representations of each amino acid. This figure is reproduced from the New England Biolabs Ph.D.-7 library manual.

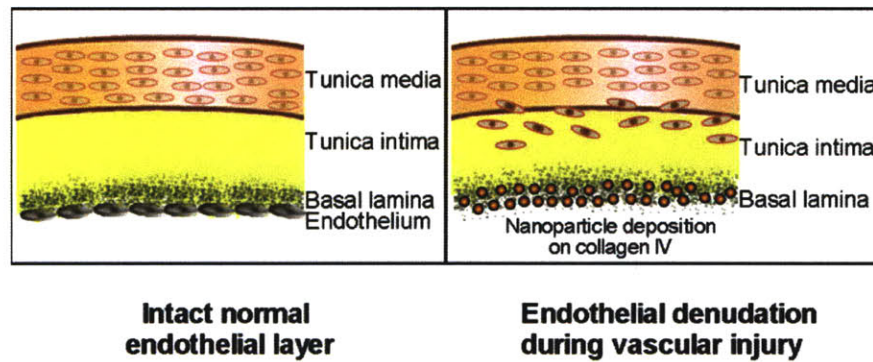


Figure 3. Illustration of targeting to the basement membrane.

The basal lamina is not exposed when the endothelial layer is healthy and intact. During chronic disease, the endothelial layer is breached and the underlying basal lamina is exposed. Targeting the vasculature provides a conduit through which active molecules can be distributed to layers of the vessel wall, such as the tunica media. During vascular injury, contractile smooth muscle cells (SMC) migrate from the tunica media into the tunica intima (as depicted in the right diagram) and become synthetic and proliferative.

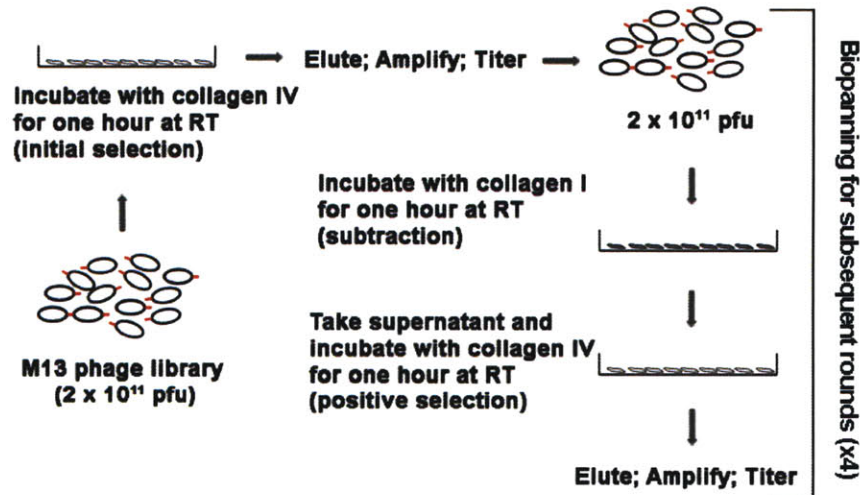


Figure 4. Schematic of phage display selection strategy.

During the initial selection, the phage library was panned against human collagen IV. In R2 to R5, the collagen IV enriched phage pool was subtractively panned against human collagen I. 15 clones per round were randomly picked for further biochemical analysis and DNA sequencing.

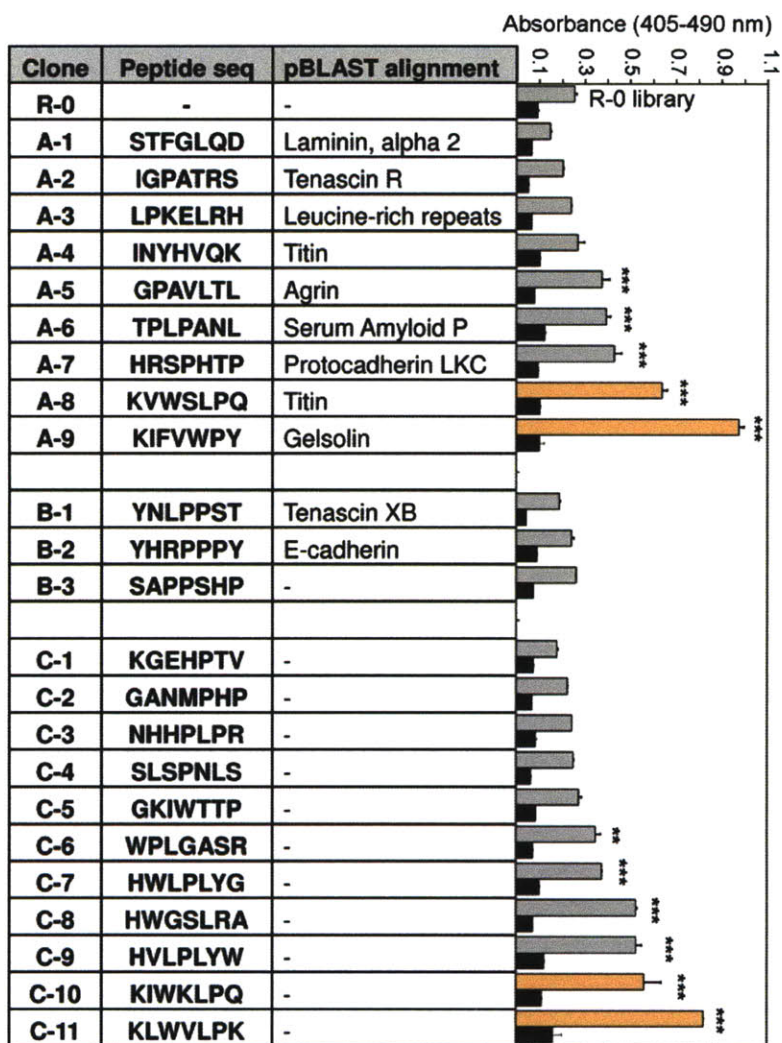


Figure 5. Identification and characterization of peptides for targeting to the basement membrane.

Twenty-three phage clones from Rounds 3-5 of the phage display screen. Group A: Peptide sequences that show similarity to resident basement membrane proteins or contain collagen binding-motifs analyzed by pBLAST against the NCBI *H. sapiens* nonredundant protein sequence database. Group B: Sequences that resemble the collagen IV GPP triple helix. Group C: Sequences with no identifiable relationship to resident basement membrane structures. The clones were tested against the library (R0) for binding to Matrigel (lighter shaded bars) and BSA (black bars). Bound phages were labeled with peroxidase-conjugated anti-M13 mAbs, and ABTS absorbance was read at 405 nm against a reference wavelength of 490 nm (mean \pm SD, n=3). **, P < 0.01; ***, P < 0.001 all compared with R0 (one-way ANOVA with Tukey post hoc test).

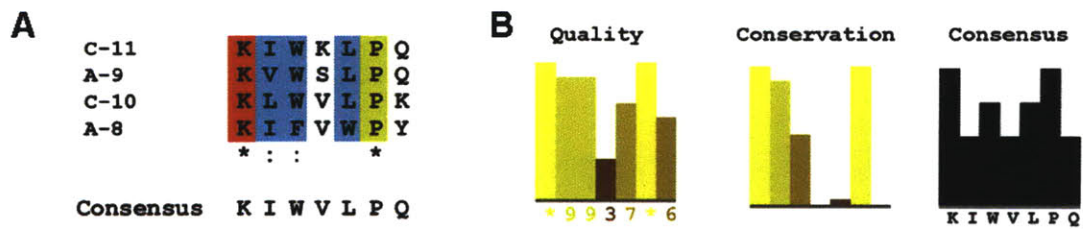


Figure 6. Alignment and consensus sequence.

Sequences were viewed and aligned by (A) CLUSTAL 2.0.10 and (B) the Jalview multiple sequence alignment editor.

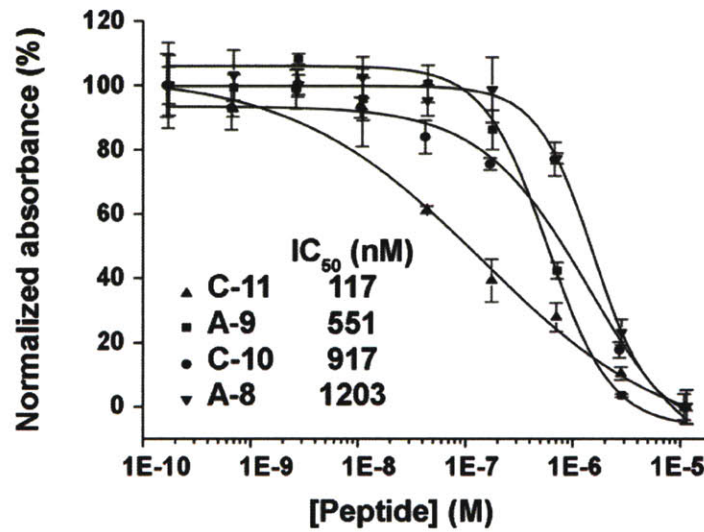


Figure 7. Sequence-specific competition binding assays.

Phage clones A-8, A-9, C-10, and C-11 were competed against synthetic peptide equivalents on Matrigel extracts and showed a dose-response relationship. IC₅₀ values were determined and normalized on a percentage scale by the formula: $Y = \text{Bottom} + (\text{Top} - \text{Bottom}) / (1 + 10^{((\text{LogIC}_{50} - X) * \text{Hill Slope}))}$ (mean \pm SD, n=3). (▲) C-11; (■) A-9; (●) C-10; (▼) A-8.

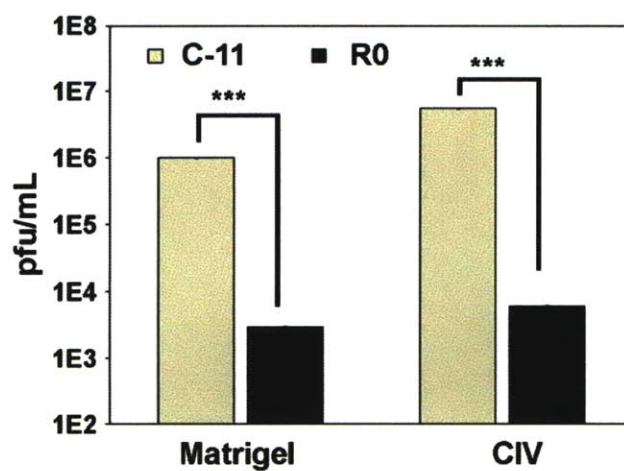


Figure 8. Titer count analyses of C-11 compared to the R0 phage library on Matrigel and collagen IV.

Titers of eluted phages were averaged to give values of pfu/mL (mean \pm SD, n=3). ***, P < 0.001 by a paired two-sample Student's t-test.

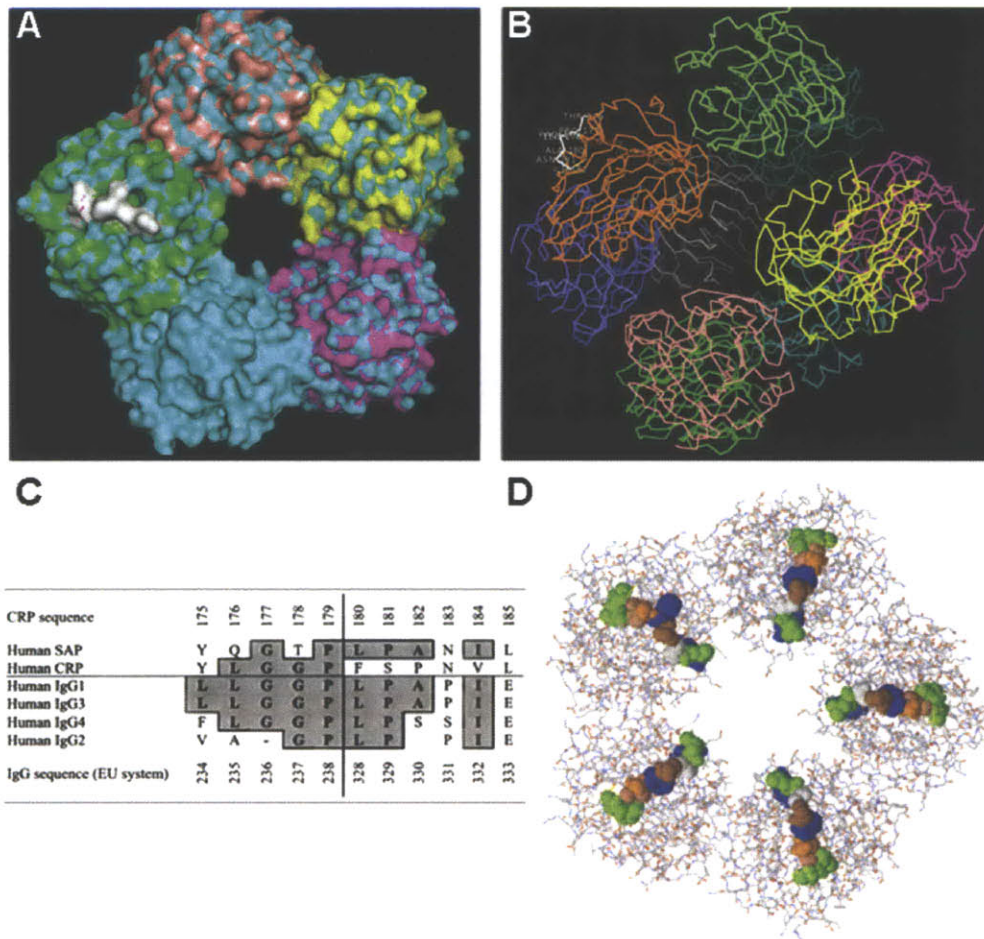


Figure 9. Epitope mapping using phage display.

The A-6 phage clone (TGPLPANL) shows similarity to a sequence within serum amyloid P component, TGPLPANIL. (A) The SAP protein structure²⁵ (RCSB Protein Data Bank) is displayed using the PyMol program (Schrodinger Computational Chemistry, Cambridge, MA). The TGPLPANIL sequence (white) is found on the exposed face of each pentameric subunit and also (B) on the exposed face of the SAP decamer (white)²⁶. (C) C-reactive protein (CRP), another member of the pentraxin family, was shown to bind to C1q via amino acids 175-185 that align to the location of the TGPLPANIL sequence. (D) Ball-and-stick stereo structure of CRP with amino acids 175-185 highlighted. Figures 10C and 10D were originally published in the Journal of Biological Chemistry. Bang, R. *et al.* Analysis of binding sites in human C-reactive protein for Fc γ RI, Fc γ RIIA, and C1q by site-directed mutagenesis. *J Biol Chem* (2005) **280**, 25095-102. Reproduced in part with permission from The American Society for Biochemistry and Molecular Biology © 2005.

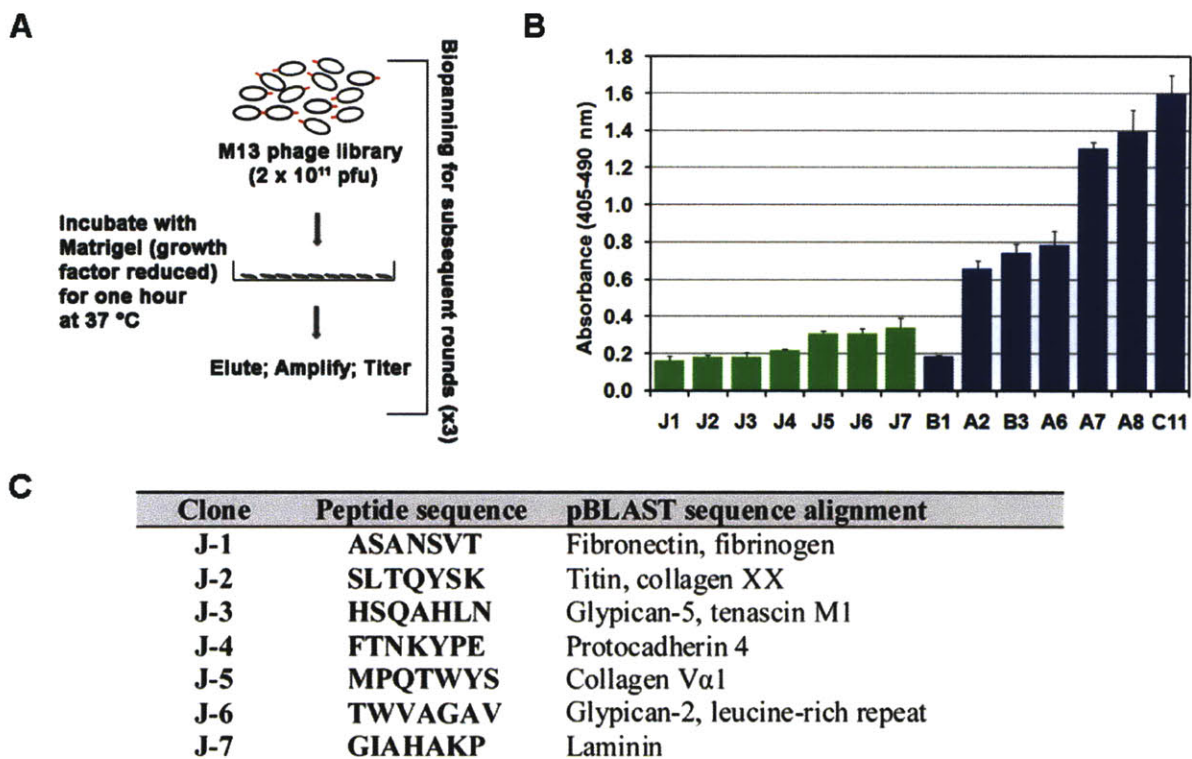


Figure 10. Phage display strategy against Matrigel matrices.

(A) Schematic of phage display strategy. The phage library was panned against Matrigel (GF-reduced, LDEV-free). 15 clones from round 3 were randomly picked for DNA sequencing and further biochemical analysis. (B) Some of the clones from this screen (green bars) were tested against clones from the collagen IV screen (blue bars) for binding to Matrigel. Bound phages were labeled with peroxidase-conjugated anti-M13 mAbs and ABTS absorbance was read at 405 nm against a reference wavelength of 490 nm (mean \pm SD, n=3). (C) Clones chosen for analysis were sequences that showed similarity to resident basement membrane proteins analyzed by pBLAST against the NCBI *H. sapiens* nonredundant protein sequence database.

Discussion

The pIII-displayed M13 filamentous bacteriophage library used in this study was suitable for the selection of small heptameric peptides present in low copy number (1-5 copies per phage). However, other phage display formats may be more relevant for applications that require larger peptide ligands or antibody fragments, and for cases where high-copy number display is required.

For polyvalent high-copy display, pVIII major coat protein display may be used to select for peptide affinity combined with an avidity effect. However, a number of issues may arise, ranging from varying display levels based on the length and sequence of the fusion protein, to unstable phages when fusion peptides are more than six residues in length. Newer studies have found ways to mutate the pVIII coat protein for improved polyvalency of display²⁹. When the displayed protein is large, such as scFv antibody fragments with > 50 residues, the displayed library has to be constructed into phagemid systems. Phagemids are hybrids of M13 phages and plasmids, and can grow both as a plasmid (origin of replication, *ori*, for dsDNA replication) and phage (f1 *ori* for ssDNA replication). Here, bacterial infection requires a 'helper' phage to provide the wild-type pIII and pVIII *in trans* for single-stranded DNA replication and phagemid DNA packaging into phage particles.

More recently, yeast display methods have been developed to enable researchers to incorporate larger fragments into yeast genomes^{30,31}. A eukaryotic host should alleviate expression biases present in bacterially-propagated combinatorial libraries, such as reduced arginine levels due to arginine interference with *secY*-dependent secretion of pIII³². Unlike phage display, yeast display methods can be used to screen for mammalian cell-surface receptors, secreted antibodies and cytokines which require post-translational processing by the endoplasmic reticulum and quality control mechanisms of the eukaryotic secretory pathway. However, disadvantages include smaller yeast library sizes and differential glycosylation in yeast compared to mammalian cells.

With a myriad of options available for screening peptides and antibody fragments, the applications of these systems are limited only by the imagination of researchers performing the screen. Libraries have been used to discover anti-microbial³³ and anti-viral peptides^{34,35}, material-specific peptides³⁶, cell-targeting peptides³⁷, small-molecule binders such as intracellular targets of paclitaxel³⁸, and even to map uncharacterized protein-protein interactions³⁹. Peptides that home in on tumors and various organs *in vivo* have also been discovered^{40,41}. Even though *in vivo* phage display has been used successfully before, several problems are encountered during *in vivo* panning such as: (i) phages experience significant hydrodynamic drag and convective forces in arterial flow which causes them to marginate away from vessel walls, (ii) the inability to block high non-specific binding, and (iii) in particular, the unwarranted randomness in the selection due to short contact times and incomplete exposure of phage diversity to the vasculature because nearly all of the injected phages are scavenged by the RES in minutes⁴².

In **Chapter 4**, a pentameric fibrin-binding peptide, CREKA, was used to target platelet/fibrin clots on atherosclerotic plaques. Here, we discover a family of collagen IV-binding peptides that we tested on Engelbreth-Holm-Swarm (EHS) mouse sarcoma basement membrane extracts. Other screening methods were also considered in the event this strategy did not lead to successful binders. For instance, we could pan the library against laminin or heparan sulfate proteoglycans which constitute 30% and 10-20% of the basement membrane, respectively. Alternatively, we could phage display angioplastied arteries *ex vivo* or *in vivo*. Finally, scFv phagemid libraries were also considered because antibody fragments generally show greater specificity and affinity for their targets compared to peptides. These strategies were not tested because the selected peptides gave suitable IC₅₀ inhibition values. When peptides are functionalized onto NPs, the synergistic effect from having multiple peptide-receptor interactions may improve on the overall targeting affinity.

Within this study, a number of heptameric sequences showed sequence similarity to resident basement membrane structures such as titin, agrin, cadherin and laminin. In all cases, 5 out of 7 amino acids must show sequence identity during alignment to qualify as being similar. Not all of these sequences may amount to functional targeting ligands on NPs, since some of them did not perform significantly better than the original library in ELISA assays against

Matrigel. However, the observation that some of the recovered peptides resemble basement membrane proteins suggests a biological consequence of this screen. This is consistent with previous reports that phage display can play a significant role in mapping epitopes of known binders³⁸ and in mapping uncharacterized protein-protein interactions³⁹. Other studies have characterized the SAP-collagen IV interaction *in vitro* but a binding site was never proposed²³. Although we postulate that we have identified the binding site of SAP to collagen IV, this hypothesis remains to be experimentally verified by IC₅₀ inhibition assays against SAP and site-directed mutagenesis studies.

In conclusion, we discovered a family of candidate peptides that may be functionally tested as targeting ligands on NPs. We hypothesized that we could target the endothelial basement membrane in diseases with chronic vascular injury and inflammation. In **Chapter 6**, we surface-functionalized the hybrid NPs with our candidate peptide ligands and tested the targeted-NPs for delivery to injured vasculature *ex vivo* and *in vivo*.

References

1. Scott, J.K. & Smith, G.P. Searching for peptide ligands with an epitope library. *Science* **249**, 386-390 (1990).
2. Devlin, J.J., Panganiban, L.C. & Devlin, P.E. Random peptide libraries: a source of specific protein binding molecules. *Science* **249**, 404-406 (1990).
3. Cwirla, S.E., Peters, E.A., Barrett, R.W. & Dower, W.J. Peptides on phage: a vast library of peptides for identifying ligands. *Proc Natl Acad Sci U S A* **87**, 6378-6382 (1990).
4. Russel, M., Linderoth, N.A. & Sali, A. Filamentous phage assembly: variation on a protein export theme. *Gene* **192**, 23-32 (1997).
5. Chan, J.M., *et al.* Spatiotemporal controlled delivery of nanoparticles to injured vasculature. *Proc Natl Acad Sci U S A* **107**, 2213-2218 (2010).
6. Vance, G.H., *et al.* Genetic heterogeneity in HER2 testing in breast cancer: panel summary and guidelines. *Arch Pathol Lab Med* **133**, 611-612 (2009).
7. Rajan, P., Elliott, D.J., Robson, C.N. & Leung, H.Y. Alternative splicing and biological heterogeneity in prostate cancer. *Nat Rev Urol* **6**, 454-460 (2009).
8. Andrechek, E.R., *et al.* Genetic heterogeneity of Myc-induced mammary tumors reflecting diverse phenotypes including metastatic potential. *Proc Natl Acad Sci U S A* **106**, 16387-16392 (2009).
9. Folkman, J. Angiogenesis: an organizing principle for drug discovery? *Nat Rev Drug Discov* **6**, 273-286 (2007).
10. Ross, R. Atherosclerosis--an inflammatory disease. *N Engl J Med* **340**, 115-126 (1999).
11. Peters, D., *et al.* Targeting atherosclerosis by using modular, multifunctional micelles. *Proc Natl Acad Sci U S A* **106**, 9815-9819 (2009).
12. Rothenfluh, D.A., Bermudez, H., O'Neil, C.P. & Hubbell, J.A. Biofunctional polymer nanoparticles for intra-articular targeting and retention in cartilage. *Nat Mater* **7**, 248-254 (2008).
13. O'Neil, C.P., *et al.* Extracellular matrix binding mixed micelles for drug delivery applications. *J Control Release* **137**, 146-151 (2009).
14. Liu, M.W., Roubin, G.S. & King, S.B., 3rd. Restenosis after coronary angioplasty. Potential biologic determinants and role of intimal hyperplasia. *Circulation* **79**, 1374-1387 (1989).
15. Hudson, B.G., Reeders, S.T. & Tryggvason, K. Type IV collagen: structure, gene organization, and role in human diseases. Molecular basis of Goodpasture and Alport syndromes and diffuse leiomyomatosis. *J Biol Chem* **268**, 26033-26036 (1993).
16. Kalluri, R. Basement membranes: structure, assembly and role in tumour angiogenesis. *Nat Rev Cancer* **3**, 422-433 (2003).
17. Kleinman, H.K., *et al.* Isolation and characterization of type IV procollagen, laminin, and heparan sulfate proteoglycan from the EHS sarcoma. *Biochemistry* **21**, 6188-6193 (1982).
18. Sambrook, J. & Russell, D.W. *Molecular cloning : a laboratory manual*, (Cold Spring Harbor Laboratory Press, Cold Spring Harbor, N.Y., 2001).
19. Smith, G.P. & Petrenko, V.A. Phage Display. *Chem Rev* **97**, 391-410 (1997).
20. Altschul, S.F., *et al.* Gapped BLAST and PSI-BLAST: a new generation of protein database search programs. *Nucleic Acids Res* **25**, 3389-3402 (1997).

21. Schaffer, A.A., *et al.* Improving the accuracy of PSI-BLAST protein database searches with composition-based statistics and other refinements. *Nucleic Acids Res* **29**, 2994-3005 (2001).
22. Dyck, R.F., *et al.* Amyloid P-component is a constituent of normal human glomerular basement membrane. *J Exp Med* **152**, 1162-1174 (1980).
23. Zahedi, K. Characterization of the binding of serum amyloid P to type IV collagen. *J Biol Chem* **271**, 14897-14902 (1996).
24. Zahedi, K. Characterization of the binding of serum amyloid P to laminin. *J Biol Chem* **272**, 2143-2148 (1997).
25. Emsley, J., *et al.* Structure of pentameric human serum amyloid P component. *Nature* **367**, 338-345 (1994).
26. Ashton, A.W., Boehm, M.K., Gallimore, J.R., Pepys, M.B. & Perkins, S.J. Pentameric and decameric structures in solution of serum amyloid P component by X-ray and neutron scattering and molecular modelling analyses. *J Mol Biol* **272**, 408-422 (1997).
27. Bang, R., *et al.* Analysis of binding sites in human C-reactive protein for Fc{gamma}RI, Fc{gamma}RIIA, and C1q by site-directed mutagenesis. *J Biol Chem* **280**, 25095-25102 (2005).
28. Danesh, J., *et al.* C-reactive protein and other circulating markers of inflammation in the prediction of coronary heart disease. *N Engl J Med* **350**, 1387-1397 (2004).
29. Sidhu, S.S., Weiss, G.A. & Wells, J.A. High copy display of large proteins on phage for functional selections. *J Mol Biol* **296**, 487-495 (2000).
30. Boder, E.T. & Wittrup, K.D. Yeast surface display for screening combinatorial polypeptide libraries. *Nat Biotechnol* **15**, 553-557 (1997).
31. Boder, E.T., Midelfort, K.S. & Wittrup, K.D. Directed evolution of antibody fragments with monovalent femtomolar antigen-binding affinity. *Proc Natl Acad Sci U S A* **97**, 10701-10705 (2000).
32. Peters, E.A., Schatz, P.J., Johnson, S.S. & Dower, W.J. Membrane insertion defects caused by positive charges in the early mature region of protein pIII of filamentous phage fd can be corrected by prlA suppressors. *J Bacteriol* **176**, 4296-4305 (1994).
33. Dharmasena, M.N., Jewell, D.A. & Taylor, R.K. Development of peptide mimics of a protective epitope of Vibrio cholerae Ogawa O-antigen and investigation of the structural basis of peptide mimicry. *J Biol Chem* **282**, 33805-33816 (2007).
34. Welch, B.D., VanDemark, A.P., Heroux, A., Hill, C.P. & Kay, M.S. Potent D-peptide inhibitors of HIV-1 entry. *Proc Natl Acad Sci U S A* **104**, 16828-16833 (2007).
35. Yang, B., *et al.* Potent suppression of viral infectivity by the peptides that inhibit multimerization of human immunodeficiency virus type 1 (HIV-1) Vif proteins. *J Biol Chem* **278**, 6596-6602 (2003).
36. Whaley, S.R., English, D.S., Hu, E.L., Barbara, P.F. & Belcher, A.M. Selection of peptides with semiconductor binding specificity for directed nanocrystal assembly. *Nature* **405**, 665-668 (2000).
37. Kelly, K.A., *et al.* Detection of early prostate cancer using a hepsin-targeted imaging agent. *Cancer Res* **68**, 2286-2291 (2008).
38. Rodi, D.J., *et al.* Screening of a library of phage-displayed peptides identifies human bcl-2 as a taxol-binding protein. *J Mol Biol* **285**, 197-203 (1999).
39. Nelson, T.J. & Alkon, D.L. Protection against beta-amyloid-induced apoptosis by peptides interacting with beta-amyloid. *J Biol Chem* **282**, 31238-31249 (2007).

40. Pasqualini, R. & Ruoslahti, E. Organ targeting in vivo using phage display peptide libraries. *Nature* **380**, 364-366 (1996).
41. Kelly, K.A., Nahrendorf, M., Yu, A.M., Reynolds, F. & Weissleder, R. In vivo phage display selection yields atherosclerotic plaque targeted peptides for imaging. *Mol Imaging Biol* **8**, 201-207 (2006).
42. Valadon, P., *et al.* Screening phage display libraries for organ-specific vascular immunotargeting in vivo. *Proc Natl Acad Sci U S A* **103**, 407-412 (2006).

Chapter 6. Spatiotemporal Targeting of Nanoparticles to Injured Vasculature.

Abstract

There are a number of challenges associated with designing NPs for medical applications. We define two challenges here: (i) conventional targeting against up-regulated cell surface antigens is limited by heterogeneity in expression, and (ii) previous studies suggest that the optimal size of NPs designed for systemic delivery is approximately 50-150 nm, yet this size range confers a high surface area-to-volume ratio which results in fast diffusive drug release. For spatial control, we functionalize 60-nm hybrid NPs with novel peptides from a phage display screen against collagen IV. For temporal control, we load the hybrid NPs with slow-eluting conjugates of paclitaxel for controlled ester hydrolysis and drug release over 10-12 days *in vitro*. The targeted-NPs inhibited human aortic smooth muscle cell proliferation in cultures embedded on collagen IV matrices and showed greater *in vivo* vascular retention during percutaneous angioplasty over non-targeted controls. This NP technology may potentially be used toward the treatment of injured vasculature, a clinical problem of primary importance.

The content of this chapter has been published in whole or in part in the following journal article:

Chan, J.M., Zhang, L., Tong, R., Ghosh, D., Gao, W., Liao, G., Yuet, K.P., Gray, D., Rhee, J.W., Cheng, J., Golomb, G., Libby, P., Langer, R. Farokhzad, O.C. Spatiotemporal controlled delivery of nanoparticles to injured vasculature. *Proc Natl Acad Sci U S A* (2010) **107**, 2213-2218. Reproduced in part with permission from *Proceedings of the National Academy of Sciences USA*. National Academy of Sciences © 2010.

Introduction

The field of nanotechnology has crossed significant milestones from the systemic delivery of NPs¹⁻⁵. However, the ability to overcome *in vivo* barriers towards tissue-specific drug delivery at therapeutically-relevant levels remains an elusive goal. Both spatial and temporal control of therapeutic agents may be essential to many medical applications. In this study, we engineer a NP system that fundamentally changes the way we achieve spatiotemporal control of drug delivery.

We designed ~60-nm core-shell hybrid NPs^{6,7} consisting of a polymeric core, a lipid interface and a PEG corona. For temporal control, we achieved the capacity for slow drug elution over two weeks using poly(lactic acid) (PLA) conjugates of paclitaxel (Ptxl)⁸ made by a modified drug-alkoxide ring-opening strategy^{9,10}. Drug burst release is a long-standing challenge in NP formulation and conventional NPs typically demonstrate a burst release of 60-90% of their payload within 24 h because drug release is controlled mainly by diffusion. These conjugates allow for controlled drug release by gradual ester hydrolysis despite the large surface area and short diffusion distances of sub-100-nm particles. Herein, we report the synthesis of Ptxl-PLA conjugates initiated by Ptxl and catalyzed by BDIZnTMS₂, an active catalyst for chemo- and region-selective polymerizations of lactide. The drug release profile of these conjugates is determined not only by diffusion but also by the hydrolysis of the Ptxl-PLA linker, giving a ~10-12 day Ptxl release. These NPs were also shown to inhibit human aortic smooth muscle cell proliferation *in vitro*.

For spatial control, the NPs were functionalized with ligands^{11,12} from the phage display screen described in **Chapter 5**. Here, a combinatorial library of 10⁹ independent clones was panned against collagen IV¹³ which represents 50% of the vascular basement membrane¹⁴. Eluted phage clones were characterized for their relative targeting affinities against a Matrigel extract rich in collagen IV and laminin¹⁵. Many human diseases are associated with compromised vasculature and increased vascular permeability^{16,17} and we exploit these vascular breaches by targeting the underlying basement membrane. Hence, targeted delivery of

therapeutics to these vascular breaches may be a powerful means to achieve efficient delivery to the vascular wall and improve on the efficacy of NP-based drug delivery.

Previous reports suggest that NPs show a size cut-off for retention when delivered by angioplasty into vascular walls. 100 nm polystyrene NPs transmigrated into the medial area whereas 500 nm NPs remained along the vascular lumen¹⁸. 90 nm tyrophostin-loaded PLA NPs also showed better drug deposition and improved anti-restenotic outcomes compared to larger 160 nm NPs¹⁹. In theoretical studies, once the sub-100 nm NPs are decorated with ligands and delivered to diseased vasculature, unlike larger leukocytes or monocytes that roll stably over the vessel wall, targeted NPs which are smaller by nearly two orders of magnitude are predicted to search for the biological target in a ‘bee-like mode’, jumping abruptly from one adhesion site to another. In general, sub-100 nm NPs experience smaller dislodging forces, and combined with the binding affinities of targeting ligands, produce larger molecular bond rupture forces and shorter times for firm adhesion²⁰.

We used angioplasty-injured vasculature as a model of compromised vasculature to examine the utility of our NPs²¹. We delivered the targeted NPs via both intraarterial (IA) and i.v. administration and showed greater *in vivo* vascular retention at sites of injured vasculature in the rat compared to non-targeted NPs. Inspired by the adhesive nature of burr seeds, which are covered by “hooks” that bind onto abundant exposed surfaces, we named our system “nanoburrs” for their adhesive quality at sites of injured vasculature. The nanoburr system may be administered systemically for a myriad of human diseases where the endothelial lining is compromised, including oncologic¹⁶ and cardiovascular inflammatory disease^{16,17,22}.

Methods

Materials.

All peptides were custom synthesized by Genscript (Piscataway, NJ) with C-terminal amidation and purified by RP-HPLC to >95% purity by mass spectral analysis. Peptides were synthesized with a linker sequence (GGGC) at the C-terminus for thiomaleimide coupling. Alexa Fluor 647 hydrazide tris(triethylammonium) salt was purchased from Invitrogen (Carlsbad, CA). All materials were bought from Sigma-Aldrich unless otherwise noted.

Paclitaxel-Polylactide Conjugation.

[(BDI)ZnN(TMS)₂] [(BDI=2-((2,6-diisopropylphenyl) amino)-4-((2,6-diisopropylphenyl)imino)-2-pentene, TMS=trimethylsilyl] (6.2 mg, 0.01 mmol) and Ptx1 (8.5 mg, 0.01 mmol) (Sigma) were mixed in 0.5-mL anhydrous THF. D,L-lactide (36 mg, 0.25 mmol) in 2 mL anhydrous THF was added dropwise to initiate polymerization. Lactide was completely consumed within hours at RT and monitored by FTIR or ¹H NMR spectroscopy. The polymerization solution was added to ethyl ether (25 mL) to precipitate out the Ptx1-PLA₂₅ conjugate (approximately 25 dL-lactide monomer units, 19.2 wt% Ptx1).

Synthesis and Characterization of Nanoburrs.

A 3 mL DSPE-PEG/lecithin mixture in 4% ethanol containing 0.17 mg DSPE-PEG-Maleimide/DSPE-PEG (1:4 molar ratio) and 0.08 mg lecithin was heated for 3 min above the lipid phase transition temperature to 68 °C under gentle stirring. Next, 1 mg of Ptx1-PLA in acetone (1 mg/mL) was added dropwise at 1 mL/min. The solution was vortexed vigorously for 3 min followed by self-assembly under gentle stirring for 2 h at RT. The NPs were washed three times using a 30 kDa MWCO Amicon Ultra-4 centrifugal filter (Millipore). The NPs were resuspended in pH 7.2 PBS buffer and 2 mM EDTA and incubated with peptides (MW=1137.54 Da) at a 1/2 molar ratio to DSPE-PEG-Mal for 45 min at RT. The peptides were previously reduced using Bond-breaker TCEP solution, Neutral pH (Thermo Scientific) in PBS-EDTA at a 1/1 disulfide bond/TCEP molar ratio. Free peptides were removed using a Sephadex PD-10 (G-

25) column. For scale-up, multiple vials of NPs were made with concentrations and volumes kept constant to maintain small NP diameters. TEM images of the nanoburrs (1 mg/mL) were obtained by negative-staining with 3% uranyl acetate. Size (diameter, nm) and surface charge (zeta potential, mV) were evaluated by quasi-elastic laser light scattering using a ZetaPALS dynamic light-scattering detector (15 mW laser, incident beam=676 nm; Brookhaven Instruments).

Release Kinetics Studies.

To assess the Ptx1–PLA bond, Ptx1 and Ptx1–PLA conjugates were subject to RP-HPLC using an Agilent 1100 HPLC equipped with a pentafluorophenyl column (Curosil-PFP, 250 × 4.6 mm, 5 µm; Phenomenex). Ptx1 and Ptx1–PLA absorbance was measured with an UV–vis detector at 227 nm in a 1/1 acetonitrile/1% trifluoroacetic acid 1 mL/min nongradient mobile phase. To quantify the Ptx1–PLA drug release profile, a 2 mg nanoburr sample was divided equally into 30 Slide-A-Lyzer MINI dialysis microtubes, 20 kDa MWCO (Pierce). The remaining Ptx1–PLA was quantified at various time points by RP-HPLC. Experiments were carried out in triplicate in PBS at 37 °C.

HaSMC Cytotoxicity Studies.

96-well plates were Matrigel-coated and BSA-blocked (as described in **Chapter 4**) in PBS. HaSMC were plated at 10,000 cells/well in a 37 °C, 5% CO₂ incubator and grown for 24 h in Medium 231 supplemented with 10 µg/mL gentamycin, 0.25 µg/mL amphotericin B and smooth muscle growth supplement (all from Cascade Biologics, Invitrogen). Treatment groups (n=5) included nanoburrs, scrambled-peptide NPs, non-targeted NPs, fourfold dilutions of Ptx1 (in maximum 0.1% DMSO) in media and a media-only control. Samples were incubated with cells for 45 min. The wells were washed two times with complete media and replaced with fresh complete media for 48 h. Medium 231 was replaced with phenol red-free RPMI medium supplemented with 10% FBS containing [3-(4,5-dimethylthiazol-2-yl)-5-(3-carboxymethoxyphenyl)-2-(4-sulfophenyl)-2H-tetrazolium, inner salt] (MTS) and phenazine methosulfate (PMS) and incubated for 2 h at 37 °C (CellTiter 96AQueous Non-Radioactive Cell

Proliferation Assay; Promega). Formazan product formation was measured by absorbance at 490 nm against a reference wavelength of 650 nm.

Animals.

Sprague-Dawley rats weighing approximately 450-500 g were obtained from Charles River Laboratories and fed a normal rodent diet. All animal procedures were conducted by a certified contract research organization using protocols consistent with local, state, and federal regulations as applicable and approved by the Institutional Animal Care and Use Committee.

Balloon-Angioplasty Ex Vivo Studies.

For *ex vivo* studies, animals were sacrificed for open abdominal cavity surgery *in situ*. Aortas were flushed with saline and injured by four passages of a Fogarty arterial embolectomy 2F balloon catheter (Model 120602F; Edwards Lifesciences) in a rotating fashion. Alexa Fluor 647 (A647) dyes were covalently conjugated to PLGA (viscosity 0.19 dL/g) using EDC/NHS chemistry in DMF. A647-PLGA conjugates were precipitated in 2/1 ethyl ether/methanol by centrifugation, dried in vacuum, and resuspended in acetone for NP preparation. Fluorescence (rfu) was quantified using a GeminiXPS microplate spectrofluorometer (Molecular Devices), and samples were diluted accordingly in PBS for comparable NP delivery into the aortas. 0.4 mL samples (approximately 6 mg/mL) were incubated in the aorta for 5 min using metal clips to secure both ends of the aorta. Non adsorbed samples were flushed away with saline using an Advance Infusion Pump Series 1200 syringe pump (Roboz Surgical Instrument Co.) programmed at 4 mL/min for 15 min.

Balloon-Angioplasty In Vivo Studies.

For *in vivo* IA studies, animals were anesthetized intramuscularly with ketamine (60 mg/kg)/xylazine (10 mg/kg) and given buprenorphine as an analgesic. Left common carotids were injured by four passages of the 2F balloon-catheter, before a 30-gauge tubing was inserted via the external carotid into the common carotid and advanced beyond the angioplastied region

into the aortic arch. Samples (approximately 10 mg/mL) were infused at 1 mL/min for 1 min. The external carotids were permanently ligated. The animals were sacrificed 1 h after surgery, and the carotids were harvested. For i.v. studies, animals were additionally given heparin (500 IU/kg) by i.v. injection immediately before surgery. The animals underwent left common carotid artery surgery and samples (approximately 15 mg/mL) were given by 1 mL i.v. tail vein injections. The animals were sacrificed after 1 h and the carotids were harvested.

Optical Imaging and Fluorescence Microscopy Studies.

Tissues were fixed in 4% paraformaldehyde/4% sucrose/saline overnight at 4 °C. Whole tissue sections were imaged simultaneously using the IVIS Imaging System200 Series (Caliper Life Sciences, Hopkinton, MA) at 640/700 (ex/em) wavelength, exposure time=1 s, binning=medium, F/Stop=2. Tissue sections were overlaid onto photographs taken at binning=medium, F/Stop=8. After IVIS imaging, the same tissues were OCT-frozen and cut to give approximately 10 μM sections for fluorescent microscopy. Representative H&E stained slides were also made from paraffin-fixed sections. All histology sections were done by the MIT Koch Institute Histology Facility and imaged using a DeltaVision RT deconvolution microscope using the 10x or 20x objective (Applied Precision Inc.).

Statistical Analysis.

One-way ANOVA with post hoc Tukey tests were used to determine significance. All error bars represent the SD of the mean. Differences were termed statistically significant at $P < 0.05$.

Results

Synthesis and Characterization of the Nanoburr Drug Delivery System.

To investigate the targeting properties of the candidate peptide against the basement membrane, peptides were covalently conjugated onto hybrid NPs that have a hydrophobic drug-eluting core, a hydrophilic polymeric shell, and a lipid monolayer⁷. PEG¹ covalently conjugated to 1,2-distearoyl-sn-glycero-3-phosphoethanolamine (DSPE) was used to form the hydrophilic polymeric shell. To complete the lipid monolayer, soybean lecithin, which is considered Generally Regarded as Safe (GRAS), was used to form the core-shell interface. For the hydrophobic drug-eluting core, paclitaxel–polylactide (Ptxl–PLA) conjugates were synthesized by a drug/alkoxide-initiated ring-opening polymerization strategy¹⁰. Ptxl was mixed with equimolar amounts of [(BDI)ZnN-(TMS)₂] [BDI=2-((2,6-diisopropylphenyl)amino)-4-((2,6-diisopropylphenyl) imino)-2-pentene, TMS=trimethylsilyl]⁹ and the (BDI)Zn–Ptxl complex formed *in situ* subsequently initiated and completed the polymerization of lactide within hours at RT (**Figure 1A**). Ptxl was shown to be conjugated to the terminals of PLA by comparing the elution profile of free Ptxl to Ptxl–PLA by RP-HPLC. Ptxl–PLA eluted at approximately 21 min instead of eluting at the original 13-14 min Ptxl peak (**Figure 1B**).

In **Figure 2**, nanoburr synthesis is illustrated in which the core (Ptxl–PLA conjugate) and shell (lipid and lipid–PEG) are integrated via nanoprecipitation and self-assembly. We conjugated the KLWVLPK peptide via a C-terminal GGGC linker to DSPE–PEG–maleimide using maleimide-thiol conjugation chemistry. The size and surface zeta potential of nonfunctionalized NPs in water were 57.3 ± 0.4 nm (mean \pm SD) (**Figure 3A**) and -12.83 ± 2.73 mV (mean \pm SD) (**Figure 3B**), respectively. Peptide attachment resulted in an approximately 1-nm size increase and made the surface charge cationic (13.5 ± 5.9 mV, mean \pm SD), presumably because the peptides were N-terminally exposed to retain their original phage-displayed orientation. TEM showed the spherical structures of nanoburrs (**Figure 3C**). To characterize the nanoburrs physiochemically, we quantified their release kinetics by taking aliquots (n=3) at scheduled time points for RP-HPLC analysis (**Figure 3D**). Ptxl is released by diffusion when the Ptxl–PLA ester bond is hydrolyzed, and the amount of Ptxl released from Ptxl–LA₂₅ was 43.4% on day 2, and 91.0% and 93.8% on day 10 and day 12, respectively.

Targeted Drug Release from Nanoburrs.

To validate the therapeutic efficacy of this treatment, a human aortic smooth muscle cell (haSMC) cytotoxicity study was used to assess nanoburr binding affinity on Matrigel-coated wells with haSMC (**Figure 4**). To test the sequence specificity of the KLWVLPK peptide (T), two controls were designated: scrambled PWKKLLV peptide (S) and non-targeted (B) NPs. In addition, we included a media-only control and fourfold dilutions of free Ptxl in DMSO (maximum 0.1% DMSO in media). The maximum free Ptxl concentration used was 51 μM , exceeding by two log scales a suitable Ptxl dose range of 50-1,000 nM for haSMC cytotoxicity. An incubation time of 45 min was significantly shorter than typical incubation times with Ptxl (approximately 4-24 h). The wells were rinsed twice with complete media and further incubated with fresh media for 48 h. Unlike free Ptxl which is removed during the washing step, the nanoburrs attached to the collagen IV matrix were retained for continued Ptxl release. Hence, lowered formazan product formation (490 nm absorbance) reflects increased haSMC cytotoxicity as a function of greater targeted-NP retention on Matrigel-coated plates (n=5, $P < 0.001$).

Binding Studies in Angioplasty Models of Injured Vasculature.

We evaluated the targeting affinity of the nanoburr system toward injured vasculature. To create those vascular characteristics, a Fogarty 2-French balloon catheter was used to injure rat arteries by repeatedly advancing, inflating the balloon, and withdrawing to denude the endothelial monolayer and expose the basement membrane. This loosely mimics a percutaneous angioplasty procedure in human patients, the difference being that in human patients the catheter is inflated locally in a preexisting stenotic lesion. In **Figure 5**, a representative H&E stained cross-section shows an injured aorta with the endothelial layer removed, and an uninjured aorta with an intact endothelial monolayer.

Ex Vivo Binding Studies in Angioplastied Aortas.

Our *ex vivo* study examined targeting of the nanoburr system to balloon-injured rat aortas. A647–PLGA conjugates were used as a substitute for Ptx1–PLA drug conjugates to visualize the nanoburrs by fluorescence microscopy and optical imaging. This wavelength is beyond the autofluorescence range of typical endogenous tissue fluorophores such as collagen and elastin, which excite and emit maximally at approximately 300-500 nm. Therefore, any A647–PLGA fluorescence detected would be NP deposition.

A647–PLGA encapsulated nanoburrs were incubated in the abdominal aorta for 5 min under constant pressure, followed by extensive washing using a syringe-pump to remove nonadsorbed samples (**Figure 6A**). Subsequently, the abdominal aortas were harvested and viewed by whole vessel fluorescent optical imaging (**Figure 6B**). In fluorescent imaging, the detected surface intensity depends on the illumination intensity, which varies according to the field-of-view and wavelength. To eliminate the effect of illumination intensity, images are normalized against a reference illumination image. The resulting “normalized” fluorescent efficiency image is unitless, and the value of each pixel represents the fractional ratio of emitted photons per incident excitation photon. The region-of-interest (ROI) function was used to quantify nanoburr retention (**Figure 7**), and measurements are displayed as average fluorescent efficiency (relative fluorescence units, rfu). The nanoburrs bound to balloon-injured aortas at $1.43 \pm 0.48 \times 10^{-4}$ (rfu), while scrambled-peptide and non-targeted NPs overall bound twofold less at 48% (n=3, P < 0.05) and 47% (n=3, P < 0.05), respectively. To ensure that the nanoburrs would not target intact endothelial layers, they were also incubated with uninjured aortas and bound fourfold less at $3.39 \pm 0.50 \times 10^{-5}$ (rfu) (n=3, P < 0.01) compared to injured vessels. Frozen histological sections were photographed to show nanoburr binding along the arterial cross-section (**Figure 8**).

In Vivo Intraarterial Delivery Studies in Angioplastied Carotid Arteries.

We next examined targeting *in vivo* via IA infusion using a left carotid injury model (**Figure 9A**). The balloon catheter is inserted into the external carotid artery branch between the bifurcation of the common carotid artery and the site of distal ligation and retraction. Samples were delivered at 1 mL/min for 1 min directly into the aortic arch and allowed to circulate for 1 h.

Subsequently, the left and right common carotids attached to the aortic arch were harvested and viewed by whole vessel fluorescent optical imaging (**Figure 9B**). The nanoburrs were injected into angioplastied left carotids through a catheter positioned in the aortic arch inserted from the external carotid artery over the course of 1 min and allowed to circulate for 1 h. Fourfold more nanoburrs [$8.71 \pm 0.38 \times 10^{-6}$ (rfu)] were found in the angioplastied left carotid arteries compared to intact right carotids. Scrambled-peptide and non-targeted NPs were retained in the left carotids at 40% (n=5, P=0.0818) and 53% (n=5, P=0.23716) of nanoburr retention, respectively (**Figure 10**). Representative frozen histological sections show fluorescence along the carotid arteries (**Figure 11**).

In Vivo Intravenous Delivery Studies in Angioplastied Carotid Arteries

The nanoburr system was studied for systemic delivery because repeat dosing may be helpful in the treatment of chronic vascular disease. Using a left carotid injury model, the nanoburrs were given as a 1 mL i.v. dose via tail-vein injection and allowed to circulate for 1 h before animals were sacrificed (**Figure 12A**).

Subsequently, the left and right common carotids attached to the aortic arch were harvested and viewed by whole vessel fluorescent optical imaging (**Figure 12B**). Nanoburr retention was $5.46 \pm 1.02 \times 10^{-6}$ (rfu) in the angioplastied left carotids compared to scrambled-peptide and non-targeted NPs, which were 35% (n=5, P < 0.001) and 64% (n=5, P < 0.01) of nanoburr retention, respectively. The nanoburrs bound to the left carotids twofold over healthy right carotids (P < 0.001) (**Figure 13**). Representative fluorescence images of nanoburr binding are shown in **Figure 14**.

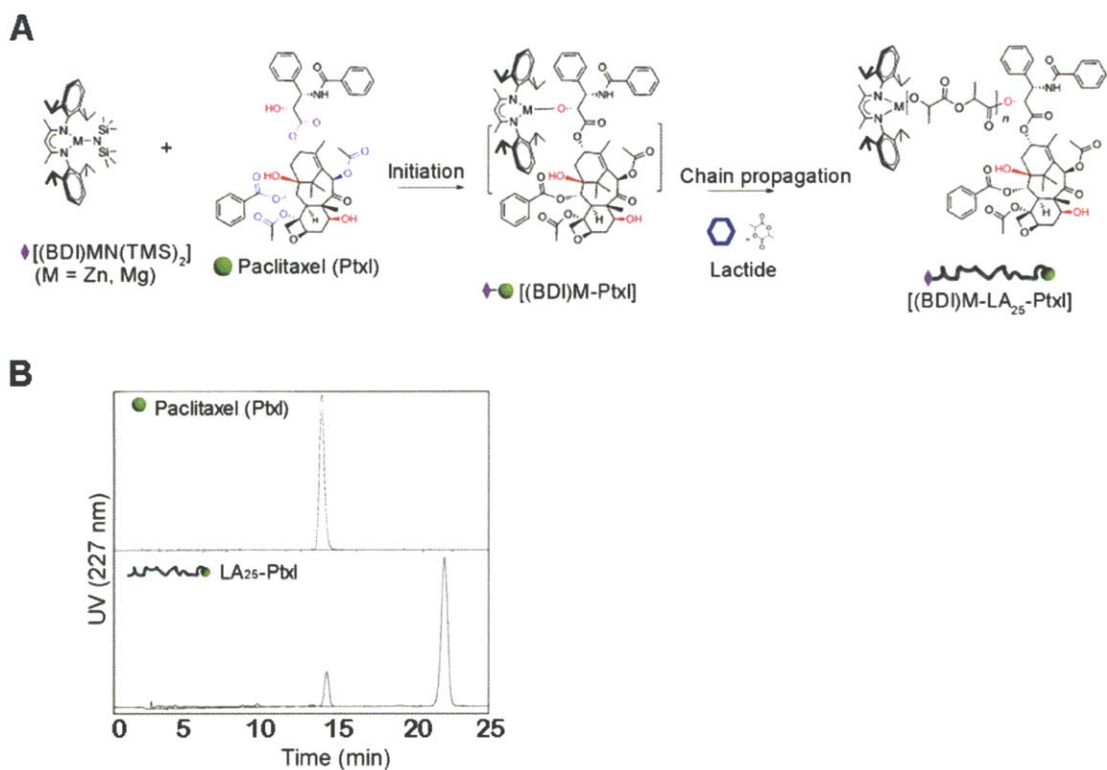


Figure 1. Schematic of Ptxl-PLA biomaterial synthesis.

(A) Ptxl was mixed with equimolar amounts of $[(BDI)ZnN(TMS)_2]$; the $(BDI)Zn$ -Ptxl complex formed *in situ* initiated and completed the polymerization of lactide. Ptxl-PLA₂₅ drug conjugates with approximately 25 D,L-lactide monomer units were synthesized for the nanoburr core. (B) RP-HPLC analysis of Ptxl against Ptxl-PLA₂₅ conjugates.

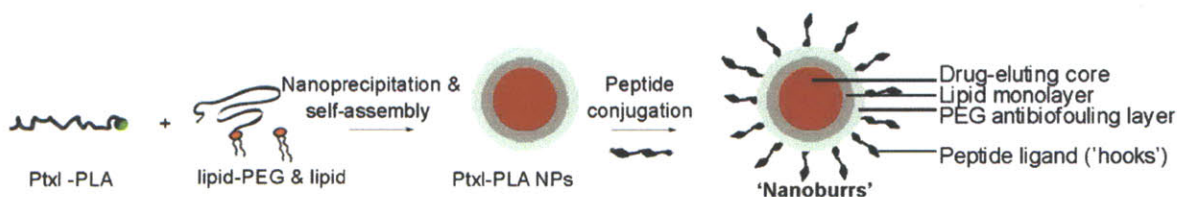


Figure 2. Schematic of nanoburr synthesis by nanoprecipitation and self-assembly.

Ptxl-PLA in acetone was added dropwise to a heated lipid solution, vortexed vigorously, and allowed to self-assemble for 2 h to form NPs. The NPs were peptide-functionalized using maleimide-thiol chemistry. Nanoburrs have a drug-eluting polymeric core, a lipid monolayer, a PEG antibiofouling layer and peptide ligands ('hooks') to adhere to the exposed basement membrane during vascular injury.

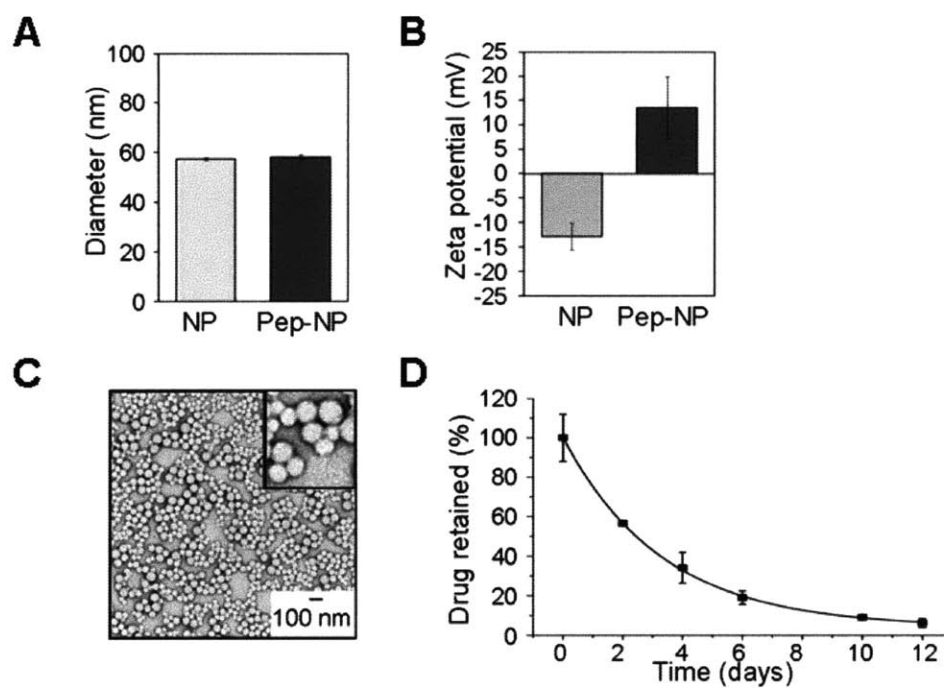


Figure 3. Nanoburr characterization.

(A) Dynamic light scattering measurements before and after peptide conjugation, respectively. (B) Zeta potential measurements before and after peptide conjugation, respectively (mean \pm SD, n=3). (C) TEM image of nanoburrs stained with 3% uranyl acetate. Scale bar, 100 nm. (mean \pm SD, n=3). (G) *In vitro* drug release of Ptx1 from the nanoburr core. Samples at different time points were measured for absorbance at 227 nm (mean \pm SD, n=3).

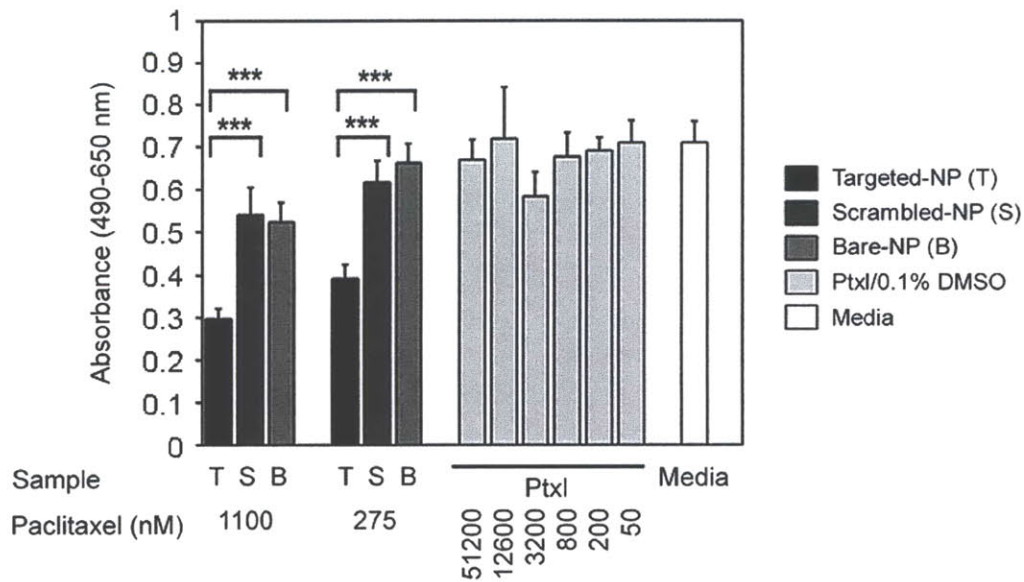


Figure 4. Targeted drug release from nanoburrs.

HaSMC cytotoxicity studies as a function of binding affinity; haSMC on Matrigel-coated plates were incubated with nanoburrs (T), scrambled-NPs (S), non-targeted bare-NPs (B), 4-fold dilutions of Ptxl, and a media-only control for 45 min. Samples were washed two times in complete media and replaced with fresh media for 48 h. Formazan product formation was measured at 490 nm against a reference wavelength of 650 nm (mean \pm SD, n=5). ***, P < 0.001 by one-way ANOVA with Tukey post hoc test.

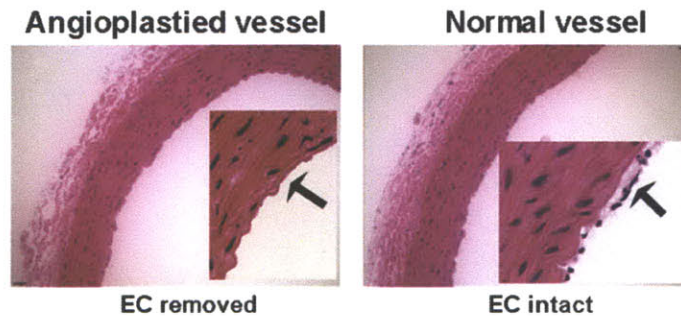


Figure 5. Representative H&E stained cross-sections of balloon-injured and uninjured aortas.

Balloon-injury removes the endothelial cell (EC) monolayer as denoted by arrows in the inset.

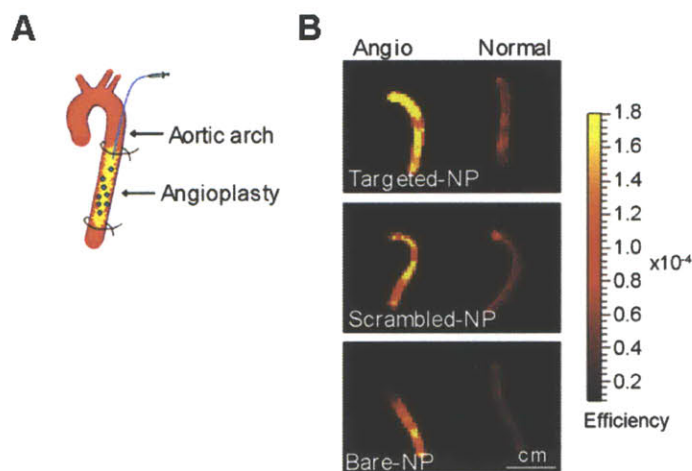


Figure 6. Ex vivo delivery in an abdominal aorta injury model.

(A) Schematic of balloon-injury. The yellow region denotes the angioplasty site. Samples were delivered into the aorta segment for 5 min *in situ*. Nonadsorbed samples were flushed out by saline infusion for 15 min. (B) Fluorescence images overlaid on photographs of balloon-injured aortas incubated with nanoburrs, compared with scrambled peptide and non-targeted NPs.

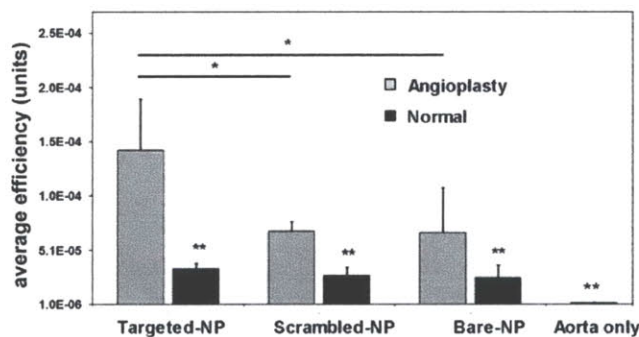


Figure 7. Quantification of nanoburr binding ex vivo to angioplastied aortas.

Aorta sections were analyzed using the region-of-interest (ROI) function of the IVIS Living Image Software. Values are shown here as average fluorescence efficiency (rfu) (mean \pm SD, $n=3$). Aorta-only sections did not have NPs delivered into them. *, $P < 0.05$; **, $P < 0.01$ by one-way ANOVA with Tukey post hoc test.

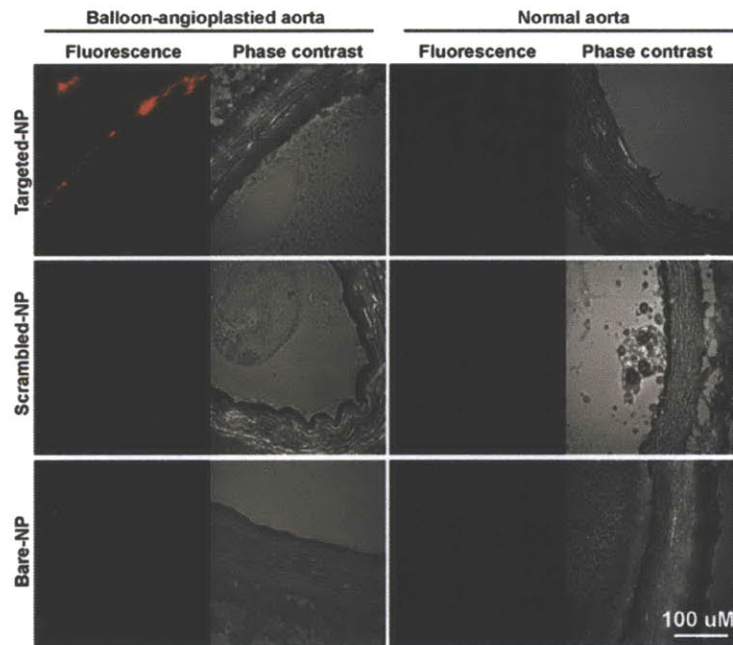


Figure 8. Representative images of nanoburr binding to angioplastied and normal aortas ex vivo.

(Top) Fluorescence and phase contrast images of aortas incubated with nanoburrs. (Middle) Aortas incubated with scrambled-peptide NPs. (Bottom) Aortas incubated with non-targeted NPs. Scale bar, 100 μm . Images were obtained with a DeltaVision deconvolution microscope using the 20x objective.

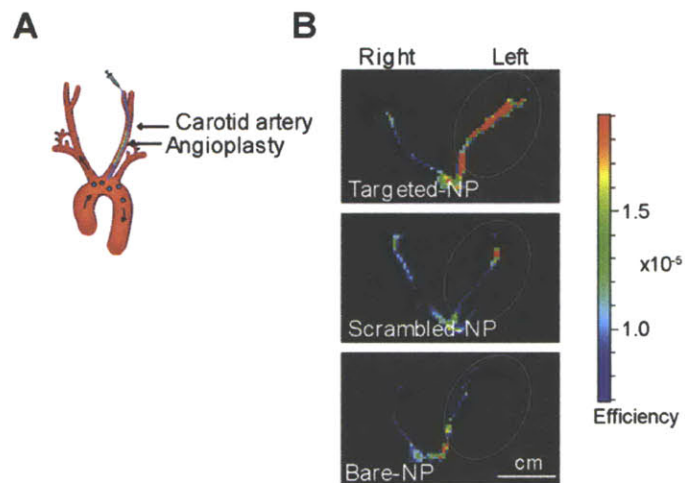


Figure 9. In vivo IA delivery in a carotid injury model.

(A) A catheter was inserted via the external carotid into the common carotid and advanced into the aortic arch. Samples were delivered at 1 mL/min for 1 min and allowed to circulate for 1 h before the animals were sacrificed. (E) Fluorescence images overlaid on photographs of carotid arteries incubated with nanoburrs, compared with scrambled-peptide and non-targeted NPs.

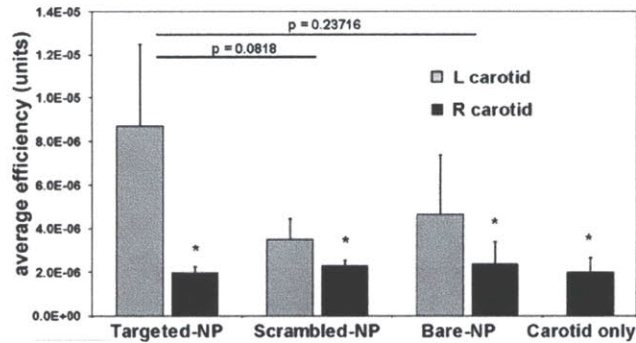


Figure 10. Quantification of nanoburr binding in vivo to angioplastied left common carotids by IA delivery.

Both the left and right common carotid arteries were analyzed using the ROI function of the IVIS Living Image Software. Values are shown here as average fluorescence efficiency (rfu) (mean \pm SD, n=3). Carotid only sections did not have NPs delivered into them. *, P < 0.05 by one-way ANOVA with Tukey post hoc test.

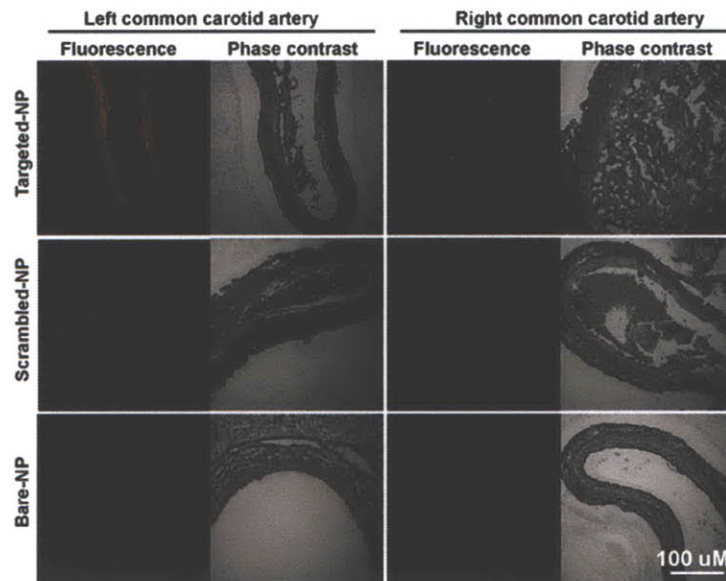


Figure 11. Representative images of nanoburr binding in vivo by IA delivery to angioplastied left common carotids.

(Top) Fluorescence and phase contrast images of carotid arteries incubated with nanoburrs. (Middle) Carotid arteries incubated with scrambled-peptide NPs. (Bottom) Carotid arteries incubated with non-targeted NPs. Scale bar, 100 μ m. Images were obtained with a DeltaVision deconvolution microscope using the 20x objective.

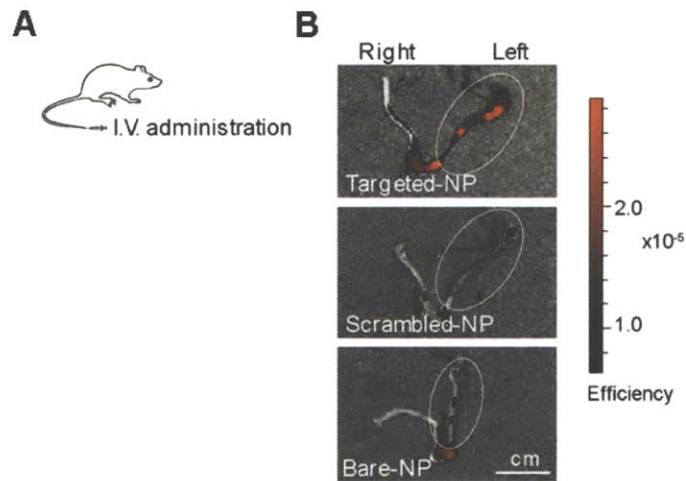


Figure 12. In vivo systemic delivery in a carotid angioplasty model.

(A) Samples were delivered by 1 mL i.v. tail vein injection and allowed to circulate for 1 h before the animals were sacrificed. (B) Fluorescence images overlaid on photographs of carotid arteries incubated with nanoburrs, compared with scrambled-peptide and non-targeted NPs. For imaging, Alexa Fluor 647–PLGA dye conjugates were encapsulated in place of Ptx1–PLA drug conjugates. Scale bar, 1 cm.

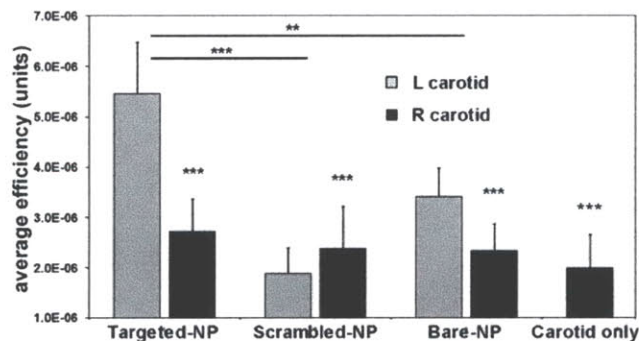


Figure 13. Quantification of nanoburr binding in vivo to angioplastied left common carotids by i.v. delivery.

Both the left and right common carotid arteries were analyzed using the ROI function of the IVIS Living Image Software. Values are shown here as average fluorescence efficiency (rfu) (mean \pm SD, n=5). Carotid-only sections did not have NPs delivered into them. **, P < 0.01; ***, P < 0.001 by one-way ANOVA with Tukey post hoc test.

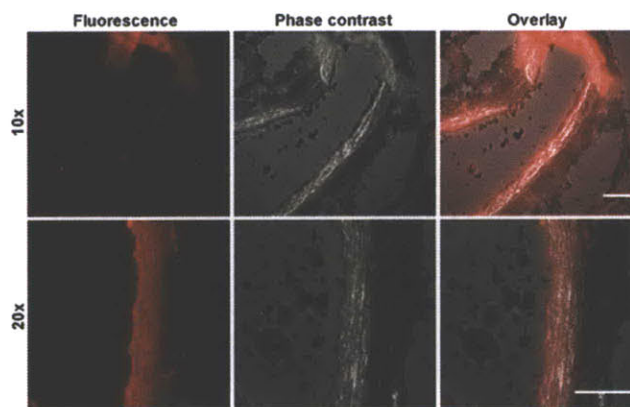


Figure 14. Representative images of nanoburr binding in vivo by i.v. delivery to angioplastied left common carotids.

(Left to Right) Fluorescence, phase contrast and overlay images of angioplastied left common carotid arteries incubated with nanoburrs at 10x and 20x magnification. Scale bar, 100 μm . Images were obtained with a DeltaVision deconvolution microscope using the 10x and 20x objective.

Discussion

In the design of controlled release NPs for vascular targeting, researchers hope to (i) reduce dosing frequency, and (ii) maintain plasma drug levels in the therapeutic window for efficacy. To limit dosing schedules to an acceptable frequency and achieve a therapeutic dose across a predetermined time frame, two parameters of drug loading and drug release must be carefully considered. Increased drug loading into the NP core tends to reduce overall stability, giving an undesired burst release effect and reduced efficacy²³. Larger particles tend to have slower *in vitro* release profiles, but when systemically delivered may be more readily detected and cleared from circulation, resulting in a lack of efficacy²⁴. For vascular targeting, because small particles show improved vessel adhesion and retention^{18,19,25}, integrating slow-eluting conjugates into the nanoburr design allows for (i) improved drug loading, (ii) sub-100-nm NPs for vascular targeting, and (iii) sustained drug release over ten days.

The use of polymers to control drug release is also a significant feature of drug eluting stents (DES)²⁶. Taxus PtxI-eluting moderate release stents (25 wt% PtxI to polymer, 171 µg PtxI) release an initial bolus of PtxI in 48 h, followed by low-level release over 10 days. Taxus slow release stents (8.8 wt% PtxI to polymer, 85 µg PtxI) release drugs over 30 days²⁷. In these stents however, only less than ~10% of the PtxI fraction is ever released. Hence, the drug release profile from the nanoburrs in this study may be relevant for the treatment of angioplastied vessels. Ideally, the NPs should have an approximately one-week drug release profile at sites of vascular injury during the initial period of proliferation and inflammation. With the nanoburrs, drug elution rates may be further controlled by varying lactide/PtxI ratios during ring-opening polymerization, resulting in different PLA chain lengths attached to the PtxI drug⁸.

This study utilized a peptide-targeted NP delivery system against resident proteins of the basement membrane. The potential applications of related systems are diverse, ranging from therapeutic to diagnostic applications in oncologic, cardiovascular and regenerative diseases.

The targeting of basement membrane proteins may be used to modulate key integrin–matrix interactions during angiogenesis. Anti-angiogenic therapy is currently one of most active fields in cancer research, with strategies aimed at inhibiting tumor vascularization either by upregulation of endogenous inhibitors or downregulation of angiogenic signals from factors such as VEGF. Integrin ligands play key roles in endothelial cell survival, migration and new vessel differentiation and reorganization. Novel anti-angiogenic approaches include the use of therapeutic blocking ligands to disrupt crucial integrin-matrix interactions and generate locally nonpermissive basement membranes²⁸. These compounds halted tumor growth in murine models and are now in clinical trials²⁸. Phage display was used to find peptides that target MMP2-processed collagen IV and these peptides subsequently blocked angiogenesis *in vivo*²⁹. Researchers have fluorescently imaged colorectal carcinomas in mice using multivalent ‘trimerbodies’ (scFv fragments connected to the N-terminal trimerization subdomain of the collagen XVIII NC1 domain) against the human carcinoembryonic antigen (CEA), an angiogenesis-associated epitope of laminin^{30,31}. Future applications may include targeted therapeutic delivery to functional laminin domains, as laminin is a resident basement membrane protein with a well-studied role in tube formation.

The targeting of matrix proteins may also be useful for the imaging of fibrotic disease. Fibrosis is a common outcome in chronic diseases due to a reparative process to injury. The formation or development of excess fibrous connective scar tissue (largely type I collagen) eradicates the architecture of the underlying tissue and may result in organ dysfunction. As described in **Chapter 4**, the thickness of fibrotic caps in atherosclerotic plaques has been shown to be an indicator of lesion rupture and thrombosis. In mouse models of myocardial infarction, MR imaging of the contrast agent delineated the infarct zone where necrotic myocytes are replaced by a fibrotic myocardial scar^{32,33}.

Finally, matrix proteins can be targeted to convert the matrix from a barrier into a reservoir. Researchers have targeted collagen II α 1³⁴ of dense, avascular intra-articular cartilage tissue to resist the rapid clearance of NPs from cartilage. Future applications using targeted polymeric NPs may include therapeutic delivery for the treatment of degenerative joint disease and osteoarthritis. In contrast with local avascular delivery to the knee joints, our study targets vascular basement membranes by systemic delivery. Conceptually however, in both cases the matrix no longer serves as a barrier but instead provides a drug reservoir. Through this drug depot, we hope to deliver anti-proliferative medicines that distribute into the inner layers of the injured vessel wall.

Our binding studies to sites of injured vasculature altogether show the successful targeting and retention of nanoburrs to injured carotid arteries *in vivo* and abdominal aortas *ex vivo*. In **Chapter 7**, we explore whether the localization of anti-proliferative therapies through collagen IV-targeted NPs corresponds to improved treatment outcomes.

References

1. Gref, R., *et al.* Biodegradable long-circulating polymeric nanospheres. *Science* **263**, 1600-1603 (1994).
2. Zhang, L., *et al.* Nanoparticles in medicine: therapeutic applications and developments. *Clin Pharmacol Ther* **83**, 761-769 (2008).
3. Kim, T.Y., *et al.* Phase I and pharmacokinetic study of Genexol-PM, a cremophor-free, polymeric micelle-formulated paclitaxel, in patients with advanced malignancies. *Clin Cancer Res* **10**, 3708-3716 (2004).
4. Davis, M.E., Chen, Z.G. & Shin, D.M. Nanoparticle therapeutics: an emerging treatment modality for cancer. *Nat Rev Drug Discov* **7**, 771-782 (2008).
5. Nel, A.E., *et al.* Understanding biophysicochemical interactions at the nano-bio interface. *Nat Mater* **8**, 543-557 (2009).
6. Zhang, L., *et al.* Self-Assembled Lipid-Polymer Hybrid Nanoparticles: A Robust Drug Delivery Platform. *ACS Nano* **2**, 1696-1702 (2008).
7. Chan, J.M., *et al.* PLGA-lecithin-PEG core-shell nanoparticles for controlled drug delivery. *Biomaterials* **30**, 1627-1634 (2009).
8. Tong, R. & Cheng, J. Paclitaxel-initiated, controlled polymerization of lactide for the formulation of polymeric nanoparticulate delivery vehicles. *Angew Chem Int Ed Engl* **47**, 4830-4834 (2008).
9. Chamberlain, B.M., *et al.* Polymerization of lactide with zinc and magnesium beta-diiminate complexes: stereocontrol and mechanism. *J Am Chem Soc* **123**, 3229-3238 (2001).
10. Dechy-Cabaret, O., Martin-Vaca, B. & Bourissou, D. Controlled ring-opening polymerization of lactide and glycolide. *Chem Rev* **104**, 6147-6176 (2004).
11. Peer, D., *et al.* Nanocarriers as an emerging platform for cancer therapy. *Nat Nanotechnol* **2**, 751-760 (2007).
12. Langer, R. Drug delivery and targeting. *Nature* **392**, 5-10 (1998).
13. Hudson, B.G., Reeders, S.T. & Tryggvason, K. Type IV collagen: structure, gene organization, and role in human diseases. Molecular basis of Goodpasture and Alport syndromes and diffuse leiomyomatosis. *J Biol Chem* **268**, 26033-26036 (1993).
14. Kalluri, R. Basement membranes: structure, assembly and role in tumour angiogenesis. *Nat Rev Cancer* **3**, 422-433 (2003).
15. Kleinman, H.K., *et al.* Isolation and characterization of type IV procollagen, laminin, and heparan sulfate proteoglycan from the EHS sarcoma. *Biochemistry* **21**, 6188-6193 (1982).
16. Folkman, J. Angiogenesis: an organizing principle for drug discovery? *Nat Rev Drug Discov* **6**, 273-286 (2007).
17. Ross, R. Atherosclerosis--an inflammatory disease. *N Engl J Med* **340**, 115-126 (1999).
18. Westedt, U., *et al.* Deposition of nanoparticles in the arterial vessel by porous balloon catheters: localization by confocal laser scanning microscopy and transmission electron microscopy. *AAPS PharmSci* **4**, E41 (2002).
19. Fishbein, I., *et al.* Formulation and delivery mode affect disposition and activity of tyrphostin-loaded nanoparticles in the rat carotid model. *Arterioscler Thromb Vasc Biol* **21**, 1434-1439 (2001).

20. Decuzzi, P., Pasqualini, R., Arap, W. & Ferrari, M. Intravascular delivery of particulate systems: does geometry really matter? *Pharm Res* **26**, 235-243 (2009).
21. Chan, J.M., *et al.* Spatiotemporal controlled delivery of nanoparticles to injured vasculature. *Proc Natl Acad Sci U S A* **107**, 2213-2218 (2010).
22. Libby, P. Inflammation in atherosclerosis. *Nature* **420**, 868-874 (2002).
23. Soppimath, K.S., Aminabhavi, T.M., Kulkarni, A.R. & Rudzinski, W.E. Biodegradable polymeric nanoparticles as drug delivery devices. *J Control Release* **70**, 1-20 (2001).
24. Alexis, F., Pridgen, E., Molnar, L.K. & Farokhzad, O.C. Factors affecting the clearance and biodistribution of polymeric nanoparticles. *Mol Pharm* **5**, 505-515 (2008).
25. Decuzzi, P. & Ferrari, M. The adhesive strength of non-spherical particles mediated by specific interactions. *Biomaterials* **27**, 5307-5314 (2006).
26. Grube, E., *et al.* Evaluation of a new polymer-coated paclitaxel-eluting stent for treatment of de novo lesions: six-month clinical and angiographic follow-up results of the APPLAUSE trial. *J Invasive Cardiol* **18**, 194-198 (2006).
27. Ranade, S.V., *et al.* Physical characterization of controlled release of paclitaxel from the TAXUS Express2 drug-eluting stent. *J Biomed Mater Res A* **71**, 625-634 (2004).
28. Sanz, L. & Alvarez-Vallina, L. The extracellular matrix: a new turn-of-the-screw for anti-angiogenic strategies. *Trends Mol Med* **9**, 256-262 (2003).
29. Mueller, J., Gaertner, F.C., Blechert, B., Janssen, K.P. & Essler, M. Targeting of tumor blood vessels: a phage-displayed tumor-homing peptide specifically binds to matrix metalloproteinase-2-processed collagen IV and blocks angiogenesis in vivo. *Mol Cancer Res* **7**, 1078-1085 (2009).
30. Cuesta, A.M., *et al.* In vivo tumor targeting and imaging with engineered trivalent antibody fragments containing collagen-derived sequences. *PLoS One* **4**, e5381 (2009).
31. Sanz, L., Kristensen, P., Russell, S.J., Ramirez Garcia, J.R. & Alvarez-Vallina, L. Generation and characterization of recombinant human antibodies specific for native laminin epitopes: potential application in cancer therapy. *Cancer Immunol Immunother* **50**, 557-565 (2001).
32. Caravan, P., *et al.* Collagen-targeted MRI contrast agent for molecular imaging of fibrosis. *Angew Chem Int Ed Engl* **46**, 8171-8173 (2007).
33. Spuentrup, E., *et al.* Molecular magnetic resonance imaging of myocardial perfusion with EP-3600, a collagen-specific contrast agent: initial feasibility study in a swine model. *Circulation* **119**, 1768-1775 (2009).
34. Rothenfluh, D.A., Bermudez, H., O'Neil, C.P. & Hubbell, J.A. Biofunctional polymer nanoparticles for intra-articular targeting and retention in cartilage. *Nat Mater* **7**, 248-254 (2008).

Chapter 7. Targeted Nanoparticles for Anti-Restenotic Drug Delivery to Injured Vasculature.

Abstract

Percutaneous angioplasty, a procedure to revascularize lesions, provides a short-term solution to coronary artery disease (CAD). The balloon device induces extensive local injury, endothelial denudation and exposure of the underlying basal lamina. Collagen IV, the primary component of the basement membrane, becomes abundantly visible to circulation. This study aims to determine if the localization of anti-proliferative therapies through collagen IV-targeted NPs corresponds to reduced neointima formation in balloon-injured rat carotid arteries. Using ~55 nm biodegradable lipid-polymeric hybrid NPs and phage-displayed peptides with affinity for collagen IV, we loaded the NPs with paclitaxel for targeted delivery. *In vivo* efficacy studies where targeted-NPs were given by systemic delivery on Day 1 and 6 of surgery resulted in lower neointimal/media (N/M) scores at two weeks compared to FDA-approved Taxol® and injury-only sham groups (1 mg/kg paclitaxel dose: $N/M_{\text{Sham}}=1.249 \pm 0.046$ versus $N/M_{\text{Taxol}}=0.837 \pm 0.087$, $N/M_{\text{NP}}=0.749 \pm 0.136$ and $N/M_{\text{Pep-NP}}=0.662 \pm 0.169$, all $P < 0.01$ versus injury-only group, mean \pm SEM, $n=5$). At low paclitaxel doses of 0.3 mg/kg, targeted-NP groups showed better lumen patency compared to non-targeted NP groups ($N/M_{\text{NP}}=1.063 \pm 0.097$ versus $N/M_{\text{Pep-NP}}=0.744 \pm 0.13$, $P < 0.08$, mean \pm SEM, $n=5$). Our findings suggest that the collagen IV-targeted NPs may potentially be used as a systemically delivered treatment in CAD.

Introduction

Cardiovascular disease constitutes the leading cause of illness and death worldwide of which atherosclerosis is a dominant contributor¹. In the United States, approximately 500,000 deaths occur annually due to atherosclerotic cardiovascular disease. The arterial wall thickening and lumen narrowing associated with the growing atherosclerotic plaque gradually results in insufficient blood supply to organs such as the heart and brain. In severe circumstances, it may abruptly rupture causing a blood clot in the vessel and subsequent thrombosis, heart attack or stroke. In clinical cardiology, percutaneous coronary interventions (PCI) are widely employed for the revascularization of stenotic coronary arteries as a complementary alternative to medical therapy and coronary artery bypass graft surgery (CABG). During PCI, intraluminal balloon inflation may result in various outcomes such as acute elastic recoil of the damaged wall within one hour of angioplasty, followed by slower unfavorable vascular remodeling and neointimal SMC formation within one to six months, eventually leading up to restenosis, the cell-mediated narrowing of the vessels, in 30-50% of patients^{2,3}. Bare metal stents (BMS) were originally developed to improve vessel patency and reduce abrupt closure, but they likely stimulate SMC proliferation leading to a 15-25% risk of in-stent stenosis⁴ (**Figure 1**).

As a result, drug eluting stents (DES) such as the Cypher sirolimus-eluting (Cordis Corporation), Taxus paclitaxel-eluting (Boston Scientific) and Xience V everolimus-eluting (Abbott Laboratories) stents were developed to deliver therapeutic agents directly into the site of vascular injury^{4,5}. DES combine a drug delivery system via polymer-coated matrices and a mechanical scaffold to maintain vascular patency in atherosclerotic lesions. Cypher stents elute sirolimus which induces G₁ cell cycle inhibition, while Taxus stents release paclitaxel (Ptxl) which causes M-phase arrest. Since their introduction, DES have become the treatment of choice and currently more than six million people worldwide have a DES fitted^{4,5}. DES are generally superior to BMS with regards to Major Adverse Cardiac Events (MACE), generally defined as death, myocardial infarction, or the need for a repeat revascularization procedure. Although the use of DES significantly reduces the need for subsequent revascularization, it is associated with an increased incidence of very late stent thrombosis (VLST) beyond the one year mark⁶. The non-biodegradable polymers used as drug-eluting matrices may also result in delayed arterial

healing^{7,8}, as evidenced by persistent fibrin deposits, incomplete endothelialization and hypersensitivity reactions (such as eosinophilic infiltrates)^{9,10}. This delayed healing is the primary substrate underlying all cases of late DES thrombosis at autopsy⁸. Hence, DES implantation is associated with a dual-antiplatelet regimen of aspirin and clopidogrel to prevent thrombus formation^{11,12}. Furthermore, small-vessel (< 2.5 mm) arteries, large-vessel (> 3.5 mm) arteries, very long lesions (> 33 mm) and bifurcation lesions are not amenable to stenting. Together with premature antiplatelet therapy discontinuation, renal failure, diabetes and low ejection fraction, all these ‘off-label’ uses were identified as predictors of VLST¹²⁻¹⁴. Despite the risks involved and the current unavailability of long-term safety results, sirolimus-eluting DES remained superior to BMS at five-years after implantation¹⁵.

It has become increasingly attractive to find complementary options to DES-based drug delivery from a nanotechnology standpoint^{16,17}. Sub-100 nm targeted NPs are virtually free from fixed constraints, deliver drugs in a controlled manner, and are biodegradable and biocompatible. In this study, the peptide-targeted NP system from **Chapter 6**¹⁸ is delivered as a systemic, intravenous infusion after angioplasty. We hypothesized that the improved localization of anti-proliferative therapies to angioplastied vasculature may contribute to improved treatment outcomes such as reduced SMC proliferation and improved vessel patency. We compare our formulations against injury-only sham controls and FDA-approved Taxol, a Cremophor-EL (polyethoxylated castor oil) micelle formulation of Ptxl. *In vivo* efficacy studies where targeted-NPs were given as i.v. doses on Day 1 and 6 of surgery resulted in lower neointimal/media (N/M) scores at two weeks compared to Taxol and injury-only groups.

Methods

Materials.

All peptides were custom synthesized by Genscript (Piscataway, NJ) with C-terminal amidation and purified by RP-HPLC to >95% purity by mass spectral analysis. Peptides were synthesized with a linker sequence (GGGC) at the C-terminus for thiomaleimide coupling. Soybean lecithin consisting of 90–95% soybean phosphatidylcholine was obtained from MP Biomedicals (Solon, OH). DSPE-PEG2000 and DSPE-PEG2000-maleimide were obtained from Avanti (Alabaster, AL). PLGA with 50:50 monomer ratio, ester-terminated and 0.72–0.92 dl/g inherent viscosity was purchased from Durect Corporation (Pelham, AL). Paclitaxel (Ptxl) and all other materials were purchased from Sigma-Aldrich unless otherwise noted.

Synthesis and Characterization of Targeted NPs.

DSPE-PEG-peptide triblocks were synthesized in 4% EtOH at a peptide/DSPE-PEG 1.25/1 molar ratio for 4 h with gentle rocking. The peptides were previously reduced for 30 min using Bond-breaker TCEP solution, Neutral pH (Thermo Scientific) in pH 7.2 PBS buffer with 5 mM EDTA at a 1/1 disulfide bond/TCEP molar ratio. Free peptides were removed by dialysis using 3,500 Da MWCO Spectrapor membranes (Spectrum Laboratories, Houston, TX) for 24 h with two water changes. A 3 mL DSPE-PEG/lecithin mixture in 4% EtOH containing 1.5 mg DSPE-PEG-peptide/DSPE-PEG (1/9 molar ratio) and 0.75 mg lecithin was heated for 3 min above the lipid phase transition temperature to 68 °C under gentle stirring. 9 mg of PLGA mixed with 0.45 mg of paclitaxel in 3 mL acetone (3 mg/mL polymer, 5 wt% Ptxl initial load) was added dropwise at 3 mL/min. The solution was vortexed vigorously for 3 min followed by self-assembly under gentle stirring for 2 h at RT. The NPs were washed three times using a 30 kDa MWCO Amicon Ultra-4 centrifugal filter (Millipore). NPs were resuspended in saline and sterile-filtered using 25 mm Acrodisc syringe filters with 0.8 µm Supor membranes (Pall Corporation, Port Washington, NY) before HPLC drug quantification and i.v. injection into animals. For scale-up, multiple vials of NPs were made with concentrations and volumes kept constant to maintain small NP diameters.

Preparation of Taxol Formulations.

Taxol formulations were prepared according to the manufacturer's instructions. Briefly, Ptxl was dissolved under gentle stirring to 6 mg/mL at a 1/1 ratio in Cremophor-EL and anhydrous ethanol, 200 proof. This formulation was then diluted 1:10 in saline for a final dosing solution containing 0.6 mg/mL of Ptxl. The solution was sterile-filtered using 25 mm Acrodisc syringe filters with 0.8 µm Supor membranes (Pall Corporation, Port Washington, NY). The drug loading in all Taxol and NP batches were quantified by RP-HPLC against a standard curve of known Ptxl concentration before i.v. administration to animals. All discussions of drug dosing in units of mg/kg relate to the active drug composition.

Animals.

Sprague-Dawley rats weighing approximately 400-500 g were obtained from Charles River Laboratories and kept on standard rodent chow and water *ad libitum* peri-operatively. Male rats are preferred for surgery because of their larger sizes. All animal procedures were conducted by a certified contract research organization using protocols consistent with local, state, and federal regulations as applicable and approved by the Institutional Animal Care and Use Committee.

Rat Carotid Model and In Vivo Proliferation Studies.

Rat carotid injury was performed as described by Tulis, D.A.¹⁹. In this study, animals were given aspirin (20 mg/kg) by oral gavage on Day -1 of surgery. On Day 1 of surgery, animals were given heparin (250 IU/kg) by i.v. injection immediately before surgery. Animals were anesthetized intramuscularly with ketamine (60 mg/kg)/xylazine (10 mg/kg) and given buprenorphine as an analgesic. The arteriotomy site for insertion of the balloon catheter is on the external carotid artery branch between the bifurcation of the common carotid artery and the site of distal ligation and retraction. The left common carotid artery was denuded of endothelium by intraluminal passage of a Fogarty arterial embolectomy 2F balloon catheter (Model 120602F; Edwards Lifesciences) introduced through the external carotid artery in a rotating fashion. Lidocaine hydrochloride was gently swabbed onto the exposed carotids. Following permanent ligation of the external carotid artery, the skin incision was closed with sutures and swabbed with

bactericide gel around the sutures to reduce the likelihood of infection. Animals were given more analgesic and kept warm on 37 °C heating pads for ~1 h after surgery. During this recovery period, samples (n=5 per dosing group) were i.v. injected into the tail-vein and animals were re-dosed on Day 6 after surgery. The surgical procedure and sample dosing did not cause mortality or any apparent morbidity. Animals were sacrificed on Day 14 by CO₂ inhalation. Both the left and right carotids and vital organs were harvested during necropsy.

Morphometric Analysis.

Tissues were fixed in 4% paraformaldehyde/4% sucrose/saline overnight at 4 °C. Tissues were paraffin-embedded and cryosectioned to give nine representative cross-sections across the artery length and H&E stained (AML Laboratories, Rosedale, MD). Images were obtained with a Zeiss microscope using the bright field setting at 5x objective. Cross-sections were analyzed using ImageJ (<http://rsb.info.nih.gov/ij/>) computerized morphometric analysis software from the NIH, by an investigator blinded to the experimental group. The degree of neointimal thickening was expressed as the ratio between the neointimal area to the medial area (N/M). The cross-section with the greatest luminal narrowing results in the highest N/M ratio and this value is assigned to the artery.

Immunohistochemistry.

Paraffin-embedded cryosectioned slides were deparaffinized and incubated with 1% H₂O₂ in methanol for 10 min to block endogenous peroxidase, followed by 10% horse serum in PBS for 20 min to block non-specific antibody binding. Primary antibodies for rat α -SMC (DAKO, Carpinteria, CA) were applied for 1 hour at 37 °C. Sections were washed with PBS and incubated with biotinylated secondary antibodies (horse anti-mouse IgG, Vector Laboratory, Burlingame, CA) and avidin-biotin-peroxidase complexes (ABC Elite kit, Vector Laboratory) for 30 min each. Color development was achieved by a 5 min exposure to 3,3'-diaminobenzidine tetrahydrochloride (DAB peroxidase substrate). Slides were lightly counterstained with Gill No. 3 hematoxylin. Positive staining was evaluated using a Zeiss microscope under a bright field setting at 5x objective.

Statistics.

All error bars represent mean \pm SEM. Comparisons of histological findings between control and treatment groups were made using one-way ANOVA with Tukey post hoc tests. Differences were termed statistically significant at $P < 0.05$.

Results

Rat Carotid Injury Model.

The rat carotid injury model was first designed by Clowes, A.W. *et al.* in 1983^{20,21} to investigate the mechanism of stenosis from cellular proliferation after arterial injury (**Figure 2**). In these studies, acute thrombosis is prevented by anti-platelet or anti-thrombotic therapies such as aspirin and/or a small i.v. bolus of heparin.

This injury model involves isolating a carotid arterial segment and creating an arteriotomy incision in the external carotid branch through which the balloon catheter is inserted and advanced into the common carotid artery (**Figure 2A**). Repeated inflation and withdrawal of the catheter induces endothelial cell loss and intimal injury. Subsequently, the catheter is removed and the suture is closed at the arteriotomy site before blood flow is resumed (**Figure 2B**). **Figure 2C** gives a close-up of the surgery and shows the arteriotomy site at the left external carotid artery. **Figure 2D** gives a simplified diagram of the surgical procedure and rat carotid artery vascular anatomy along with sites of placement of arterial clamps, sutures and ligations.

Histological and morphometric analyses with this model can be employed for long-term quantification of neointima development and vessel wall restructuring. Representative images of carotid artery cross-sections taken from the same animal show the result of arterial balloon-injury when compared to non-injured arteries. In the left column of **Figure 3**, left carotids that received the balloon-injury showed extensive neointimal formation and lumen occlusion at two weeks in both H&E and VvG stained sections. In the right column however, non-injured right carotids remained healthy and intact, with no neointimal formation and lumen occlusion observed at two weeks.

Characterization of NP Treatment Groups.

NPs were made in ~1 g batches (based on PLGA weight). The NPs were found to be 55.1 ± 0.4 nm (polydispersity=0.075, n=3) in one representative batch after sterile filtration, and this value was found to vary batch-to-batch by only ± 5 nm. NP batches that were functionalized with peptides did not show any significant size increase beyond 5 nm.

To determine the final drug loading based on a 5 wt% initial drug/polymer input, a batch of NPs were lyophilized to get the final polymer weight (80% of final weight, other 20% is lipids and PEG). Samples were resuspended in 1/1 acetonitrile/water for measurements of drug content. The final drug load was 1.04 wt% (n=3), giving a 21.35% overall encapsulation efficiency of Ptxl. The initial drug input was kept low to prevent a drug release burst observed with higher drug loadings. Although we used Ptxl-PLA drug conjugates in **Chapter 6**, here we used free Ptxl to compare our NPs against Taxol micellar formulations. Any modification of the drug through amine side-chain modification and ring-opening polymerization would change the active drug composition and render direct comparisons with Taxol difficult.

Morphometric Analyses of Treatment Groups.

On Day 1 of surgery, the mean weights of animals were approximately 400-500 g. During the study, the mean body weight of the animals in all treatment groups increased and was similar when the study was concluded. Treatment groups (n=5) were Taxol, hybrid NPs and peptide-functionalized NPs, versus sham injury-only groups. Samples were i.v. injected as a bolus with Ptxl doses set at 0.3 mg/kg and 1 mg/kg. Here, all discussions of drug delivery relate to the active drug composition and not the material composition.

Repeat dosing may be important in the treatment of vascular disease, since atherosclerosis is a chronic disease that needs long-term care. Furthermore, systemic dosing is non-invasive and does not require additional surgical procedures. Therefore, all our treatment groups were given as doses on Day 1 and Day 6, midway to the conclusion of the study.

The studies were terminated at 14 days after angioplasty. Animals were sacrificed and both carotids were harvested for inspection. Using the ImageJ morphometric analysis software (NIH), cross-sections of arteries were analyzed by an investigator blinded to the type of

experimental group. The degree of neointimal thickening was expressed as the ratio between the neointimal area to the medial area (N/M). The cross-section with the greatest luminal narrowing results in the highest N/M ratio and this value is assigned to the artery (**Figure 4A**). Using an injury-only group carotid artery cross-section as an example (**Figure 4B**), three rings were made to surround the (i) tunica media (at the external elastic lamina, EEL), (ii) tunica intima (at the internal elastic lamina, IEL) and (iii) lumen. Next, the areas denoted by these three rings were noted. The medial area (M) is calculated from the area bordered by the EEL and the IEL, i.e. area (i) subtract area (ii). The neointimal area (N) is calculated from the area bordered by the IEL and the lumen, i.e. area (ii) subtract area (iii). From there, N/M ratios can be derived and this gives a unitless ratio (**Figure 4C**).

N/M measurements taken from the site of greatest luminal narrowing per artery showed that sham injury-only saline groups had N/M scores of $N/M_{\text{Sham}}=1.249 \pm 0.046$ versus 1 mg/kg treatment groups of $N/M_{\text{Taxol}}=0.837 \pm 0.087$, $N/M_{\text{NP}}=0.749 \pm 0.136$ and $N/M_{\text{Pep-NP}}=0.662 \pm 0.169$ (all $P < 0.01$ vs. injury-only group, mean \pm SEM, $n=5$). When doses were lowered three-fold to 0.3 mg/kg, average N/M ratios per treatment group of $N/M_{\text{Taxol}}=0.937 \pm 0.126$ ($P < 0.05$ mean \pm SEM, $n=5$), $N/M_{\text{NP}}=1.063 \pm 0.097$ ($P > 0.05$ mean \pm SEM, $n=5$) and $N/M_{\text{Pep-NP}}=0.744 \pm 0.129$ ($P < 0.01$ mean \pm SEM, $n=5$) were obtained. This suggests that even at low therapeutic doses, the peptide-functionalized hybrid NPs were still able to localize and treat injured vasculature. In **Figure 6**, representative H&E cross-sections are taken from each treatment group. In **Figure 7**, representative α -smooth muscle cell actin (α -SMA) immunostained cross-sections were taken from each treatment group. Both **Figure 6** and **Figure 7** suggest qualitative differences in neointimal proliferation when compared to saline groups, and also a dose-response when higher or lower doses of Ptx1 were given.

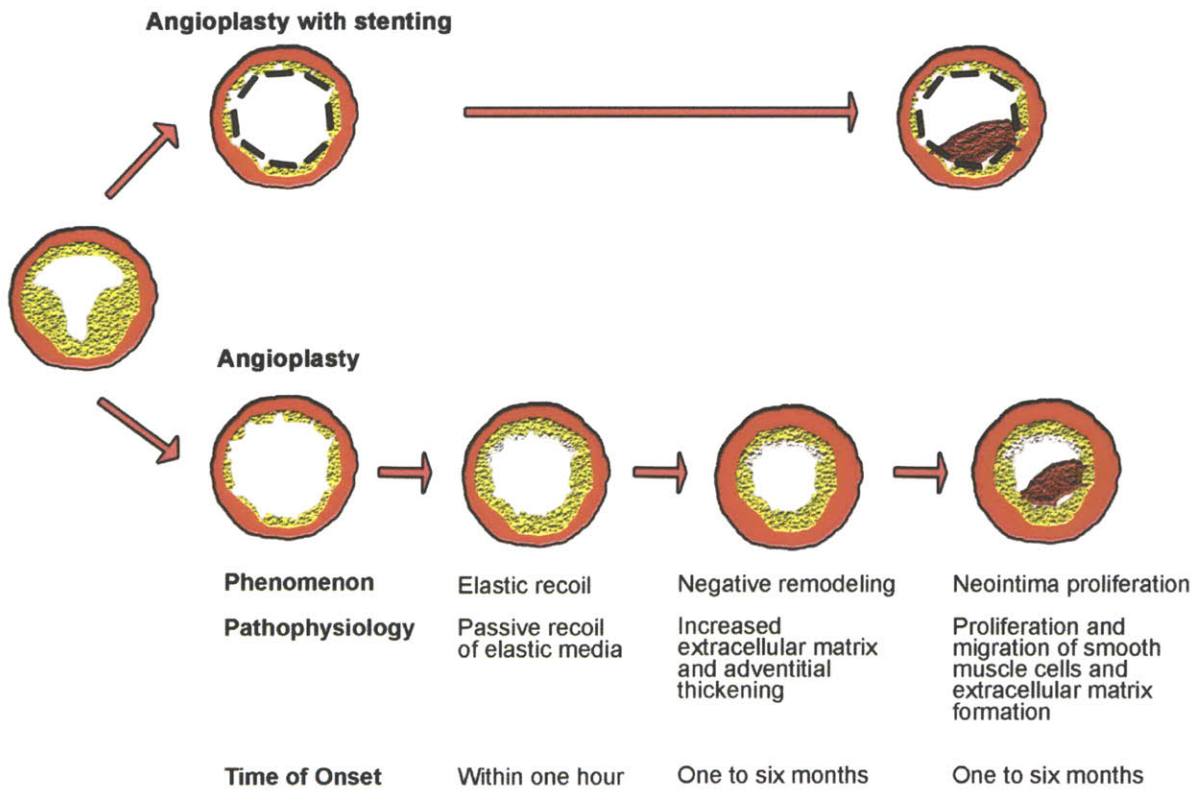


Figure 1. Schematic of events after angioplasty and stenting.

Revascularization of a stenotic atherosclerotic lesion results in acute elastic recoil of the damaged wall within one hour of angioplasty, followed by a slower unfavorable negative remodeling within one to six months. These two unfavorable outcomes can be prevented by bare metal stenting (BMS). In stented and non-stented arteries, neointimal proliferation is observed after one to six months, eventually leading to restenosis in 30-50% of patients. This risk is reduced to 15-25% of patients with BMS.

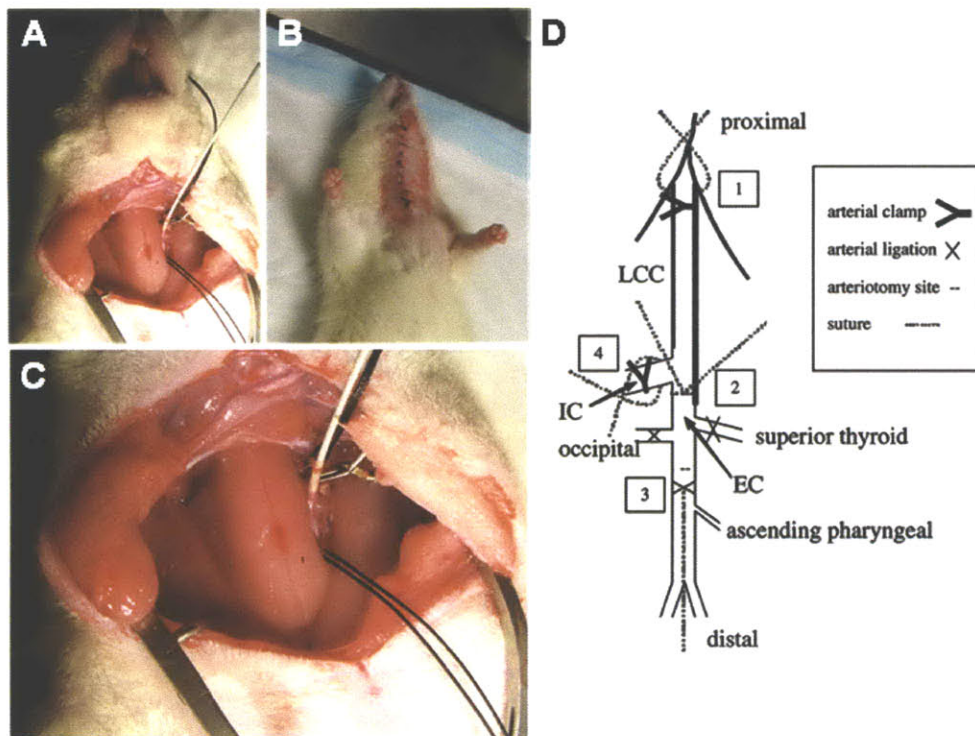


Figure 2. A rat carotid model of vascular injury.

(A) Photograph of carotid surgery. The balloon catheter is inserted into the external carotid artery branch between the bifurcation of the common carotid artery and the site of distal ligation and retraction. (B) Photograph of skin incision and post-procedure sutures. (C) Close-up of carotid surgery. (D) Simplified diagram of the rat carotid artery vascular anatomy along with sites of placement of arterial clamps, sutures and ligations. IC, internal carotid; EC, external carotid; LCC, left common carotid. This figure (Figure 3) was reproduced with kind permission from Springer Science + Business Media, License: 2364821090061. Tulis, D.A.. Rat Carotid Artery Balloon Injury Model. *Methods in Molecular Medicine, Vascular Biology Protocols*. (2007) **139**, 1-30. Springer Science + Business Media © 2007.

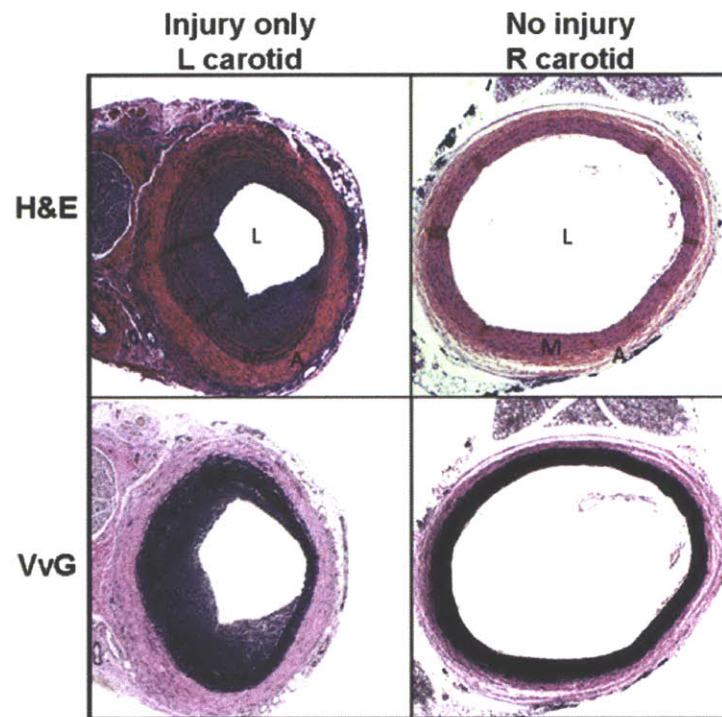


Figure 3. Representative carotid arteries with and without injury.

Injury only left carotids versus uninjured right carotids. Representative H&E and VvG stained sections. Images were obtained with a Zeiss microscope using the 5x objective. L, lumen; N, neointima; M, media; A, adventitia.

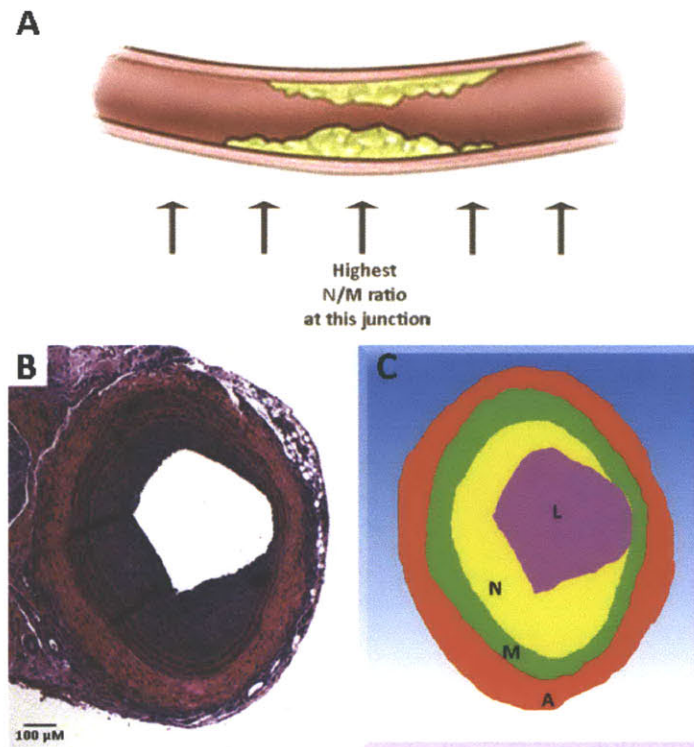


Figure 4. Determination of N/M ratios of carotid samples.

(A) Nine arterial cross-sections were analyzed across the length of the artery (denoted by arrows). The section with the highest N/M ratio value gives the site of greatest luminal narrowing and that numerical value is assigned to each artery. (B) Representative H&E-stained artery cross-section. (C) N/M ratio measurement. Using the ImageJ software (NIH) region-of-interest (ROI) function, the N/M ratio is derived from the area of the neointima (yellow) over the area of the media (green). L, lumen; N, neointima; M, media; A, adventitia.

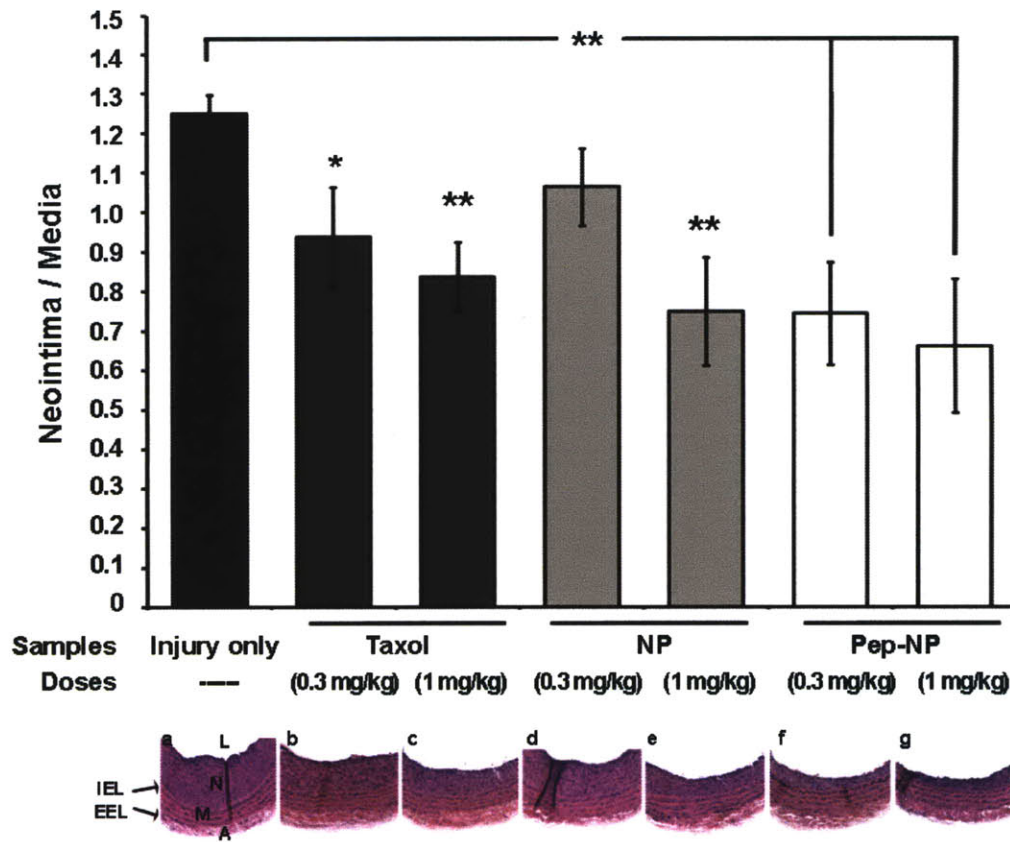


Figure 5. N/M ratio measurements of intimal proliferation.

N/M ratios taken from the site of greatest luminal narrowing per artery. Doses indicate active Ptx1 drug composition and are independent of the formulation method. Animals were dosed on Day 1 and Day 6 of surgery and the study was concluded on Day 14. All results are taken as mean \pm SEM, n=5. *, P < 0.05; **, P < 0.01 by one-way ANOVA with Tukey post hoc test. Below, representative H&E pictures from different treatment groups. L, lumen; N, neointima; M, media; A, adventitia; IEL, internal elastic lamina; EEL, external elastic lamina.

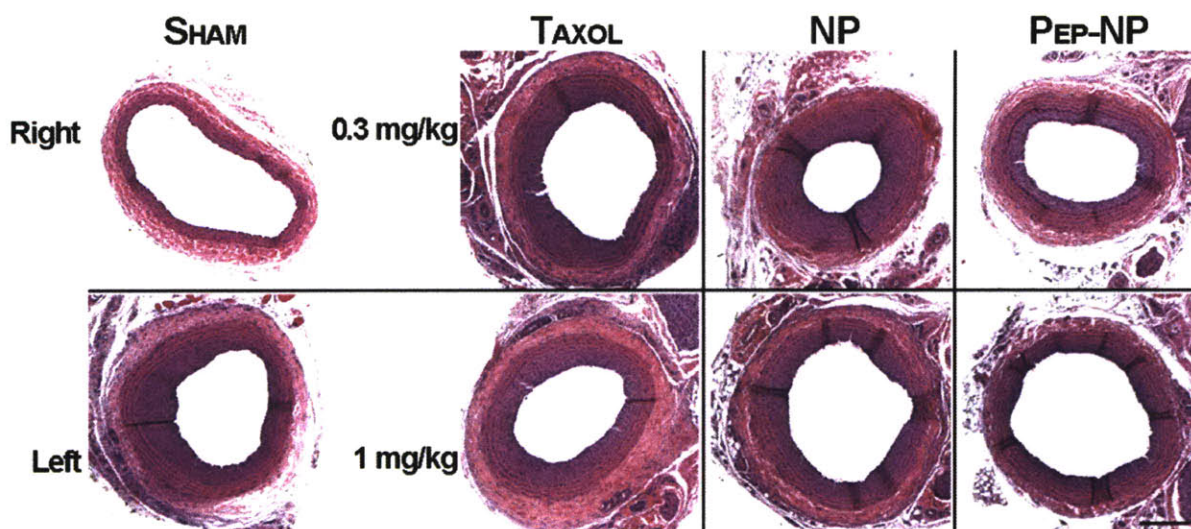


Figure 6. Representative H&E carotid cross-sections from different treatment groups. Representative H&E pictures from different treatment groups show qualitatively different levels of neointima and lumen occlusion versus sham injury-only groups and intact right carotids. These pictures also suggest a dose-response relationship within treatment groups.

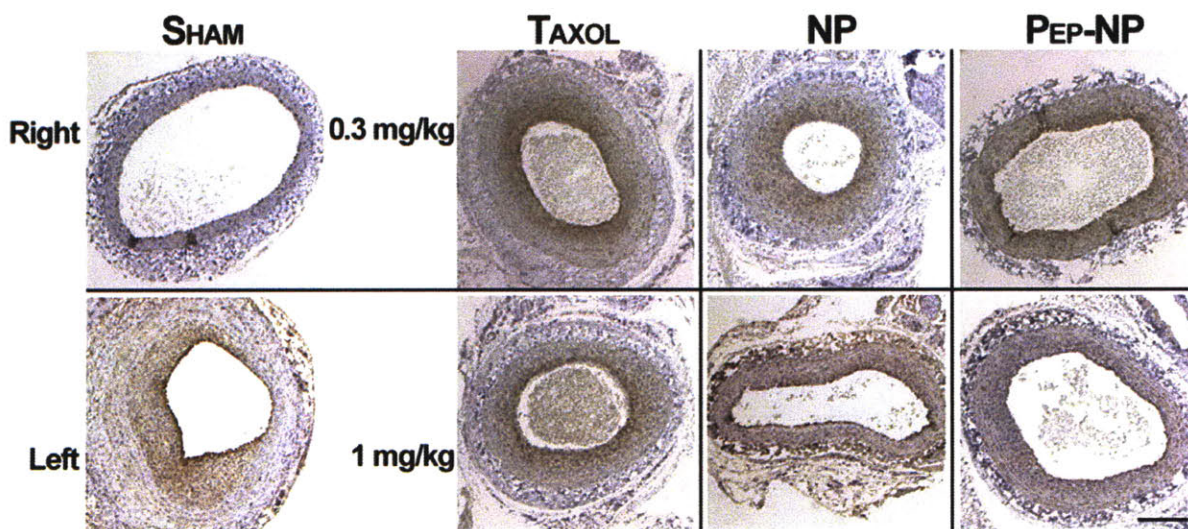


Figure 7. Representative α -SMA immunostained carotid cross-sections from different treatment groups.

Representative α -SMA immunostained cross-sections with mild hematoxylin staining from different treatment groups show qualitatively different levels of smooth muscle cell proliferation in the neointima (brown stain) versus sham injury-only groups and intact right carotids. These pictures also suggest a dose-response relationship within treatment groups.

Discussion

Recent clinical trials have tested new DES devices to overcome the problems posed by non-biodegradable drug-eluting matrices²². Biodegradable polymer matrices on stent surfaces (Supralimus, Nevo, Infinium and BioMatrix stents), stents without polymers (Artax stents) and even completely biodegradable stents (Igaki-Tamai stents^{23,24}) have been tested. Novel stents (Geneous stents) have been designed to capture endothelial progenitor cells and program them to mature into endothelial cells, preventing the adhesion of platelets, fibrin and inflammatory cells that lead to in-stent thrombosis. In parallel, there has also been a number of contradictory large-scale clinical reports underscoring the long-standing and unresolved debate on the efficacy and safety of approved DES^{6,25,26}. These safety reports are impeded by a lack of long-term safety data beyond current five-year studies.

Amidst improvements in DES design and progressively longer-term safety reports, NP-based drug delivery may be useful for patients who (i) cannot receive a DES due to a pre-existing condition, (ii) cannot take the antiplatelet medicine due to a planned surgery or allergies, (iii) have lesions in pre-stented arteries, and (iv) have lesions which are non-amenable to stenting¹³. A number of locally^{27,28} and systemically²⁹⁻³² delivered NPs have been described in the literature for the treatment of restenosis. Systemic-acting therapies such as bisphosphonates lead to an overall reduction in inflammatory cells that infiltrate and worsen lesions²⁹. Anti-proliferative drugs such as Ptxl, however, need to be localized for action and systemically delivered infusions have been unable to achieve therapeutic doses at the injury site. Hence, anti-proliferative Ptxl treatments in clinical trials have been administered to patients as local intraarterial infusions. Coroxane, a 130-nm albumin-bound paclitaxel carrier by Abraxis Biosciences (equivalent to Abraxane) is currently in Phase II trials for coronary restenosis. In these trials, Coroxane is delivered as a local intraarterial infusion following balloon angioplasty with BMS placement^{33,34}. However, vascular disease remains a chronic, life-long condition that requires long-term maintenance. Hence, systemic delivery of anti-proliferative drugs remains an attractive goal.

In this efficacy study, Taxol was used as an active control group because there is an urgent requirement for alternatives to Cremophor-EL (CrEL). The amount of CrEL required for Ptxl is significantly higher than for other drugs containing CrEL³⁴. CrEL has been shown to cause neuropathy, serious hypersensitivity reactions^{35,36} and to activate both alternative and classical pathways of the complement system^{37,38}. To prevent these hypersensitivity reactions, Taxol administration requires steroid pretreatment with antihistamines and corticosteroids. Despite pretreatment, 3% of patients will still have life-threatening reactions³⁹. Targeted hybrid NPs do not contain CrEL and therefore do not require pre-medication and long infusion times.

The short-term binding studies to injured vasculature in **Chapter 6** did not take into account an increase in matrix production over time. In this experimental angioplasty model of intimal proliferation, studies have shown that along with cell proliferative and migration responses, there is also a pronounced accumulation of extracellular matrix as the neointima grows. The response-to-injury involves the proliferation of medial SMC (first wave) followed by migration (second wave) and neointimal formation (third wave)². In a process termed modulation, the SMC in the neointima undergo a phenotypic change from ‘contractile’ to ‘synthetic’ and synthesize matrix molecules such as collagen². In one study, Sprague-Dawley rats showed a 50% increase in collagen deposition one week after surgery based on total arterial hydroxyproline content⁴⁰. Hence, the increased collagen levels corresponding to neointimal formation may form a positive loop where more vascular injury equals more target binding sites. Since the animals were also dosed on Day 6 post-procedure, the increased collagen expression may account for one aspect of the efficacy seen here.

In **Chapter 6**, we used Ptxl-PLA drug conjugates that exhibit slow elution rates *in vitro*¹⁸. In this chapter however, we used unmodified Ptxl drugs to make direct comparisons of potency against Taxol. The peptide-targeted NP groups gave lower N/M values of $N/M_{\text{Pep-NP}}=0.744 \pm 0.129$ compared to $N/M_{\text{Taxol}}=0.937 \pm 0.126$ ($P < 0.3$, mean \pm SEM, n=5) for 0.3 mg/kg treatment groups, but the N/M ratios observed in this study may be further improved (**Figure 5**). Beyond this study, the experimental set-up can be modified by: (i) extending the study to 28 days for more pronounced differences to be observed, if any, since shorter-term studies may overestimate efficacy, (ii) incorporating Ptxl-PLA conjugates for slow-release capacity, (iii) reducing the i.v. dose to accentuate N/M ratio differences at very low doses and (ii)

dosing only once instead of twice, since higher and/or more frequent doses compensate for a lack of targeting.

In conclusion, anti-proliferative therapies given as a systemic infusion on Day 1 and 6 of injury reduced neointimal hyperplasia and arterial stenosis more effectively in the targeted-NP group compared to non-targeted NP, Taxol and saline-only groups. Our findings indicate that collagen IV-targeted NPs may be clinically relevant in the treatment of injured vasculature following percutaneous angioplasty.

References

1. Ross, R. Atherosclerosis--an inflammatory disease. *N Engl J Med* **340**, 115-126 (1999).
2. Schwartz, S.M., deBlois, D. & O'Brien, E.R. The intima. Soil for atherosclerosis and restenosis. *Circ Res* **77**, 445-465 (1995).
3. Htay, T. & Liu, M.W. Drug-eluting stent: a review and update. *Vasc Health Risk Manag* **1**, 263-276 (2005).
4. Serruys, P.W., Kutryk, M.J. & Ong, A.T. Coronary-artery stents. *N Engl J Med* **354**, 483-495 (2006).
5. Pendyala, L., *et al.* Drug-eluting stents: present and future. *Cardiovasc Hematol Agents Med Chem* **6**, 105-115 (2008).
6. Stone, G.W., *et al.* Safety and efficacy of sirolimus- and paclitaxel-eluting coronary stents. *N Engl J Med* **356**, 998-1008 (2007).
7. Nakazawa, G., *et al.* Delayed arterial healing and increased late stent thrombosis at culprit sites after drug-eluting stent placement for acute myocardial infarction patients: an autopsy study. *Circulation* **118**, 1138-1145 (2008).
8. Finn, A.V., *et al.* Vascular responses to drug eluting stents: importance of delayed healing. *Arterioscler Thromb Vasc Biol* **27**, 1500-1510 (2007).
9. Cook, S., *et al.* Correlation of intravascular ultrasound findings with histopathological analysis of thrombus aspirates in patients with very late drug-eluting stent thrombosis. *Circulation* **120**, 391-399 (2009).
10. Kounis, N.G., Hahalis, G. & Theoharides, T.C. Coronary stents, hypersensitivity reactions, and the Kounis syndrome. *J Interv Cardiol* **20**, 314-323 (2007).
11. Ducrocq, G., Serebruany, V. & Tanguay, J.F. Antiplatelet therapy in the era of drug-eluting stents: current and future perspectives. *Expert Rev Cardiovasc Ther* **5**, 939-953 (2007).
12. Iakovou, I., *et al.* Incidence, predictors, and outcome of thrombosis after successful implantation of drug-eluting stents. *Jama* **293**, 2126-2130 (2005).
13. Mehran, R. & Dangas, G.D. Off-label use of drug-eluting stents: assessing the risk. *Nat Clin Pract Cardiovasc Med* **4**, 594-595 (2007).
14. Slottow, T.L. & Waksman, R. Drug-eluting stent safety. *Am J Cardiol* **100**, 10M-17M (2007).
15. Morice, M.C., *et al.* Long-term clinical outcomes with sirolimus-eluting coronary stents: five-year results of the RAVEL trial. *J Am Coll Cardiol* **50**, 1299-1304 (2007).
16. Brito, L. & Amiji, M. Nanoparticulate carriers for the treatment of coronary restenosis. *Int J Nanomedicine* **2**, 143-161 (2007).
17. Lanza, G., *et al.* Nanomedicine opportunities in cardiology. *Ann N Y Acad Sci* **1080**, 451-465 (2006).
18. Chan, J.M., *et al.* Spatiotemporal controlled delivery of nanoparticles to injured vasculature. *Proc Natl Acad Sci U S A* **107**, 2213-2218 (2010).
19. Tulis, D.A. Rat carotid artery balloon injury model. *Methods Mol Med* **139**, 1-30 (2007).
20. Clowes, A.W., Reidy, M.A. & Clowes, M.M. Kinetics of cellular proliferation after arterial injury. I. Smooth muscle growth in the absence of endothelium. *Lab Invest* **49**, 327-333 (1983).
21. Clowes, A.W., Reidy, M.A. & Clowes, M.M. Mechanisms of stenosis after arterial injury. *Lab Invest* **49**, 208-215 (1983).

22. Kukreja, N., Onuma, Y., Daemen, J. & Serruys, P.W. The future of drug-eluting stents. *Pharmacol Res* **57**, 171-180 (2008).
23. Tsuji, T., *et al.* Biodegradable stents as a platform to drug loading. *Int J Cardiovasc Intervent* **5**, 13-16 (2003).
24. Vogt, F., *et al.* Long-term assessment of a novel biodegradable paclitaxel-eluting coronary poly(lactide) stent. *Eur Heart J* **25**, 1330-1340 (2004).
25. Stone, G.W., *et al.* Paclitaxel-eluting stents versus bare-metal stents in acute myocardial infarction. *N Engl J Med* **360**, 1946-1959 (2009).
26. James, S.K., *et al.* Long-term safety and efficacy of drug-eluting versus bare-metal stents in Sweden. *N Engl J Med* **360**, 1933-1945 (2009).
27. Banai, S., *et al.* Locally delivered nanoencapsulated tyrphostin (AGL-2043) reduces neointima formation in balloon-injured rat carotid and stented porcine coronary arteries. *Biomaterials* **26**, 451-461 (2005).
28. Cyrus, T., *et al.* Intramural delivery of rapamycin with alphavbeta3-targeted paramagnetic nanoparticles inhibits stenosis after balloon injury. *Arterioscler Thromb Vasc Biol* **28**, 820-826 (2008).
29. Danenberg, H.D., *et al.* Macrophage depletion by clodronate-containing liposomes reduces neointimal formation after balloon injury in rats and rabbits. *Circulation* **106**, 599-605 (2002).
30. Danenberg, H.D., *et al.* Liposomal alendronate inhibits systemic innate immunity and reduces in-stent neointimal hyperplasia in rabbits. *Circulation* **108**, 2798-2804 (2003).
31. Cohen-Sela, E., *et al.* Nanospheres of a bisphosphonate attenuate intimal hyperplasia. *J Nanosci Nanotechnol* **6**, 3226-3234 (2006).
32. Cohen-Sela, E., *et al.* Alendronate-loaded nanoparticles deplete monocytes and attenuate restenosis. *J Control Release* **113**, 23-30 (2006).
33. Kolodgie, F.D., *et al.* Sustained reduction of in-stent neointimal growth with the use of a novel systemic nanoparticle paclitaxel. *Circulation* **106**, 1195-1198 (2002).
34. Margolis, J., *et al.* Systemic nanoparticle paclitaxel (nab-paclitaxel) for in-stent restenosis I (SNAPIST-I): a first-in-human safety and dose-finding study. *Clin Cardiol* **30**, 165-170 (2007).
35. Gelderblom, H., Verweij, J., Nooter, K. & Sparreboom, A. Cremophor EL: the drawbacks and advantages of vehicle selection for drug formulation. *Eur J Cancer* **37**, 1590-1598 (2001).
36. Authier, N., Gillet, J.P., Fialip, J., Eschalier, A. & Coudore, F. Assessment of neurotoxicity following repeated cremophor/ethanol injections in rats. *Neurotox Res* **3**, 301-306 (2001).
37. Szebeni, J., Muggia, F.M. & Alving, C.R. Complement activation by Cremophor EL as a possible contributor to hypersensitivity to paclitaxel: an in vitro study. *J Natl Cancer Inst* **90**, 300-306 (1998).
38. van Zuylen, L., Verweij, J. & Sparreboom, A. Role of formulation vehicles in taxane pharmacology. *Invest New Drugs* **19**, 125-141 (2001).
39. Weiss, R.B., *et al.* Hypersensitivity reactions from taxol. *J Clin Oncol* **8**, 1263-1268 (1990).
40. Nili, N., Zhang, M., Strauss, B.H. & Bendeck, M.P. Biochemical analysis of collagen and elastin synthesis in the balloon injured rat carotid artery. *Cardiovasc Pathol* **11**, 272-276 (2002).

Chapter 8.

Closing Remarks.

Despite the significant advances of this decade in cardiovascular treatment, cardiovascular diseases continue to be the leading cause of morbidity and mortality in developing nations, and remains the greatest health problem in the United States. Cardiovascular-related deaths claim 500,000 lives annually and estimated treatment costs exceed \$360 billion per year in the US alone¹.

Currently, one of the treatments for atherosclerosis relies on the use of oral statin therapy, which at best reduces cardiovascular events by 25% to 30%². Patients with atherosclerotic disease often survive their first cardiac event through optimal medical therapy, coronary bypass graft surgery and acute revascularization with stent placement. Despite the high usage of commercially-available DES in the cardiac field, there are a number of limitations and only select coronary lesions are amenable to DES placement. This results in the use of BMS or plain balloon angioplasty, both of which lack the benefit of anti-restenotic therapy. In other patients, transient ischemic attacks and stroke constitute the initial presentation of disease, resulting in highly limited diagnostic and therapeutic options.

Nanomedicine offers options to each of these individual challenges³. For predictive purposes, targeted NPs against plaque architecture may be used to sequentially detect and quantify plaque development in high-risk, asymptomatic patients, by monitoring underlying lesion activity and vulnerability to rupture. NPs can locally deliver anti-angiogenic therapy, which may acutely retard plaque progression, allowing aggressive statin therapy to become effective. Novel multimodal NPs may be used as theranostics to combine both diagnostic and therapeutic entities for the personalized treatment of atherosclerosis⁴. In cases proceeding to the catheterization laboratory for revascularization, NPs incorporating anti-restenotic drugs can be delivered to lesions independently of stent placement⁵. Moreover, delivery of anti-proliferative agents to the vascular wall when neointimal proliferation is most aggressive, followed by complete degradation and clearance, is most likely to improve healing of the endothelium. Prior studies have provided strong support for the importance of endothelialization in post-procedural clinical outcomes⁶. Polymer-based NPs, liposomes and micelles in the treatment of coronary

restenosis have been tested *in vitro* and *in vivo* with favorable results⁵, while clinical trials are underway for NP-based treatments of in-stent stenosis⁷.

The targeted drug delivery NP platform developed in this thesis work may be applicable for restenotic therapy independent of stent design and type of injury. The variety of anti-proliferative treatments delivered can be expanded to include drugs such as sirolimus and its analogs, or even to co-deliver more than one type of treatment. The targeted NPs may be used to treat longer lesions, multiple lesions, branch points and smaller arteries currently non-amenable to stenting⁸. Maintenance of stented arteries may also be possible when used in conjunction with stenting by giving NP doses at later time points (months and years), given the knowledge that atherosclerosis is a chronic, lifelong condition that may not be completely resolved by revascularization. Therefore, efficacy studies using stented animal models may be carried out to investigate if the targeted NPs are able to reduce in-stent stenosis. Finally, the targeted NPs may also be tested in non-stenotic models of atherosclerosis using apolipoprotein E-knockout mice for the delivery of anti-inflammatory treatments.

By expanding the utility of NP-based treatments to the application of cardiovascular disease, one would hope that the explosion in technology previously associated with oncologic treatments will be repeated⁹. Based on this ever-expanding platform of technologies, we look forward to achieving our most desired experimental result, that of improved patient outcomes.

References

1. Sanz, J., Moreno, P.R. & Fuster, V. Update on advances in atherothrombosis. *Nat Clin Pract Cardiovasc Med* **4**, 78-89 (2007).
2. MRC/BHF Heart Protection Study of cholesterol lowering with simvastatin in 20,536 high-risk individuals: a randomised placebo-controlled trial. *Lancet* **360**, 7-22 (2002).
3. Lanza, G., *et al.* Nanomedicine opportunities in cardiology. *Ann N Y Acad Sci* **1080**, 451-465 (2006).
4. Mulder, W.J., *et al.* Multimodality nanotracers for cardiovascular applications. *Nat Clin Pract Cardiovasc Med* **5 Suppl 2**, S103-111 (2008).
5. Brito, L. & Amiji, M. Nanoparticulate carriers for the treatment of coronary restenosis. *Int J Nanomedicine* **2**, 143-161 (2007).
6. Iakovou, I., *et al.* Incidence, predictors, and outcome of thrombosis after successful implantation of drug-eluting stents. *Jama* **293**, 2126-2130 (2005).
7. Margolis, J., *et al.* Systemic nanoparticle paclitaxel (nab-paclitaxel) for in-stent restenosis I (SNAPIST-I): a first-in-human safety and dose-finding study. *Clin Cardiol* **30**, 165-170 (2007).
8. Mehran, R. & Dangas, G.D. Off-label use of drug-eluting stents: assessing the risk. *Nat Clin Pract Cardiovasc Med* **4**, 594-595 (2007).
9. Zhang, L., *et al.* Nanoparticles in medicine: therapeutic applications and developments. *Clin Pharmacol Ther* **83**, 761-769 (2008).

CURRICULUM VITAE

JULIANA MARIA CHAN

77 Massachusetts Ave, Room E25-342, Cambridge MA, 02139 • juchan@mit.edu

I. EDUCATION AND CREDENTIALS

A. EDUCATION

Massachusetts Institute of Technology, U.S.A. **2006-2010**

Ph.D. candidate, Department of Biology

Advisor: Robert Langer, Sc.D., David H. Koch Institute Professor

Dissertation: *Spatiotemporal Controlled Delivery of Nanoparticles to Injured Vasculature.*

Christ's College, Cambridge University, U.K. **2002-2005**

B.A., M.A. in Biochemistry and Molecular Biology

Graduated with double First Class Honors (04, 05)

B. ACADEMIC AWARDS

- [1] S. W. Greig Prize for Natural Sciences Part IB, 2004, Cambridge University
- [2] 2004 College Prize (Christ's College, Cambridge University)
- [3] S. W. Greig Prize for Natural Sciences Part II, 2005, Cambridge University
- [4] 2005 College Prize (Christ's College, Cambridge University)
- [5] Sir Hans Kornberg Travel Award for Research, 2004, Cambridge University
- [6] Christ's College Cambridge Scholar, Cambridge University
- [7] Cambridge Commonwealth Trust Honorary Fellow, Cambridge University
- [8] Agency for Science, Technology and Research, Singapore B.S.-Ph.D. National Science Fellowship

II. TEACHING EXPERIENCE

A. TEACHING ASSISTANT, Cell Biology (7.06) **Spring 2008**

TA for Professors Hidde Ploegh and Terry Orr-Weaver

Taught two classes a week, conducted office hours and revisions,
helped write and evaluate four exams.

B. TEACHING ASSISTANT, Microbial Physiology (7.25) **Spring 2009**

TA for Professors Boris Magasanik and Uttam RajBhandary

Facilitated discussions, evaluated weekly writing assignments and two exams.

JULIANA MARIA CHAN

Page 2 of 4

III. PUBLICATIONS

- [8] **Chan JM**, Rhee JW, et al. Vascular Matrix-Targeted Lipid-Polymeric Nanoparticles Reduce Neointimal Formation After Balloon Injury in Rats. (2010, submitted).
- [7] **Chan JM**, Zhang L, Tong R, Ghosh D, Gao W, et al. Spatiotemporal Controlled Delivery of Nanoparticles to Vasculature. *Proc Natl Acad Sci U S A*. (2010) 107(5):2213-8.
(Highlighted in **BBC Health, The Independent, Science Daily, Nature Scibx, Medical News Today, Nano Today, The Straits Times**).
- [6] **Chan JM**, Valencia PM, Zhang L, Langer R, Farokhzad OC. Polymeric nanoparticles for drug delivery. *Methods Mol Biol*. (2009) 624:163-75.
- [5] **Chan JM**, Zhang L, Yuet KP, Liao G, Rhee JW, Langer R, et al. PLGA-lecithin-PEG core-shell nanoparticles for controlled drug delivery. *Biomaterials*. (2009) 30(8):1627-34.
- [4] Nguyen DN, Green JJ, **Chan JM**, Langer R, Anderson DG. Polymeric Materials for Gene Delivery and DNA Vaccination. *Advanced Materials*. (2009) 21(8):847-67.
- [3] Zhang L, **Chan JM**, Gu FX, Rhee J-W, Wang AZ, et al. Self-Assembled Lipid-Polymer Hybrid Nanoparticles: A Robust Drug Delivery Platform. *ACS Nano*. (2008) 2(8):1696-702.
- [2] Wang AZ, Gu F, Zhang L, **Chan JM** et al. Biofunctionalized targeted nanoparticles for therapeutic applications. *Expert Opin Biol Ther*. (2008) 8(8):1063-70.
- [1] Zhang L, Gu FX, **Chan JM**, Wang AZ, Langer RS, Farokhzad OC. Nanoparticles in medicine: therapeutic applications and developments. *Clin Pharmacol Ther*. (2008) 83(5):761-9.

IV. PRESENTATIONS

A. CONFERENCE & POSTER PRESENTATIONS

- [1] US-Japan Drug Delivery Symposium 2007
- [2] Center for Cancer Nanotechnology Excellence (CCNE) annual meeting 2008
- [3] Center for Cancer Nanotechnology Excellence (CCNE) annual meeting 2009
- [4] US-Japan Drug Delivery Symposium 2009

B. TALKS GIVEN

- [1] Center for Cancer Nanotechnology Excellence (CCNE) monthly meeting

Oct 10, 2008

JULIANA MARIA CHAN

Page 3 of 4

V. GRANT & REVIEWING EXPERIENCE

A. RESEARCH GRANT WRITING

Wrote and contributed data towards a NHLBI-PEN Program of Excellence in Nanotechnology translational grant (PI: Robert Langer/Zahi A. Fayad) – Grant funded: April 2010.

B. REVIEWS

Peer-reviewed manuscripts (on behalf of Dr. Omid Farokhzad) for journals including Langmuir, ACS Nano and JACS.

VI. RESEARCH EXPERIENCE

A. RESEARCH HISTORY

- [1] **Technician/Research Assistantship** Aug 2005-Jul 2006
Prof. Sir David P. Lane lab, Institute of Molecular and Cellular Biology, Singapore
- [2] **Undergraduate Honors Project** Jan-Mar 2005
Prof. Richard J. Jackson lab, University of Cambridge, UK
Dissertation: *Reinitiation of eukaryotic mRNA translation after puromycin-induced termination*. Awarded first class honors.
- [3] **Sir Hans Kornberg Travel Award for Research summer project** Aug-Oct 2004
Prof. Thomas F. Martin lab, University of Wisconsin-Madison, USA
Abolished synaptotagmin IX expression using RNAi in PC3 cell lines.
Acknowledged in Lynch KL et al. *J. Cell Sci* (2007) 120: 617-627.

B. RESEARCH SKILLS

HPLC, SEM, TEM, dynamic light-scattering, ELISA, immunohistochemistry, fluorescence microscopy, molecular biology, cell culture, bacteriophage display screening, radioisotope studies (^3H , ^{35}S -Met, ^{111}In , ^{32}P), xenograft tumor mice models, *in vivo* biodistribution and circulation half-life studies.

VII. PATENTS

- [1] Alexis F, Zhang L, Chan J, Basto P, Levy-Nissebaum E, Langer R, Farokhzad OC. Poly (Amino Acid)-Targeted Drug Delivery. PCT/US08/059491.
- [2] Salvador-Morales C, Chan JM, Zhang L, Gao W, Langer R, Farokhzad OC. Particles with multiple functionalized surface domains. (PCT filed, Sept 09).
- [3] Chan JM, Langer R, Farokhzad OC. Endothelial Basement Membrane Targeting Peptide Ligands for Nanoparticle Delivery of Therapeutic Agents. (PCT Filed, Dec 09).

JULIANA MARIA CHAN

Page 4 of 4

VIII. REFERENCES

Robert Langer, Sc.D.

David H. Koch Institute Professor
Department of Chemical Engineering, Massachusetts Institute of Technology
77 Massachusetts Avenue, Room E25-342, Cambridge, MA 02139
Tel: 617-253-3107, Fax: 617-258-8827, Email: rlanger@mit.edu

Omid C. Farokhzad, M.D.

Associate Professor
Laboratory of Nanomedicine and Biomaterials, Department of Anesthesiology, Brigham and Women's Hospital, Harvard Medical School, 75 Francis Street, Boston, MA, 02115, USA
Tel: 617-732-6093, Fax: 617-264-6378, Email: ofarokhzad@zeus.bwh.harvard.edu

Liangfang Zhang, Ph.D.

Assistant Professor
Department of NanoEngineering, University of California, San-Diego
Moore's Cancer Center, MC-0815, 3855 Health Sciences Drive, La Jolla, CA 92093, USA
Tel: 858-246-0999, Fax: 858-534-9553, Email: zhang@ucsd.edu